

Peatlands to the Rescue! Late Holocene History of Climate and Storms as Told by Coastal  
Peatlands on the Magdalen Islands, Québec, Canada

Antoine Lachance

A Thesis in  
The Department  
of  
Geography, Planning & Environment

Presented in Partial Fulfillment of the  
Requirements for the Degree of Master of Science  
(Geography) at Concordia University  
Montreal, Québec, Canada

November 2022

© Antoine Lachance, 2022

**CONCORDIA UNIVERSITY**

**School of Graduate Studies**

This is to certify that the thesis

prepared by: Antoine Lachance

entitled: Peatlands to the Rescue! Late Holocene History of Climate and Storms as  
Told by Coastal Peatlands on the Magdalen Islands, Québec, Canada

and submitted in partial fulfillment of the requirements of the degree of

**Master of Science (Geography)**

complies with the regulations of the University and meets the accepted standard with respect to originality and quality.

Signed by the final Examining Committee:

\_\_\_\_\_ Chair

*Dr. Alexandra Lesnikowski*

\_\_\_\_\_ External Examiner

*Dr. Steve Pratte*

\_\_\_\_\_ Internal Examiner

*Dr. Pascale Biron*

\_\_\_\_\_ Supervisor

*Dr. Jeannine-Marie St-Jacques*

\_\_\_\_\_ Supervisor

*Dr. Matthew Peros*

Approved by \_\_\_\_\_ Chair of Department

*Dr. Craig Townsend*

Date: \_\_\_\_\_ Dean of Faculty

*Dr. Pascale Sicotte*

## ABSTRACT

Peatlands to the Rescue! Late Holocene History of Climate and Storms as Told by Coastal  
Peatlands on the Magdalen Islands, Québec, Canada

*Antoine Lachance*

Storms are pervasive dangers to coastal communities in Eastern Canada and, under future climate scenarios, these extreme weather events are projected to increase in intensity. However, the impacts of climate change on storm variability have not been studied extensively in this region, in part due to the short and incomplete instrumental storm records. Environmental paleo-data archives recording high-impact storms on multi-centennial to multi-millennial timescales can provide invaluable information to document past storm variabilities and to support and inform adaptation strategies. First, a review of the literature on paleo-storm studies from the North Atlantic was conducted. Then, a reconstruction of late Holocene environmental changes and storms is presented, based on the analyses of two ombrotrophic peat cores from the Magdalen Islands, Québec, in the Gulf of St. Lawrence. The cores were dated by  $^{14}\text{C}$  and  $^{210}\text{Pb}$ , with the bottommost peat dating to  $\sim 4920$  BP and  $\sim 4720$  BP. We used a multi-proxy approach based on sedimentological and geochemical analysis to examine the evolution of the peatlands, as well as local climate on the Magdalen Islands during the past 4000 years, and to reconstruct storms during the past 1000 years, i.e., the period for which both cores display clear ombrotrophic conditions. The storm reconstruction was validated using the hurricane record from the Magdalen Islands over the past 150 years, and shows a particularly active period between 1400-1650 CE, when heightened activity was also identified in other studies from the northwestern North Atlantic, as well as a notable increase in storms since 1930 CE. While warm sea-surface temperature (SST) anomalies seem to have contributed to more frequent storms since 1930 CE, the 1400-1650 CE active period occurred during the Little Ice Age (LIA), a period of generally cooler SSTs in the North Atlantic. Our study is the first to use ombrotrophic peat cores to track storm frequency in eastern North America, as well as one of the northernmost paleotempestological studies on the continent. Future research should focus on understanding the climatic factors that control storm variation in Eastern Canada, especially over the last millennium.

## ACKNOWLEDGEMENTS

I would like to express my deepest gratitude to my supervisors, Dr. Jeannine-Marie St-Jacques and Dr. Matthew Peros, without whom this project would not have been possible. Their constant support and trust for my ideas, thoughtful feedbacks and suggestions, and helpful patience made working with them an invaluable learning experience. I am extremely grateful to my thesis committee, Dr. Steve Pratte and Dr. Pascale Biron, for the time they invested in reviewing this thesis, as well as Dr. Damon Matthews. I could not have undertaken this project without the financial support of Concordia University, the *Fond de recherche du Québec – Sciences et technologies*, the Power Corporation of Canada, and Hydro-Québec.

I would like to extend my sincere thanks to the GEOTOP research team, Dr. Michelle Garneau, Dr. Nicole Sanderson, and Leonie Perrier, for the helpful guidance in age-modelling and peat stratigraphy; the team at the INRS, Dr. Pierre Francus and Arnaud De Coninck, for helping me with the geochemical analysis; Sydney and Tania, who helped me at the very beginning of the project on the Magdalen Islands; and Jennifer Srey, for her invaluable advice throughout the Master.

Lastly, I would be remiss in not mentioning my family and friends for their unwavering encouragements in the hardest moments, particularly my partner Simon and my dear friend Ella. A special thanks to my cat, Luna, for constant emotional support.

## **CONTRIBUTION OF AUTHORS**

Chapter 4

Co-authors:

Jeannine-Marie St-Jacques and Matthew Peros

*Les faits ne pénètrent pas dans le monde où vivent nos croyances, ils n'ont pas fait naître celles-ci, il ne les détruisent pas; ils peuvent leur infliger les plus constants démentis sans les affaiblir, et une avalanche de malheurs ou de maladies se succédant sans interruption dans une famille ne la fera pas douter de la bonté de son Dieu ou du talent de son médecin.*

Marcel Proust, 1913

## TABLE OF CONTENTS

|   |            |
|---|------------|
| <b>List of figures.....</b>   | <b>vii</b> |
| <b>List of tables.....</b>  | <b>xi</b>  |
| <b>CHAPTER 1: Introduction.....</b>   | <b>1</b>   |
| <b>CHAPTER 2: Literature review.....</b>  | <b>4</b>   |
| <b>2.1 Introduction.....</b>  | <b>4</b>   |
| <b>2.2 Climatology of tropical and extratropical cyclones.....</b>                      | <b>4</b>   |
| 2.2.1 Definition of TCs and ETCs.....   | 4          |
| 2.2.2 Temporal variability of TCs and ETCs.....   | 7          |
| 2.2.3 Impacts of climate change on TCs and ETCs.....                                    | 7          |
| <b>2.3 Paleotempestology: definition and methods.....</b>                               | <b>8</b>   |
| 2.3.1 Site selection and types of natural archives.....                                 | 8          |
| 2.3.2 Aspects of storms relevant to paleotempestology and related storm proxies.....    | 10         |
| <b>2.4 Overview of paleo-storm studies published since 2000.....</b>                    | <b>16</b>  |
| <b>2.5 Long-term perspective on tropical and extratropical cyclone variability.....</b> | <b>20</b>  |
| 2.5.1 Long-term TC trends.....  | 20         |
| 2.5.2 Long-term ETC trends.....   | 21         |
| <b>2.6 Conclusion.....</b>  | <b>22</b>  |
| <b>CHAPTER 3: Research questions and objectives.....</b>                                | <b>23</b>  |
| <b>CHAPTER 4: Research article manuscript.....</b>                                      | <b>24</b>  |
| <b>4.1 Introduction.....</b>  | <b>25</b>  |
| <b>4.2 Regional setting.....</b>  | <b>28</b>  |
| <b>4.3 Methods.....</b>   | <b>31</b>  |
| 4.3.1 Site description and field methods.....   | 31         |
| 4.3.2 Chronology and Peat Accumulation Rates.....                                       | 34         |
| 4.3.3 Peat type analysis.....   | 34         |

|  |            |
|--|------------|
| 4.3.4 Computerized tomography and x-ray radiography .....                            | 35         |
| 4.3.5 $\mu$ -XRF analysis .....  | 36         |
| 4.3.6 Mineral and organic content .....  | 36         |
| 4.3.7 Aeolian Sand Influx .....  | 37         |
| 4.3.8 Multivariate analysis.....   | 38         |
| 4.3.9 Determining storm frequency .....  | 39         |
| <b>4.4 Results and discussion .....</b>  | <b>41</b>  |
| 4.4.1 Overview.....  | 41         |
| 4.4.2 Age-depth models and PAR .....   | 41         |
| 4.4.3 Core description: sedimentology of TAC and TLM.....                            | 45         |
| 4.4.4 $\mu$ -XRF elemental downcore variations.....                                  | 52         |
| 4.4.5 PCA and biplot of elemental data.....  | 56         |
| 4.4.6 Processes controlling sediment inputs at each core site .....                  | 59         |
| 4.4.7 Insights from core sedimentology and geochemistry on peatland development..... | 60         |
| 4.4.8 Reconstructing storminess over the past 168 years .....                        | 65         |
| 4.4.9 Storm frequency over the last 1000 years.....                                  | 70         |
| 4.4.10 Regional paleostorm patterns and climate.....                                 | 73         |
| <b>4.5 Conclusion .....</b>  | <b>77</b>  |
| <b>CHAPTER 5: General conclusions and future directions .....</b>                    | <b>78</b>  |
| <b>References.....</b>   | <b>80</b>  |
| <b>Supplementary figures.....</b>  | <b>92</b>  |
| <b>Supplementary tables .....</b>  | <b>101</b> |

## List of figures

- Figure 2.1** Life cycle of a Cape Verde hurricane, from the formation of a tropical disturbance off the coast of West Africa, to its intensification into a tropical cyclone in the eastern North Atlantic Ocean, and finally to the weakening of the tropical cyclone and extratropical transition. Figure taken from the NOAA website ([https://www.nhc.noaa.gov/outreach/presentations/2013\\_02nhcL311\\_hurricaneLifeCycleHazard s.pdf](https://www.nhc.noaa.gov/outreach/presentations/2013_02nhcL311_hurricaneLifeCycleHazard s.pdf)). (John Cangialosi, 2012). ..... 5
- Figure 2.2** A) Hurricane (TC) tracks from 1850-2020 from the IBTrACKS dataset (Knapp, Kruk, Levinson, Diamond, & Neumann, 2010). B) Extratropical cyclone (ETC) tracks from 1989 to 2009 from the ERA-Interim reanalysis dataset [30]. The location of the province of Québec, Canada is indicated as QC. .... 6
- Figure 2.3** Potential sites (inland, coastal, and offshore) for paleo-storm studies (1) and examples of natural archives along an inland-offshore gradient (2). Natural archives from peatlands/wetlands, lakes/sinkholes, salt marshes, lagoons, and blue holes/basins usually consist of sediment cores. Natural archives from forests/trees and speleothems use chronologically successive growth rings or layers. Natural archives from beach berms/ridges are usually chronologically successive samples from a sequence of berms or ridges. .... 9
- Figure 2.4** Schematic of the relationships among storm characteristics and processes, storm proxies and methods. Blue boxes: storm characteristics; green boxes: storm-related processes of interest in paleo-storm research; grey boxes: storm proxies; white boxes: methods to identify and measure the storm proxies. Modified from Masselink and van Heteren (2014). .... 10
- Figure 2.5** Schematic illustration of the four storm surge regimes from Masselink & van Heteren (Masselink & van Heteren, 2014) and impacts on coastal barrier systems.  $D_{low}$  and  $D_{high}$  refer to the position of the height of the barrier foot and crest, respectively.  $R_{high}$  refers to the highest action of the waves, while  $R_{low}$  refers to the lowest position of the storm wave setup. Figure from Goslin and Clemmensen (2017). .... 13
- Figure 2.6** Maps of the 92 paleo-storm studies across the North Atlantic. The studies are classified by the storm variable proxy type. .... 18
- Figure 2.7** A) Number of studies per region in the North Atlantic. B) Number of studies per storm variable examined. C) Duration of the records, from longest to shortest, per region in the North Atlantic and per storm variable examined. .... 19
- Figure 4.1** A-C. Location of the Magdalen Islands, Québec, Canada, in the Gulf of St. Lawrence. This study is focused on the southern island, *Ile-du-Havre-Aubert* (red rectangle). The two coring sites are indicated by blue squares. D. Seasonal wind roses displaying 12 directions of incoming winds based on daily peak wind gusts data from 1984 to 2018. The number of days (expressed as %) for any category of speed of peak wind gusts (in km/h) are indicated for each wind direction. Winds are stronger during the fall and winter and mostly coming from the southwest, west and northwest. E-F. Erosional features on the coast of the Magdalen Islands. .... 30
- Figure 4.2** A) Map of *Ile-du-Havre-Aubert*, the southernmost island of the archipelago. The two coring sites, TAC and TLM, are indicated by a blue square overlain by a red square, delimiting the insets B and C. The main beaches surrounding the island are indicated by yellow dots. B-C) TAC and TLM coring sites. The locations where the cores were extracted are indicated by blue squares. The TAC core site is 250 m away from the south facing cliffs, while the TLM core site is 2150 m

away from the closest beach, which is du Cap beach. D) Photos of the coring site at TLM. The cores were extracted in 50 cm sections and then wrapped in PVC split-tubes. E) Visible tracks from the snowmobile trail cutting through TLM. F-G) Photos of core sections after they were extracted from the peatland and before transferring them into PVC split-tubes. Panel F shows a section from 125-175 cm from TAC, containing visible sand layers. Panel G shows a section from 600-700 cm from TLM, containing a layer of coarse sand defining the lower limit of the peat column..... 33

**Figure 4.3.** BACON-derived age-depth models for TAC (A) and TLM (B). Radiocarbon ( $^{14}\text{C}$ ) dates are shown in blue along the age model and  $^{210}\text{Pb}$  dates from the top 50 cm of the TAC core only are shown in purple. The surface date (2019 CE) is indicated in teal. In the TAC core, the rate of supported  $^{210}\text{Pb}$  (right axis) is indicated by the blue boxes on the left-hand side (the blue boxes are the measured  $^{210}\text{Pb}$  values; blue shadings represent the modelled  $^{210}\text{Pb}$  values). For each core, the leftmost upper panel depicts the Markov Chain Monte Carlo (MCMC) iterations; then the prior (green curve) and posterior (grey histogram) distributions the accumulation rate (second panel), and next the memory (third panel). For TAC, the fourth panel indicates  $^{210}\text{Pb}$  influx in  $\text{Bq/m}^2\cdot\text{yr}$  and the fifth panel indicates supported  $^{210}\text{Pb}$  in  $\text{Bq/kg}$ . The peat accumulation rates (PARs) are indicated for certain sections of the cores in  $\text{cm/yr}$ . ..... 44

**Figure 4.4** Lithology and sedimentology of the TAC core without the basal sand layers. The core is plotted by depth (left-hand side) with the corresponding age from the age-depth model on the right-hand side, in CE/BCE. The x-ray images were taken by computerized-tomography scanning (CT-Scan). Peat stratigraphy is indicated by color. The width of each layer is a qualitative indication of density. Dry bulk density (DBD) is shown as  $\text{g/cm}^3$ . Carbon accumulation rate is shown as  $\text{g/m}^2\cdot\text{yr}$ . Mineral content is the percent of minerals in  $5\text{ cm}^3$  of dried peat. Aeolian sand influx (ASI) is presented in  $\text{g/m}^2\cdot\text{yr}$  per year. Modelled AMS  $^{14}\text{C}$  dates are shown as a blue triangle for a date from wood, and as a red circle for a date from bulk peat. Core units calculated by CONISS algorithm are also shown on the right of each plot..... 50

**Figure 4.5** Lithology and sedimentology of the TLM core without the basal sand layers. The core is plotted by depth (left-hand side) with the corresponding age from the age-depth model on the right-hand side, in CE/BCE. The x-ray images were taken by computerized-tomography scanning (CT-Scan). Peat stratigraphy is indicated by color. The width of each layer is a qualitative indication of density. Dry bulk density (DBD) is shown as  $\text{g/cm}^3$ . Carbon accumulation rate is shown as  $\text{g/m}^2\cdot\text{yr}$ . Mineral content is the percent of minerals, in  $5\text{ cm}^3$  of dried peat. Aeolian sand influx (ASI) is presented in  $\text{g/m}^2\cdot\text{yr}$  per year. Modelled AMS  $^{14}\text{C}$  dates are shown as a blue triangle for a date from wood, and as a red circle for a date from bulk peat. Core units calculated by CONISS algorithm are also shown on the right of each plot..... 51

**Figure 4.6** TAC XRF data (A) and principal component results (B), by zones. XRF data are expressed in thousands counts per second (kCPS). The black lines in A and B are smoothers, showing data averaged every centimeter ..... 54

**Figure 4.7** TLM XRF data (A) and principal component results (B), by zones. XRF data are expressed in thousand counts per second (kCPS). The black lines in A and B are smoothers, showing data averaged every centimeter. Note the break in the y-axis near 550 cm and the different x-axis scales in these two sections. .... 55

**Figure 4.8** PCA analyses of the 10 major elements for TAC and TLM. Each subunit is represented by a different colored symbol. The supplementary variables (CAR, ASI, DBD and Minerals) are

represented by the dashed blue arrows, while the variables used in the PCA analysis are in solid black. Note that the CAR arrow in TAC overlaps with the Fe arrow and that the DBD arrow in TLM overlaps with the Ca arrow..... 58

**Figure 4.9** Comparison of selected sedimentological and geochemical variables between the two Magdalen Islands sites (TAC in red and TLM in blue) plotted by age (CE/BCE). Note that the sign of PC2 for TAC is reversed from how it is reported in Table 2 and Figure 8 so that the direction of the effect is the same between the two cores, with positive values meaning relatively more elements from group 1 (enhanced aeolian processes [AP+]) and vice-versa (AP-). Blue zones represent documented periods of cold climate in the northern hemisphere: the Neoglacial cooling from 1050 BCE – 850 CE and the Little Ice Age (LIA) from 1350-1910 CE, while the white zones are periods of warmer climate: the Holocene Climate Optimum (HCO) from 9700 – 1000 BCE and the Medieval Climate Anomaly (MCA) from 950-1350 CE (Magnan & Garnau, 2014). ..... 64

**Figure 4.10** A) Storm proxies from the TAC core for 1850-2019 CE: ASI in  $\text{g/m}^2 \cdot \text{yr}$  and Ti counts. The Ti count data was detrended by subtracting a 30-year moving average. The dotted black line represents the threshold for storm detection, i.e., any Ti measurements above the 95<sup>th</sup> percentile of the detrended Ti count data. All identified storms are identified with a red dot. The grey shaded boxes represents clusters of events, i.e., the range between the positive and negative age uncertainty around the most recent and oldest storm detected within a cluster (indicated by vertical red lines). B) Bar chart of wind data from the IBTrACKS and Historical Weather datasets. For the Historical Weather dataset, only days with winds above 110 km/h are shown. C) All hurricanes that tracked less than 100 km from the Magdalen Islands and peak winds (in km/h) recorded at the hurricane location at the time of passage are shown. Wind events that had a recorded impact on the Magdalen Islands are indicated in red. D) The AMV index from van Oldenborgh, te Raa, Dijkstra, and Philip (2009) with the positive (negative) phases highlighted in blue (red). ..... 69

**Figure 4.11** Storm proxies from the TAC (A) and TLM (B) cores for 1000-2019 CE, including ASI in  $\text{g/m}^2 \cdot \text{yr}$  and Ti counts. The Ti count data was detrended by subtracting a 30-year moving average. The dotted black line in A and B represent the threshold for storm detection, i.e., any Ti measurements above the 95<sup>th</sup> percentile of the detrended Ti count data are counted as storms. All storms are identified with a red dot, together with their age uncertainty. The grey shaded boxes are used to highlight events or clusters of events. C) Time-series of events/century for TAC and TLM. Given our use of a centered 168 years sliding window to calculate the running sum, we do not have storm frequency data for the first 84 years of the record. .... 72

**Figure 4.12** Comparison of our two Magdalen Islands storm (Ti CPS) records to previously published research (C. Salt Pond, Massachusetts, storm records from Donnelly et al. (2015); D. Atlantic Multidecadal Variability (AMV) record from Mann, Zhang, et al. (2009); and E. North Atlantic SST anomalies from Orme et al. (2021)). ..... 76

**Figure S1** Diagram of the depths of each segment of the cores (TLM on the left, TAC on the right). The black dashed line on the x-axis represents the surface. Notice the y-axis is different in the two subgraphs. Core drives or core segments that were aggregated to create the composite cores are indicated in solid green. The TLM composite core includes: the segment from the surface to 25 cm from the TLM-monolith; the segment from 25 cm to 100 cm from TLM-2; and the full core drive from TLM-1. The TAC composite core includes: the full TAC-monolith section; the section from 50 cm to 275 cm from TAC-4; and the full TAC-5b core drive. The other cores or core

segments (green hatched) were kept for preliminary analysis, other research purposes and for reference, if needed. .... 92

**Figure S2 A** Photos of the cores taken at the TAC and TLM sites after extraction from the peatland. .... 93

**Figure S3** Lithology and sedimentology of the TAC core with the basal sand layers. The core is plotted by depth (left-hand side) with the corresponding age from the age-depth model on the right-hand side, in CE/BCE. The x-ray images were taken by computerized-tomography scanning (CT-Scan). Peat stratigraphy is indicated by color. The width of each layer is a qualitative indication of density. Dry bulk density (DBD) is shown as  $\text{g/cm}^3$ . Carbon accumulation rate is shown as  $\text{g/m}^2 \cdot \text{year}$ . Mineral content is the percent of minerals, in  $5 \text{ cm}^3$  of dried peat. Aeolian sand influx (ASI) is presented in  $\text{g/m}^2 \cdot \text{yr}$  per year. Modelled AMS  $^{14}\text{C}$  dates are shown as a blue triangle for a date from wood, and as a red circle for a date from bulk peat. Core units calculated by CONISS algorithm are also shown on the right of each plot. .... 96

**Figure S4** Lithology and sedimentology of the TLM core with the basal sand layers. The core is plotted by depth (left-hand side) with the corresponding age from the age-depth model on the right-hand side, in CE/BCE. The x-ray images were taken by computerized-tomography scanning (CT-Scan). Peat stratigraphy is indicated by color. The width of each layer is a qualitative indication of density. Dry bulk density (DBD) is shown as  $\text{g/cm}^3$ . Carbon accumulation rate is shown as  $\text{g/m}^2 \cdot \text{year}$ . Mineral content is the percent of minerals, in  $5 \text{ cm}^3$  of dried peat. Aeolian sand influx (ASI) is presented in  $\text{g/m}^2 \cdot \text{yr}$  per year. Modelled AMS  $^{14}\text{C}$  dates are shown as a blue triangle for a date from wood, and as a red circle for a date from bulk peat. Core units calculated by CONISS algorithm are also shown on the right of each plot. .... 97

**Figure S5** PCA test performed in R of TAC (left) and TLM (right). PC axes 1, 2 and 3 are significant at  $p\text{-value} < 0.05$  for TAC, and PC axes 1 and 2 are significant at  $p\text{-value} < 0.05$  for TLM. .... 98

**Figure S6** BACON-derived alternative age-depth models for TLM. Radiocarbon ( $^{14}\text{C}$ ) dates are shown in blue along the age model. The  $^{210}\text{Pb}$  dates from the top 50 cm of the TAC core were plugged into the TLM age-depth model, adjusting for TLM depths, and are shown in purple. The surface date (2019 CE) is indicated in teal. The rate of supported  $^{210}\text{Pb}$  (right axis) is indicated by the blue boxes on the left-hand side (the blue boxes are the measured  $^{210}\text{Pb}$  values; blue shadings represent the modelled  $^{210}\text{Pb}$  values). The leftmost upper panel depicts the Markov Chain Monte Carlo (MCMC) iterations; then the prior (green curve) and posterior (grey histogram) distributions the accumulation rate (second panel), and next the memory (third panel). The fourth panel indicates  $^{210}\text{Pb}$  influx in  $\text{Bq/m}^2 \cdot \text{yr}$  and the fifth panel indicates supported  $^{210}\text{Pb}$  in  $\text{Bq/kg}$ . .... 99

**Figure S7** Comparison of TAC and TLM storm proxies with an alternative age-model for TLM, where  $^{210}\text{Pb}$  values from TAC were plugged into an age-model for TLM (see Supplemental Figure S6). In panel A and B, the ASI and Ti peaks from both cores match together, especially in the period from 2010-1970. .... 100

## List of tables

|  |     |
|--|-----|
| <b>Table 4.1</b> Accelerator mass spectrometry radiocarbon ( $^{14}\text{C}$ ) results for both sites in the Magdalen Islands. Dated material is from bulk peat sediment (bulk) or wood fragments (wood). Uncalibrated $^{14}\text{C}$ dates are shown as years before 1950 (BP). The $^{14}\text{C}$ dates were input into the Bayesian (BACON) algorithm in R and calibrated with the IntCal20 calibration curve. Calibrated dates are presented as calibrated years before 1950 (cal. BP) and as Common Era/Before Common Era (CE/BCE)..... | 42  |
| <b>Table 4.2</b> Correlations between the first two principal components (PCs), and the XRF variables and supplementary variables for TAC and TLM. Only the first two statistically significant ( $p < 0.05$ ) PCs are shown. Statistically significant ( $p < 0.01$ ) correlations are shown in bold dark blue (positive correlations) and bold red (negative correlations). Non-statistically significant correlations are in black. ....  | 57  |
| <b>Table S1</b> Description of the main characteristics of the 92 studies included in the meta-analysis. ....  | 101 |
| <b>Table S2</b> List of cores drives from the TLM and TAC. Cores with a <i>b</i> suffix were taken in the same hole as their corresponding core and therefore have overlapping material (for example, TLM-1b corresponds to depth 669-719 cm and was taken from the same hole as TLM-1, which corresponds to depth 100-700 cm. Therefore, there is overlapping material between the two core sections). Cores with an asterisk (*) were used to create the composite cores.....  | 107 |
| <b>Table S3</b> Results of DCA analysis with Decorana algorithm in R, on XRF data at the mm-scale for TAC and TLM. The first DCA axis length is less than 3 standard deviations for both TLM and TAC, therefore a linear analysis is possible (PCA). ....  | 108 |
| <b>Table S4</b> List of hurricanes that passed by 100 km or closer from the Magdalen Islands, with recorded wind of the hurricane at that time and known impacts. ....   | 109 |
| <b>Table S5</b> Days when winds exceeded 110 km/h on the Magdalen Islands and known impacts. Data from the Historical Weather dataset (Environment and Climate Change Canada, 2020). ....  | 110 |

## CHAPTER 1: Introduction

The rise in extreme weather events since the beginning of the 21<sup>st</sup> century is, in many respects, unprecedented. First and foremost, it can be attributed to the anthropogenic influence exerted on the climate (Arias et al., 2021), and the rapid pace of the rise in extreme weather events is, in some cases, too fast for human society to adapt to. People living in low-lying coastal areas are amongst the most vulnerable to climate change: they represent about 11% of the human population and are exposed to coastal flooding related to extreme weather events, a number that is bound to increase with the projected sea-level rise (Neumann, Vafeidis, Zimmermann, & Nicholls, 2015). Among extreme weather events, tropical cyclones (TCs) and extratropical cyclones (ETCs) are the leading cause of economic damage to coastal communities worldwide (Klotzbach, Bowen, Pielke, & Bell, 2018). Therefore, much effort has been made to understand the potential impacts of anthropogenic climate change on the frequency, intensity, and distribution of TCs and ETCs. The IPCC's 6<sup>th</sup> Assessment Report states that it is *likely* that the global proportion of major tropical cyclones will increase due to climate change, yet there is *low confidence* about the long-term trends in cyclone frequency due to the scarcity of high resolution long-term data on these events (Arias et al., 2021). While some historical cyclone datasets go back to the 19<sup>th</sup> century, data from satellites, which permit a consistent assessment of cyclone intensity, only go back to the 1970s (Walsh et al., 2016). These detailed satellite datasets provide us with the information needed to understand the processes and climatology of cyclones, yet they do not cover nearly enough time to assess long-term trends (Donnelly et al., 2015; Donnelly & Woodruff, 2007).

Eastern Canada, especially the Maritimes, is located at the northwestern margin of the North Atlantic TC tracks and has been struck repeatedly by severe tropical storms and even hurricanes (Oliva et al., 2018). For example, Hurricane Juan struck Nova Scotia in 2003 (McTaggart-Cowan, Atallah, Gyakum, & Bosart, 2006), Hurricane Igor impacted Newfoundland in 2010 (Masson, 2014), and Hurricane Dorian struck Nova Scotia in 2019 (Ezer, 2020). The most recent such event is Hurricane Fiona, a record-breaking hurricane that swept the Maritimes and is predicted to cost more than \$660 million in insured damage, making it the costliest extreme weather event in Atlantic Canada (Insurance Bureau of Canada, 2022). The Maritimes are also especially vulnerable to ETCs, which form in the mid-latitudes along the polar jet stream and travel eastward, with peak intensity during the fall and winter (Feser et al., 2015). Although ETCs are

usually less intense in terms of wind velocity compared to TCs, they are much more frequent and can be very destructive when associated with stationary patterns of extreme rains, thus causing flooding (Francis & Vavrus, 2012). The long-term trends of TCs and ETCs and the potential impacts of climate change on these events in Eastern Canada have not been studied extensively, despite the threat that they pose (Oliva et al., 2018).

It is possible to improve our understanding of the relationships between climate and cyclones by reconstructing pre-instrumental cyclone variability from a variety of natural storm archives (Raible, Pinto, Ludwig, & Messmer, 2021). In Eastern Canada, there have been at least two attempts to reconstruct paleo-storm records. Oliva et al. (2018) presented a 800 years TC activity record from a barrier lake in Nova Scotia, while Yang et al. (2020) reconstructed 6500 years of tropical cyclones from a seafloor core from the Scotian Shelf, offshore Nova Scotia. While these two studies contributed substantially to understanding TC activity in Eastern Canada, more reconstructions are needed to increase the spatial coverage and to develop regional-scale understanding of long-term cyclone activity (Oliva, Peros, & Viau, 2017). A dense, high resolution network of paleo-storm records in Eastern Canada can help us identify conditions conducive to extreme weather, assess present-day and future risks as they pertain to cyclones, and define baselines to differentiate between natural and anthropogenic forcing of cyclones variability.

There is now a large body of knowledge and expertise in developing paleo-storm records using different types of coastal environmental archives. Recently, interest in using ombrotrophic peatlands as archives of past storm variability has increased, as these environments receive water and minerals exclusively through atmospheric deposition, making them excellent repositories of traces of atmospheric processes (Orme et al., 2017; Pratte, Garneau, & De Vleeschouwer, 2017). Aeolian particles (sea spray, dust, sand) deposited in ombrotrophic peatlands serve as proxies for past winds and are less affected by the complex variation in sea-level, post-depositional reworking, and availability of material that other widely used storm-wave proxies, such as marine over-wash layers in coastal lagoons, suffer from (Vandel et al., 2019). While this approach has been used in Europe, it has not yet been employed in Eastern Canada, despite the presence of many suitable sampling sites (Pratte et al., 2017). There is a need, therefore, to push paleotempestological research in Eastern Canada, both by establishing the suitability of ombrotrophic peatlands as archives of past storm variability, and deepening our understanding of the relationship between climate change and storm activity.

This thesis aims to take stock of paleo-storm research along the margin of the Northeast Atlantic Ocean and to understand the relevance and significance of paleo-storm records in Eastern Canada, while contributing to paleotempestology by presenting a new paleo-storm record from the Magdalen Islands, in the Gulf of St. Lawrence. In the literature review (Chapter 2), I introduce the climatology of storms and discuss the climatic causes, both natural and anthropogenic, of these events. Then, I review the numerous types of methods employed in paleotempestology, before giving an overview of the current state of paleo-storm research in the North Atlantic based on an analysis of 92 paleo-storm records. The literature review thus establishes knowledge gaps in paleotempestology and leads to my research questions and objectives (Chapter 3). Chapter 4 is a research manuscript based on the analysis of two composite sediment cores extracted from two ombrotrophic peatlands from the Magdalen Islands, Québec, a small archipelago of eight islands located in the Gulf of St-Lawrence, between Prince Edward Island and Newfoundland. In the manuscript, I examine the evolution of the peatlands, as well as local climate on the Magdalen Islands during the past 4000 years and reconstruct storms during the past 1000 years. In Chapter 5, the thesis ends with general conclusions drawn from the literature review and the research article and outlines possible directions for future research.

## **CHAPTER 2: Literature review**

### **2.1 Introduction**

This literature review is divided in three sections. In the first section, I introduce the climatology of storms, including TCs and ETCs, in the North Atlantic generally, but also their characteristics which are specific to Eastern Canada. The current knowledge of the causes of annual and decadal variability in these events is discussed, as well as the implications for current and potential impacts of climate change on storms. In the second section, I give an overview of the usual steps of reconstructing a paleo-storm record. The different types of methods based on storm-related processes of interest in paleotempestology, i.e., storm surge, wind, precipitation, and wave shear stress, are summarized. The third section comprises an analysis of 92 paleo-storm studies from the North Atlantic region – including North America, the Caribbean, Central America, and Europe – published between 2000 and 2022. Finally, the fourth section reviews the current knowledge on long-term, multimillennial trends in TCs and ETCs in the North Atlantic.

### **2.2 Climatology of tropical and extratropical cyclones**

#### *2.2.1 Definition of TCs and ETCs*

Tropical cyclone is the general term used to describe convective low-pressure systems (cyclones) that form over tropical or sub-tropical waters, with sustained high-velocity winds, which acquire energy from the evaporation of ocean water (Marks, 2015). TCs are distributed throughout the Pacific, Indian and Atlantic oceans; in the western North Atlantic region, peak activity occurs between August and October. These North Atlantic TCs, sometime called hurricanes if above a certain wind velocity threshold, usually form in the warm waters around Cape Verde as a tropical disturbance off western Africa just north of the equator, in the Atlantic Main Development Region (AMDR) (Figure 2.1) (Marks, 2015). From there, the storm systems travel westwards to the northeastern coast of South America, Central America, the Caribbean, or the east coast of North America, where they intensify into a tropical cyclone and sometimes make landfall, or recurve towards the north (Colbert, Soden, Vecchi, & Kirtman, 2013). Extratropical cyclones, on the other hand, are a dominant weather feature in mid and high latitudes in both hemispheres and are the

main energy transport system from the tropics to the poles (Joly, 2015; Raible et al., 2021). ETCs usually acquire their energy from the temperature gradient present at the polar fronts, which separate the air masses of the cold polar latitudes from the warmer mid-latitudes (Raible et al., 2021). In the Northern Hemisphere, over North America and Europe, storms form along the polar jet stream and travel eastward, with peak intensity during the fall and winter (Feser et al., 2015). While both TC and ETC systems are characterized by a low-pressure center and high-velocity winds, the strongest winds of TCs are usually near the surface, whereas for ETCs, they are usually located at higher altitudes, near the boundary between the troposphere and the stratosphere (Marks, 2015). TCs, when travelling in the mid-latitudes, can sometime acquire attributes of ETCs in a process called extratropical transition (Figure 1), and vice-versa; both phenomena are not completely mutually exclusive (Hart & Evans, 2001).

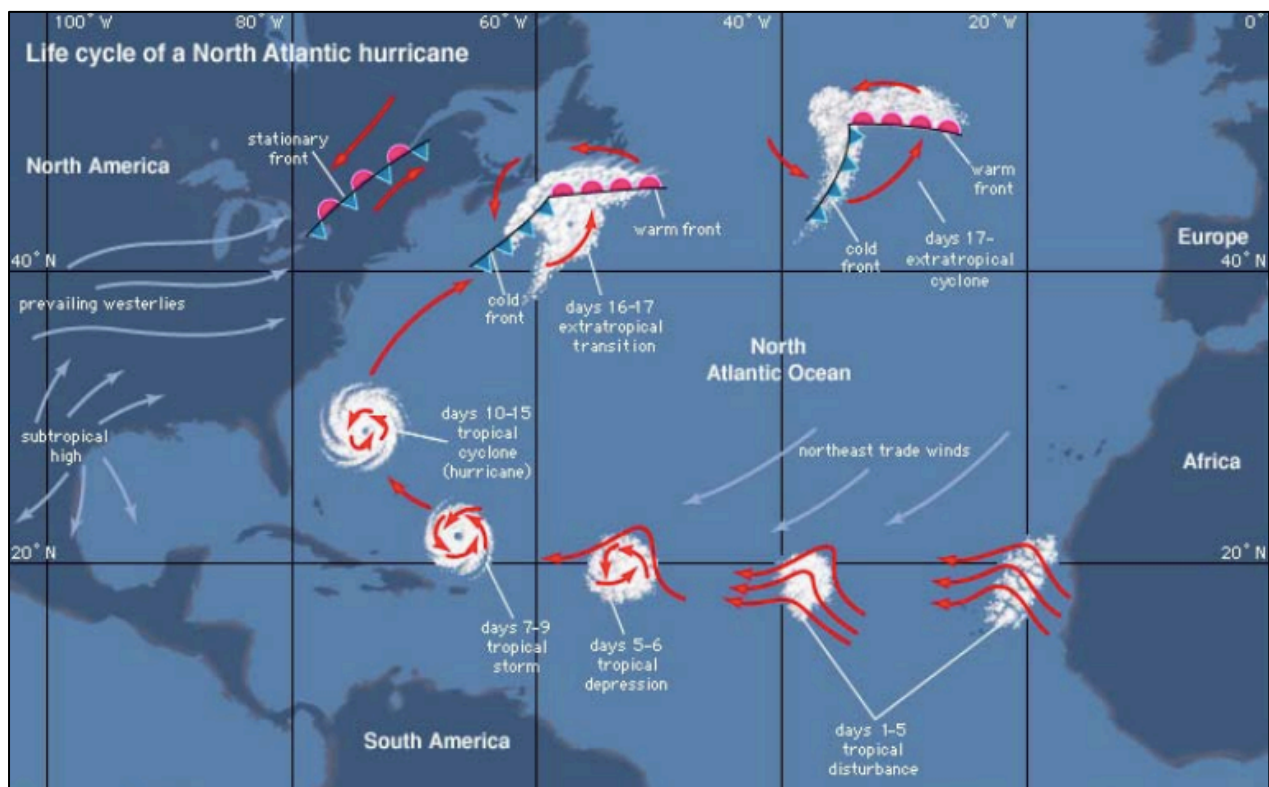


**Figure 2.1** Life cycle of a Cape Verde hurricane, from the formation of a tropical disturbance off the coast of West Africa, to its intensification into a tropical cyclone in the eastern North Atlantic Ocean, and finally to the weakening of the tropical cyclone and extratropical transition. Figure taken from the NOAA website ([https://www.nhc.noaa.gov/outreach/presentations/2013\\_02nhcL311\\_hurricaneLifeCycleHazards.pdf](https://www.nhc.noaa.gov/outreach/presentations/2013_02nhcL311_hurricaneLifeCycleHazards.pdf)). (Cangialosi, 2012).

### 2.2.2 TCs and ETCs in eastern Canada

Eastern Canada, especially the Maritimes, is located at the northwestern margin of the North Atlantic TC tracks (Figure 2.2A) and has been struck repeatedly by severe tropical storms and even hurricanes (e.g. Hurricane Juan struck Nova Scotia in 2003 (McTaggart-Cowan et al., 2006); Hurricane Igor struck Newfoundland in 2010 (Masson, 2014); Hurricane Dorian struck Nova Scotia in 2019 (Ezer, 2020); Hurricane Fiona swept through the Maritimes in 2022 (Insurance Bureau of Canada, 2022)) (Oliva et al., 2018). TCs travel northwards, general parallel to the east coast of North America until they eventually reach Canada, and are especially intense in the fall due to the strong sea-land temperature contrast (Plante, Son, Atallah, Gyakum, & Grise, 2015). In Eastern Canada, TCs forming in the AMDR are usually more intense in terms of wind velocity compared to ETCs, although the latter are much more frequent and can also be very destructive, especially when associated with stationary patterns of extreme rains, which can lead to excessive flooding (Francis & Vavrus, 2012). The Atlantic coast is particularly vulnerable, as ETCs usually remain weak over western and central Canada, until they intensify over the Maritimes due to greater moisture supply from the Atlantic Ocean (Figure 2.2B) (Plante et al., 2015). Storm surges and flooding associated with high-velocity winds are the main vulnerabilities along the coast, both of which may become more severe with future sea level rise (Bernatchez et al., 2008; Danard, Munro, & Murty, 2003; Forbes, Parkes, Manson, & Ketch, 2004).

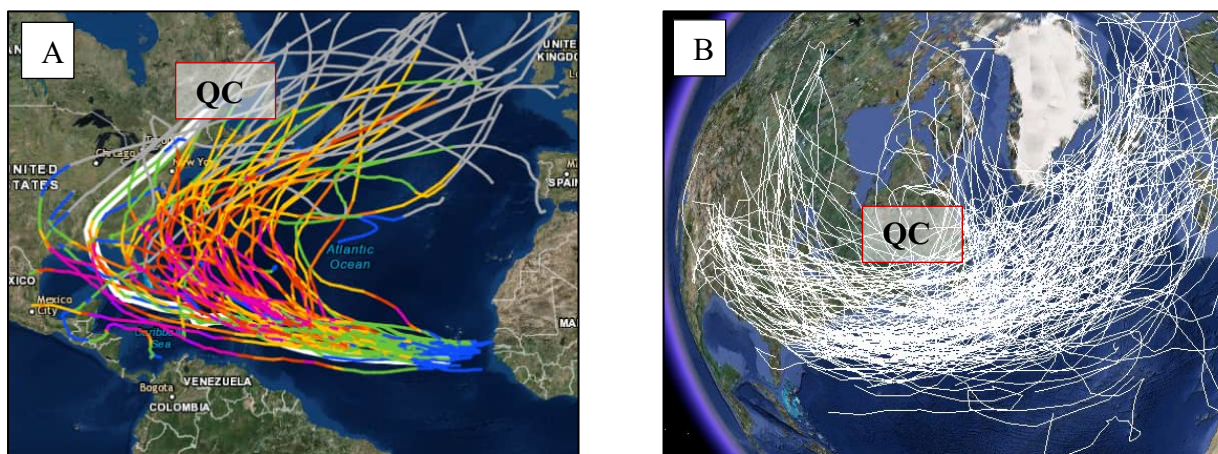


**Figure 2.2** A) Hurricane (TC) tracks from 1850-2020 from the IBTrACKS dataset (Knapp, Kruk, Levinson, Diamond, & Neumann, 2010). B) Extratropical cyclone (ETC) tracks from 1989 to 2009 from the ERA-Interim reanalysis dataset [30]. The location of the province of Québec, Canada is indicated as QC.

### *2.2.2 Temporal variability of TCs and ETCs*

The main drivers of TC and ETC genesis and intensification are strong temperature gradients (baroclinicity), mostly in the form of land-sea and latitudinal temperature contrasts, and evaporation due to latent heat release (Aryal, Villarini, Zhang, & Vecchi, 2018; Knutson et al., 2019). The distribution and intensity of baroclinicity (temperature and pressure contrasts in the atmosphere) and sea surface temperatures vary over time according to changes in climate modes, which themselves vary or oscillate on decadal or multi-decadal timescales (Raible et al., 2021). Therefore, the frequency, intensity, position of the storm track, and thus the vulnerability of specific regions to storms also fluctuate on annual, decadal, and even longer timescales in relation to climate modes (Bhatia et al., 2019; Cohen et al., 2014). One of the most influential climate modes of Atlantic cyclone activity is the North Atlantic Oscillation (NAO), which is a fluctuation in the difference of atmospheric pressure between the Icelandic low pressure region and the Azores high pressure region (Feser et al., 2015). In winter, the large difference of pressure between the regions [positive NAO index (NAO+)] is conducive to the formation of extratropical cyclones in the North Atlantic, while a small difference in pressure [negative NAO index (NAO-)] leads to weak cyclonic activity, and the sign and strength of the NAO fluctuates on a decadal scale. Variations in SSTs associated with the Atlantic Multidecadal Variation (AMV) and the El-Niño Southern Oscillation (ENSO) also play a role in cyclonic variability (Frajka-Williams, Beaulieu, & Duchez, 2017; Kossin, Emanuel, & Vecchi, 2014). These latter large-scale systems describe the shifting position of warm pools of oceanic water over decades, although the exact nature of the teleconnections between those systems and North Atlantic cyclones is not well understood (Aryal et al., 2018).

### *2.2.3 Impacts of climate change on TCs and ETCs*

While there has been an improvement in understanding and predicting cyclone variability due to anthropogenic climate change (e.g. Bhatia et al., 2019; Colbert et al., 2013; Knutson et al., 2019), the decadal fluctuations caused by changes in climate oscillations complicate the detection of any trends related to anthropogenic forcing (Knutson et al., 2010). Most scientists agree that increasing CO<sub>2</sub> in the atmosphere will play an important role in changing the intensity, frequency and distribution of cyclones in the 21<sup>st</sup> century (Colbert et al., 2013). According to a recent review by Knutson et al. (2020), there is high confidence that increasing sea-level will lead to higher coastal

inundations; medium-to-high confidence that global average TC precipitation rate and TC intensity will increase; and mixed confidence that global TC frequency will decrease, while very intense TC frequency will increase. A dangerous trend in rapid intensification of tropical cyclones is already observed in instrumental data for the North Atlantic region (Bhatia et al., 2019). Additionally, a poleward migration of intense hurricanes is observed, in relation to an expansion of the Inter-Tropical Convergence Zone (ITCZ) (Kossin et al., 2014). At mid- and high-latitudes, changes in the extent of summer sea-ice and the rapid warming of Arctic air masses may interact with the storm track and the polar jet stream, albeit in unpredictable ways (Cohen et al., 2014). Examination of reanalysis data revealed that winter cyclones increased in the Canadian Arctic while they decreased in southern Canada during the second half of the 20<sup>th</sup> century (Wang, Wan, & Swail, 2006), consistent with a decrease in baroclinicity at mid-latitudes and a northward shift of the polar jet stream (Feser et al., 2015). Nevertheless, the short length of historical and instrumental observations prevents us from significantly improving our understanding of the relationship between climate change and storms, underlining the need to extend the storm record beyond the instrumental period.

## **2.3 Paleotempestology: definition and methods**

### *2.3.1 Site selection and types of natural archives*

The basic principle behind paleotempestology is to identify and to date evidence for storms in the geological record using geological proxy data (Hippensteel, 2010). The usual sequence when reconstructing a paleo-storm record is first to choose the environment or site from which the natural archive will be extracted (Figure 2.3). Potential sites are determined by the location of the zone of influence of a storm, which usually comprises most coastal areas where cyclones make landfall, as well as the inland trajectories and zones of impact, but also offshore areas that are on the cyclone's trajectory before landfall. Second, once a site is selected, we need to extract a temporally continuous core or successive samples from a natural storm archive. Each of the aforementioned sites offer many natural storm archives to choose from, including sediments from lakes, sinkholes, peatlands, and wetlands; sediments from tidal systems like salt marshes, lagoons and estuaries; sediments from offshore blue holes (marine sinkholes) and basins; cores or samples from the barrier environment (beach) and dune fields; and growth rings from speleothems and

trees, among others (Figure 2.3). Third, from the core or samples, we need to detect the storms' signature. Some common sedimentary storm signals include beach ridges and scarps, washover fans and sheetwash, aeolian sand and marine aerosols, coarse sediment layers and turbidites (turbidity markers), and storm precipitation that exhibits a specific isotopic signature. The basic principle here is to identify sedimentary deposits indicative of high-energy events that stand out from the natural background (Engelhart, Pilarczyk, & Rovere, 2019). The methods to measure the storm proxies include grain-size analysis, aeolian sand influx, organic matter analysis, and micropaleontological analysis (e.g. counts of benthic foraminifera, marine dinoflagellate cysts, marine diatoms); geochemical analysis (e.g. analysis of the terrigenous elements Ti, K, Fe, or of the marine aerosol elements Br, Cl, Sr); stable isotopic geochemical analysis (e.g. oxygen, carbon or nitrogen isotopes); and tree-ring width measurements, among others (Oliva et al., 2017). Finally, the core or samples are adequately dated or chronologically constrained to produce the paleo-storm record. Additionally, it is possible, when the storm proxies extend to the historical data period, to compare the proxy record with an instrumental record of storms to confirm the relationship between the proxies and the event of interest.

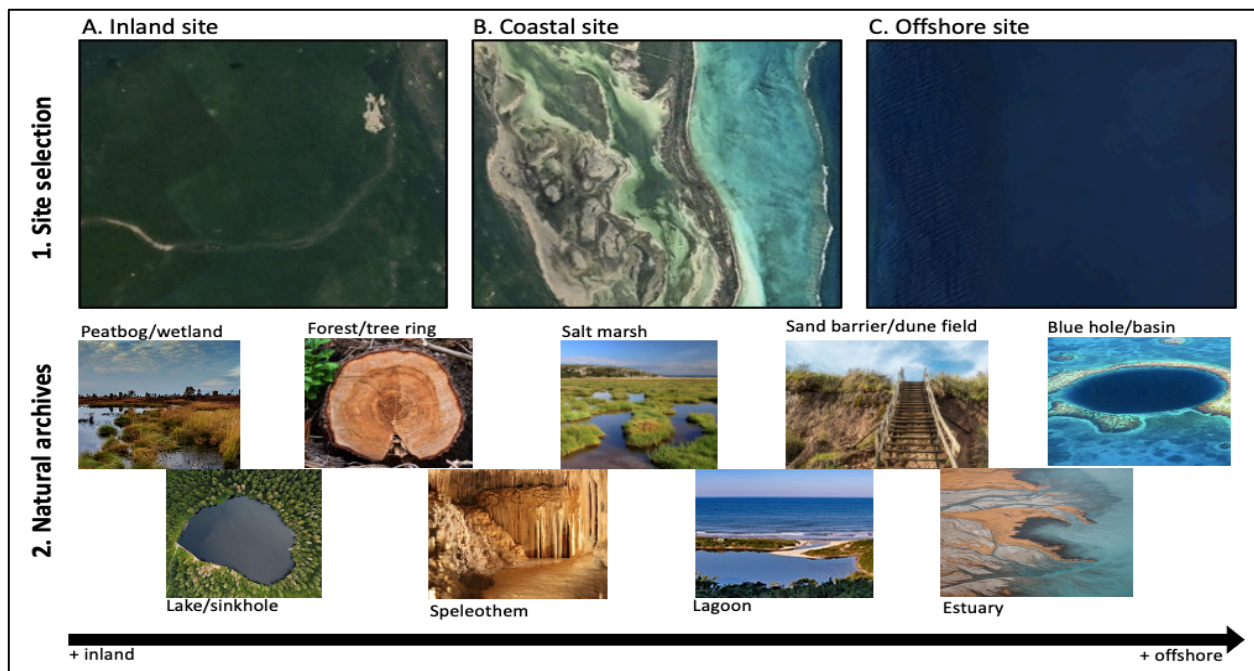


**Figure 2.3** Potential sites (inland, coastal, and offshore) for paleo-storm studies (1) and examples of natural archives along an inland-offshore gradient (2). Natural archives from peatlands/wetlands, lakes/sinkholes, salt marshes, lagoons, and blue holes/basins usually consist of sediment cores. Natural archives from forests/trees and speleothems use chronologically successive growth rings or layers. Natural archives from beach berms/ridges are usually chronologically successive samples from a sequence of berms or ridges.

### 2.3.2 Aspects of storms relevant to paleotempestology and related storm proxies

In this section, I will describe in more detail the different aspects of storms that are relevant to paleotempestology, that is, the storm surge, storm winds, the wave shear stress, and storm precipitation, and the specific storm proxies and paleo-storm reconstruction methods related to each of these storm aspects (summarized in Figure 2.4).

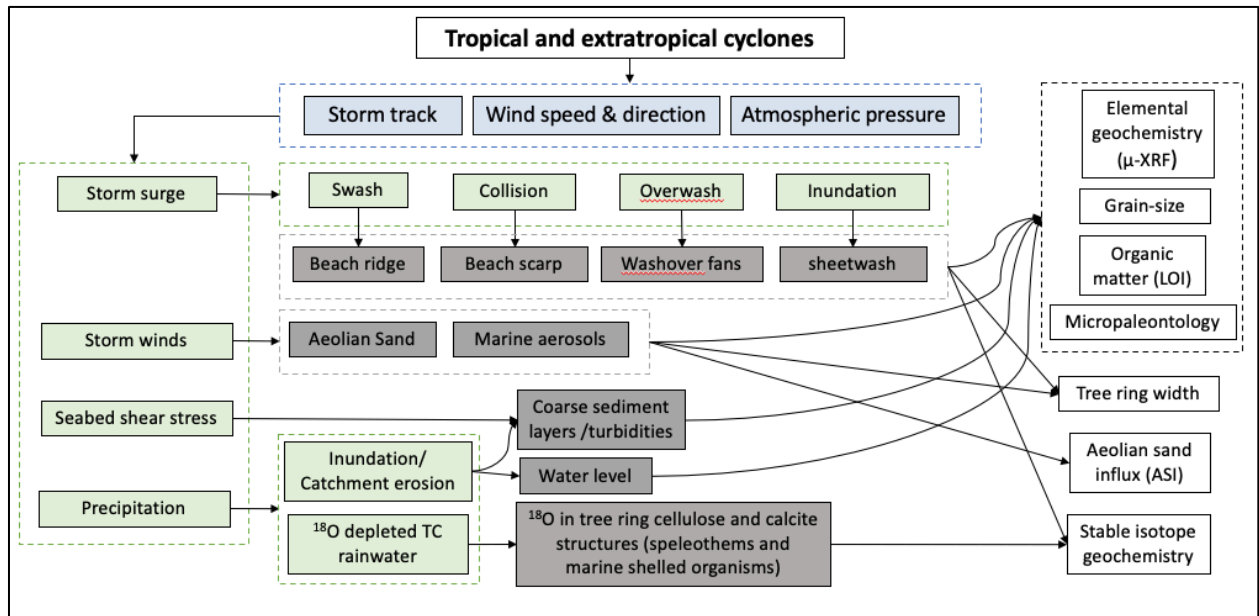


**Figure 2.4** Schematic of the relationships among storm characteristics and processes, storm proxies and methods. Blue boxes: storm characteristics; green boxes: storm-related processes of interest in paleo-storm research; grey boxes: storm proxies; white boxes: methods to identify and measure the storm proxies. Modified from Masselink and van Heteren (2014).

*Storm surges* – Storm surges are caused by short-term variations in the height of the ocean surface related to TCs and ETCs (Chaumillon et al., 2017). The increase of the sea-level during these events is due to a decrease in atmospheric pressure and an increase in wind stress on the sea surface (Chaumillon et al., 2017). Masselink and van Heteren (2014) provides a detailed description of the onshore storm wave regime, which are summarized in Figure 2.5 from Goslin and Clemmensen (2017); they define four types of wave impacts related to different types of storm surge sedimentation processes. The first two, the swash and collision regimes, are responsible for the formation of beach ridges and scarps (Rodriguez, Yu, & Theuerkauf, 2018). Beach ridges form when high-energy waves deposit coarse sediments on the backshore of the beach (Figure 2.5A) (Goslin & Clemmensen, 2017). These beach ridges are later isolated by progradation processes, i.e., the growth of the coastline further out into the sea and are arranged in a parallel sequence on

the coast (Goslin & Clemmensen, 2017; Scheffers, Engel, Scheffers, Squire, & Kelletat, 2012; Tamura, 2012). After successfully dating and mapping the succession of beach ridges, it is possible to extract information on ancient storm intensities by looking at the beach ridge elevation and comparing it to ancient sea-levels (Goslin & Clemmensen, 2017). Beach scarps, on the other hand, are formed by waves excavating the beach wall through repeated wave collisions. During storm events, the top layer of the scarp often breaks and is re-deposited on the beach, preserving the storm signature as coarse-grained concentrated material sheets that is then buried by finer material deposited post-storm (Figure 2.5B) (Buynevich, FitzGerald, & Goble, 2007; Goslin & Clemmensen, 2017). Identifying and mapping beach scarp features is more difficult compared to using beach ridges, but the advent of ground penetrating radar has simplified this process (Goslin & Clemmensen, 2017). As discussed by Moskalewicz, Szczuciński, Mroczek, and Vaikutienė (2020) and Buynevich et al. (2007), beach ridges and scarps tend to record only maximum intensity events. For example, Williams (2013) was not able to detect trends in storm variability in their beach ridge sediment core from southwestern Louisiana, but was able to detect the signature of very intense, but infrequent, storms.

The two other types of storm wave impact regimes, the overwash and inundation regimes, occur when the foredune is partially breached (overwash) or completely submerged by waves (inundation), which leads to the erosion of the foredune and the accretion of sediments landward in the backbarrier environment (the area located between the mainland and the most seaward part of the barrier (Goslin & Clemmensen, 2017)) (Figure 2.5C-D) (Goslin & Clemmensen, 2017; Masselink & van Heteren, 2014; Rodriguez, Theuerkauf, Ridge, VanDusen, & Fegley, 2020). The storm signature – the high energy sediment layer – is then covered by sediments resulting from subsequent low-energy sedimentation processes, thus preserving the trace of the storm in the sediment record. Backbarrier landscapes include landforms created by low energy processes that favor sedimentation such as lagoons, salt marshes and brackish features such as wetlands and ponds. Storm waves that breach the barrier only locally (overwash) result in a small deposit of limited extent in the backbarrier environment, known as a washover fan (Figure 2.5C) (Chaumillon et al., 2017). In case of inundation, i.e., when storm waves are much higher than the barrier, thus causing a general overtopping of the barrier (Figure 2.5D), sediment deposition happens in extensive sheets of sediments known as sheetwash (Figure 2.5D) (Goslin & Clemmensen, 2017). Storm wave inundations of the backbarrier environment have more widespread consequences on

the local topography and ecology compared to storm wave washover (Goslin & Clemmensen, 2017). Overall, backbarrier environments such as lagoons or salt marshes tend to record only high intensity events that create storm surges large enough to overtop, either partially or fully, their barriers (Donnelly, Bryant, et al., 2001; Donnelly, Roll, et al., 2001; Scileppi & Donnelly, 2007). It is possible to reconstruct past storms from these environments by taking sediment cores and identifying the washover sequences interbedded between fine-grain or organic sediments. Saltwater intrusions during overwash events are also a good storm proxy, and they can be identified by looking at the concentration of chemical elements indicative of salt-water along the sediment core such as bromine, chlorine, calcium, or strontium (Goslin & Clemmensen, 2017). Micropaleontological analysis can also indicate barrier breaching and saltwater intrusion into the backbarrier environment, for example by examining foraminifera (small shelled amoeba) deposits (Oliva et al., 2017).

The major limitation of reconstructing paleo-storm records from storm surge proxies is the difficulty in ascertaining the sensitivity of a given site to swash, collision, overwash and inundation. Coastal environments are highly dynamic landscapes and their sensitivity to storms will change over time (Donnelly, Bryant, et al., 2001; Donnelly, Roll, et al., 2001). For example, because beaches and foredunes are composed of unconsolidated sediments, beach ridges and scarps are not highly resilient to changes in sea-level rise, which complicates the evaluation of a site's sensitivity to storms (Rodriguez et al., 2018). Some landforms, particularly salt marshes, have significant spatial heterogeneity, meaning that the impact of a storm is not uniform across its surface (Castagno, Donnelly, & Woodruff, 2021). In this case, it is best to sample in multiple areas to capture the spatial variability (Castagno et al., 2021). Coastal landscapes usually take several decades to recover from intense storms, which may decrease their capacity to record events happening in close temporal proximity (Nikitina et al., 2014). During their recovery, submerged environments such as brackish ponds, lagoons or estuaries are affected by tidal processes such as the scouring and reworking of bottom sediments, which may disturb the storm sediment layer (Adomat & Gischler, 2017). The older the event, the more likely it has been affected by tidal processes, which creates a bias towards the preservation of more recent events in any sedimentary core record at the expense of older events (Adomat & Gischler, 2017).

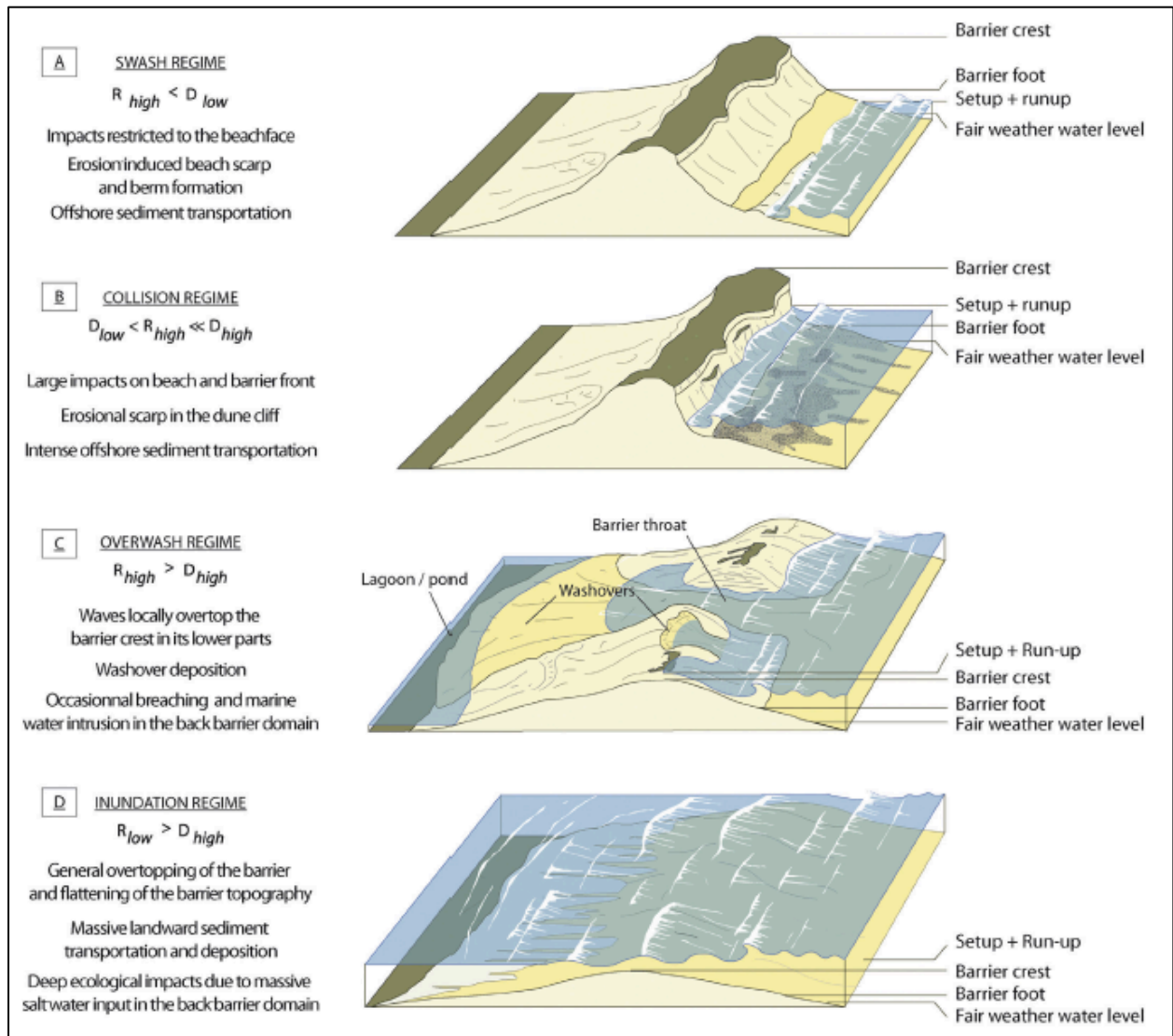


**Figure 2.5** Schematic illustration of the four storm surge regimes from Masselink & van Heteren (Masselink & van Heteren, 2014) and impacts on coastal barrier systems.  $D_{low}$  and  $D_{high}$  refer to the position of the height of the barrier foot and crest, respectively.  $R_{high}$  refers to the highest action of the waves, while  $R_{low}$  refers to the lowest position of the storm wave setup. Figure from Goslin and Clemmensen (2017).

*Storm winds* – Sustained high-velocity winds are a central characteristic of storms, and wind events have long been recognized as important factors contributing to changes in coastal geomorphology (Delgado-Fernandez & Davidson-Arnott, 2011). There are two main approaches related to storm wind processes used in paleo-storm reconstructions: the aeolian sand influx (ASI) and core geochemistry, both based on the transport of particles from coastal environments that are deposited further inland in coastal peatlands, lakes, and sinkholes (Figure 2.4) (DeVries-Zimmerman, Fisher,

Hansen, Dean, & Björck, 2014). The concept of ASI was developed by Björck and Clemmensen (2004) and is based on the relationship between mineral grain size, wind stress and transport competence. These elements determine the magnitude of winds able to transport grains of different size classes. The choice of a grain size threshold will depend on different factors such as source-sink distance, sediment source availability, local geomorphology, and ecology, and whether wind transport is through creeping and saltation (particles drifting or rolling on or close to the surface, which happens at a lower wind threshold) or suspension (which necessitate a high wind threshold, for example during intense storms). As an example, Goslin et al. (2019) calculated ASI based on the assumption that sand particles > 125- $\mu\text{m}$  in diameter require winds > 78 km/h to be transported in suspension. In the winter, the presence of snow and ice in the leeward side of the dune can serve as an even platform on which sand and other sediment particles can travel greater distances before being trapped in the snow and released to the surface when it melts (DeVries-Zimmerman et al., 2014). The geochemical approach was developed more recently with the advent of new analytical tools like the ITRAX Core Scanner, which uses micro-x-ray fluorescence ( $\mu\text{-XRF}$ ) to quantify the elemental composition in sediment cores (Croudace & Rothwell, 2015). Elements of interest include terrigenous elements (e.g., Ti, Fe, K, Zr in sand dunes), but also marine-derived elements such as Br, Cl, Na, Sr, or S. Indeed, the violent swash and collision of waves with the coast during storm events also leads to the creation of marine aerosols, which can be transported further inland by the same processes described above (Gustafsson & Franzén, 2000). The geochemical approach is very effective at detecting small concentrations of allochthonous materials that are used as storm proxies and, as such, can be used to identify events of different intensity, from long-range transport of atmospheric dust (Pratte et al., 2017) to intense storms (Orme, Davies, & Duller, 2015).

The main challenge of reconstructing paleo-storm records from storm wind proxies is the difficulty in ascertaining the source of the prospective storm-deposited sediment or element (Kylander et al., 2020). A good understanding of the geomorphology of the surrounding potential sediment sources at a site and their histories is paramount, as the storm signal will depend on factors such as the distance between sediment source and sink, the volume and availability of sediment, and the surface (vegetation) cover (Nielsen, Dahl, & Jansen, 2016). Testing the elemental composition of possible sources of sediments can help ascertain the aeolian origin of potential paleo-storm markers (Goslin et al., 2018).

*Seabed shear stress* – Seabed shear stress is a consequence of surface water winds and waves at shallow and intermediate depths (Myrhaug, 2017). Winds of all strengths create surface waves, and the water movement induced by those waves propagates in the entire water column (Myrhaug, 2017). Turbulence in the water column can induce bottom current which, under fair weather conditions, usually flows over the seabed as laminar flow, i.e., in paths parallel to the seabed, especially over surface that offer a smooth surface like mud beds (Myrhaug, 2017). The friction between these bottom currents and the seabed is known as seabed shear stress. During storm events, strong surface winds will induce large waves, which will propagate to the seabed as intense turbulence, thus disrupting the laminar flow above the seabed. The increased turbulence at the boundary layer leads to an increased seabed shear stress, which creates a distinctive bottom sediment layer associated with high turbidity (Figure 2.4) (Myrhaug, 2017). Once the sediments are in suspension in the water column, they can be transported over a basin or blue hole, where they will be deposited, resulting in a distinctive sheet of coarse sediments indicative of a storm event interbedded between finer undisturbed sediments resulting from background, fair weather sedimentation (Gischler, Shinn, Oschmann, Fiebig, & Buster, 2008; Yang et al., 2020). After obtaining a core from these environments, it is possible to identify the storm layers by traditional techniques such as grain-size and micropaleontological analysis (Gischler et al., 2008).

Reconstructing paleo storms from seabed shear stress proxies offer some advantages: in the case of blue holes, for example, the high background sedimentation rate promotes the quick isolation of discrete storm event beds within background sedimentary layers (van Hengstum et al., 2014). Additionally, blue holes can be stable environments that are less prone to post-storm reworking of sediments and be less affected by processes such as sea-level change and coastal geomorphological dynamics, thus promoting the long-term conservation of storm signals in the sediment layers (van Hengstum et al., 2014). As discussed by Toomey, Curry, Donnelly, and van Hengstum (2013), sedimentation in some blue holes has been shown to be stable over periods of millennia, meaning that blue hole sediments can preserve storm signatures at a high resolution for periods going back as far as the early Holocene. Nevertheless, one must consider confounding factors such as possible sub-sea connections and coral reef dynamics. One must have a good knowledge of the local water currents (both regular and storm-induced), and the necessary wind speed that will be able to create bottom currents capable of suspending and transporting sediments (Toomey et al., 2013).

*Precipitation* – Another characteristic of storms, both tropical and extratropical cyclones, is that they are often associated with extreme amounts of precipitation. One useful feature of heavy storm precipitation in the tropics is that it is usually depleted in the heavy isotopes of oxygen  $^{18}\text{O}$  and deuterium  $^2\text{H}$  relative to normal local precipitation, meaning that tropical cyclones have a unique isotopic signature (Figure 2.4) (Lekshmy, Midhun, Ramesh, & Jani, 2014; Oliva et al., 2017). Negative isotopic values in TC rainfall are due to isotopic fractionation during precipitation, although the specific controls of that process are still poorly understood (Sun et al., 2022). Isotope-depleted water from tropical storms gets absorbed by different natural archives such as trees, stalagmites and other carbonate structures and organisms:  $^{18}\text{O}$ -depleted precipitation reaches speleothems via infiltration, by flooding the cave, or through streams (Frappier et al., 2014), whereas carbonate structures and trees absorb the  $^{18}\text{O}$ -depleted rainfall during calcite precipitation of shelled marine organisms and in tree-ring cellulose, respectively (Lane et al., 2017; Li, Labbé, Driese, & Grissino-Mayer, 2011). Once this isotopically specific signature of tropical storms is recorded in the various natural archives, it can be detected and measured by applying techniques such as stable isotope mass spectrometry (Kilbourne, Moyer, Quinn, & Grottoli, 2011; Lasas-Hernández, Medina-Elizalde, & Frappier, 2020; Li et al., 2011). Factors that can affect the sensitivity of speleothems, trees and carbonate structures to  $^{18}\text{O}$ -depleted precipitation include homogenization of tropical cyclone rain with surrounding groundwater and sea water, and diffusion and dispersion of  $^{18}\text{O}$  atoms during filtration from the surface to the speleothems or tree roots (Frappier, Sahagian, Carpenter, González, & Frappier, 2007; C. S. Lane et al., 2017).

The main advantage of working with  $^{18}\text{O}$ -depleted precipitation proxies, such as speleothems and tree-rings, is the possibility of also extracting a companion robust and accurate chronology of storm events with a very high resolution due to the nature of these archives (Baldini et al., 2016; Frappier et al., 2014). However, the storm records derived from these proxies are usually shorter compared to other types of records.

## **2.4 Overview of paleo-storm studies published since 2000**

In this section, I provide an overview and summary of the current state of paleotempestological research in the North Atlantic region based on 92 paleo-storm studies published since 2000

(Supplemental Table S1). These studies were obtained from Scopus after executing a search for articles with the term *paleo-storm* or *paleotempest* in their title or abstract. Additional studies were found through snowballing, i.e., by looking at the references of each relevant article identified in Scopus. This list is non-exhaustive, but it is representative of the variety of paleo-storm studies as described above, in terms of geographical distribution, climate archives, storm variables and analysis methods.

First, approximately two thirds (70%;  $n = 49$ ) of the studies identified are located in the western North Atlantic basin (27% in the Caribbean [ $n = 25$ ]; 26% in the southeastern US [ $n = 24$ ]; and 16% in the northeastern US/Canada [ $n = 15$ ]) (Figures 6 and 7A). The 28 records from the eastern North Atlantic basin (30%) are divided between northern Europe (20%;  $n = 18$ ) and western Europe (11%;  $n = 10$ ) (Figures 2.6 and 2.7A). These statistics underline the underrepresentation of European storm records in the North Atlantic compared to North American/Caribbean records. However, European records usually focus on records of ETCs as opposed to the North American/Caribbean records, whose focus is on TCs. TCs in North America/Caribbean have destructive impacts on local communities (Klotzbach et al., 2022), which may in part explain why they represent most of the records in the North Atlantic. Additionally, in the western North Atlantic basin, the northeastern US/Canada is also underrepresented, despite TCs having had destructive impacts in those regions as well (Oliva et al., 2018). The lack of paleostorm records along the northern limit of the hurricane track prevents us from studying long-term, large scale trends such as the poleward migration of TCs in the North Atlantic.

More than half of the records (54%;  $n = 50$ ) are using proxies whose storm signature is related to storm surges (Figure 7B). The other half of the records are divided between storm winds (22%;  $n = 20$ ), seabed shear stress (12%;  $n = 11$ ); and storm precipitation (12%;  $n = 11$ ). However, these storm-related processes are not represented equally between the regions: for example, most studies using wind-related proxies are in northern Europe (85%;  $n = 17$ ), and there are no records using precipitation- or seabed shear stress-related proxies in Europe (Figures 2.6 and 2.7C).

The temporal coverage of the studies varies between the last 23 years and more than 10,000 years, for an average record duration of 3215 years (Supplemental Table 1). The majority (76%;  $n = 70$ ) of the records cover at least the last 1000 years. Looking at the duration of the records by region, the Caribbean, western and northern Europe have highest number of long (>4000 years) records, and the northeastern US/Canada have the shortest record, for an average of

2520 years. This region, however, contains the longest records at 14,000 years (Parris, Bierman, Noren, Prins, & Lini, 2010).

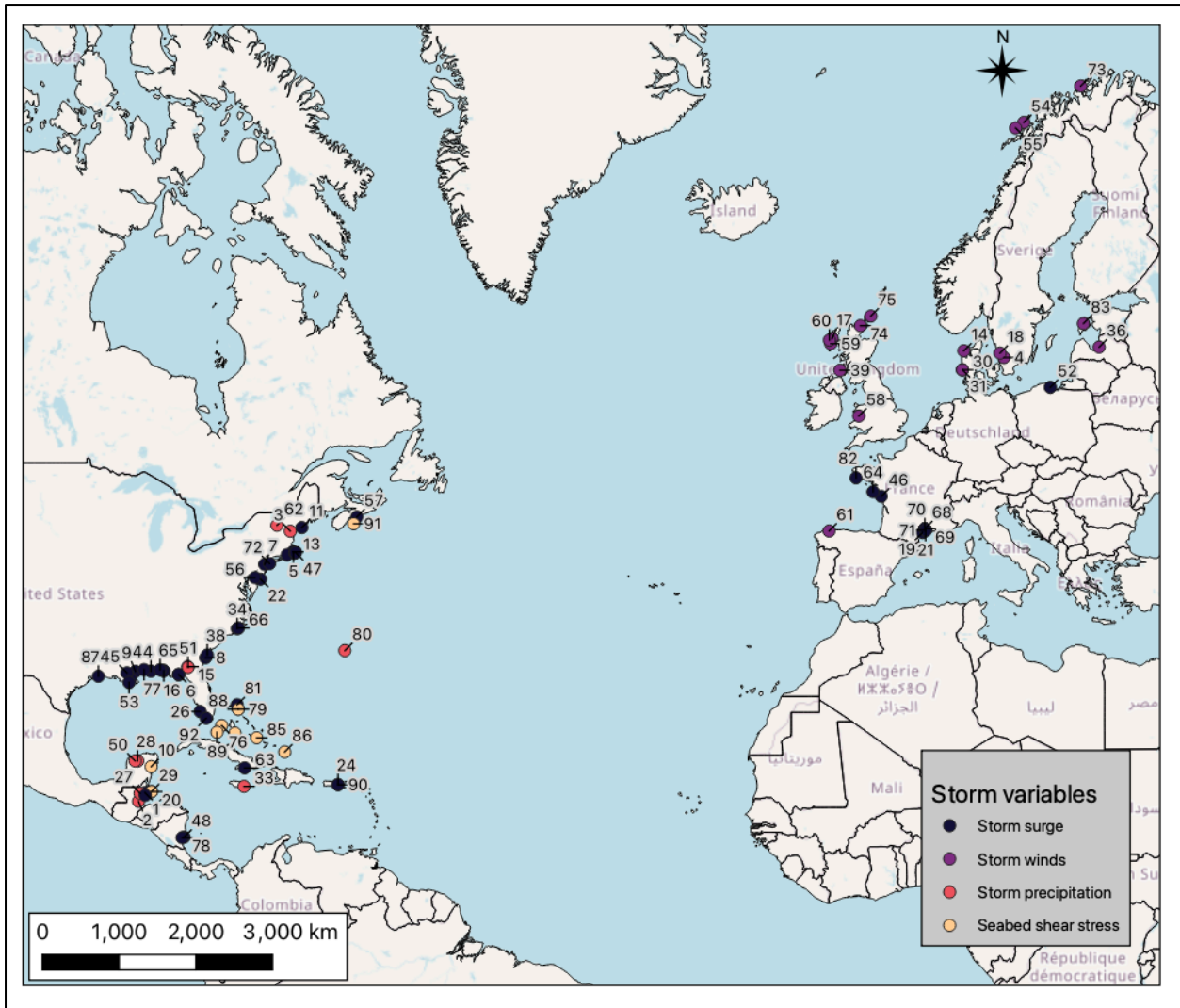


**Figure 2.6** Maps of the 92 paleo-storm studies across the North Atlantic. The studies are classified by the storm variable proxy type.

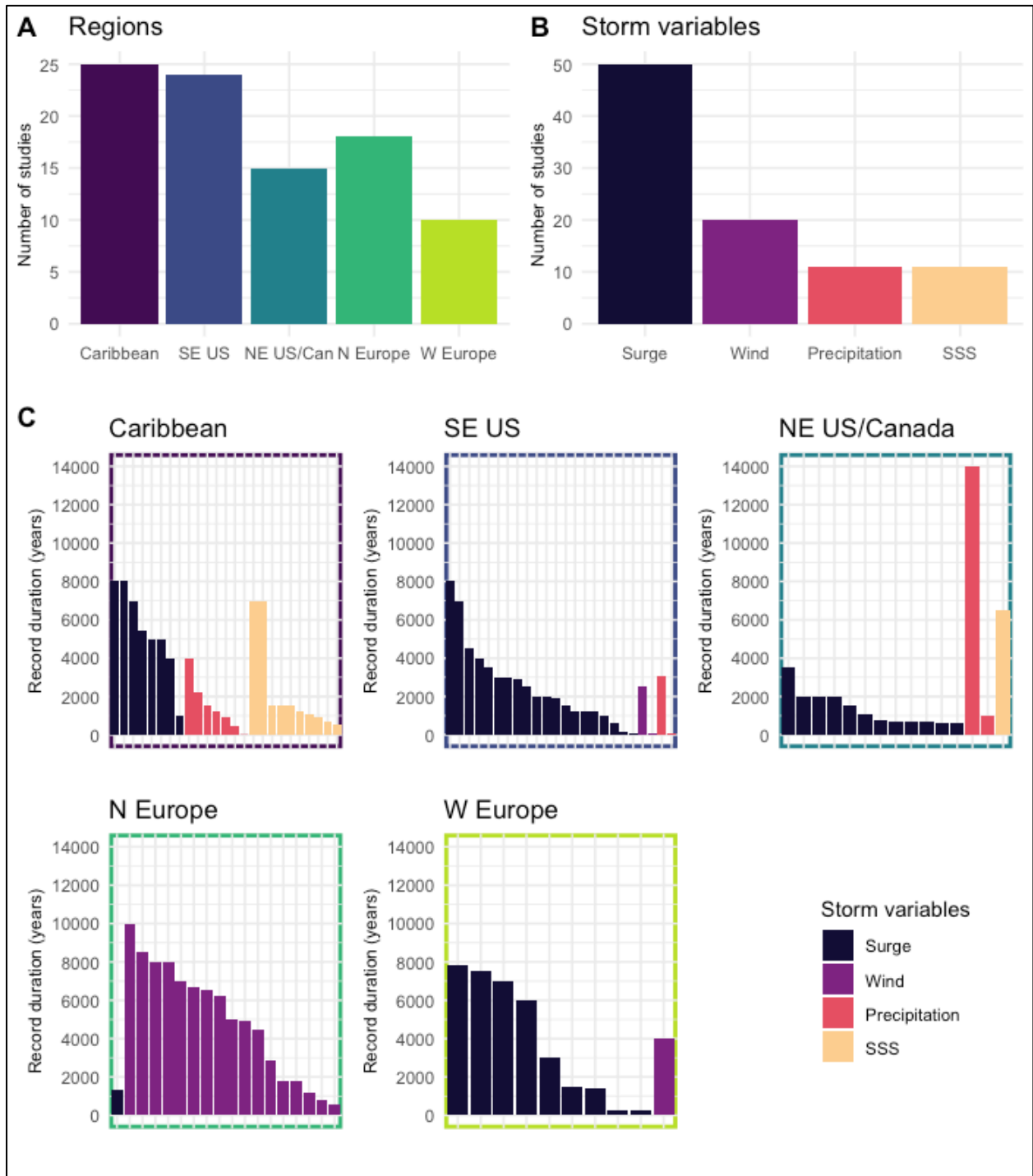


**Figure 2.7** A) Number of studies per region in the North Atlantic. B) Number of studies per storm variable examined. C) Duration of the records, from longest to shortest, per region in the North Atlantic and per storm variable examined.

## **2.5 Long-term perspective on tropical and extratropical cyclone variability**

### *2.5.1 Long-term TC trends*

As noted above, most paleotempestological research with respect to tropical cyclones has been conducted in the Caribbean and on the Southeastern US coast (Oliva et al., 2017), where a number of multi-millennial records of hurricane landfalls have been produced (e.g. (Adomat & Gischler, 2017; Brown, Reinhardt, van Hengstum, & Pilarczyk, 2014; Toomey et al., 2013)). Most of the reconstructions show that TC activity has not remained constant during the Holocene, but rather has manifested centennial- to millennial-scale periods of active versus calm phases (McCloskey & Liu, 2013). These phases often correlate with large-scale climatic modes and permit the identification of climatic forcing mechanisms related to increased TC activity. In general, conclusions about the relationship between climate and variation in TC regimes fall under two categories: 1) synchronous change across the North Atlantic related to basin-wide conditions favourable to cyclogenesis (Mann, Woodruff, Donnelly, & Zhang, 2009); and 2) asynchronous latitudinal change across the North Atlantic related to the changing position of North Atlantic circulation features, concentrating landfalls in different regions at different periods with no change in overall TC activity levels (McCloskey & Liu, 2012).

Evidence for synchronous, basin-wide variation in hurricane landfalls is summarized by Mann, Woodruff, et al. (2009). Based on a composite record of paleotempestological evidence of hurricane landfalls covering the western North Atlantic region and a statistical model of North Atlantic hurricane activity, they tied active landfall periods to higher SSTs in the AMDR and La Niña-like climatic conditions, both of which favor TC genesis. However, their sample of studies is not representative of basin-wide hurricane activity, preventing stronger conclusions from being drawn. Alternatively, McCloskey and Liu (2012) show a negative correlation between paleo-records of hurricane landfall in Central America (Nicaragua) and North America (Puerto Rico and the Atlantic coast) in the last 2500 years, pointing to a changing position of the hurricane track between the two regions. Donnelly et al. (2015) also point to asynchronous periods of intense TC activity between the Caribbean and the east coast of North America attributed to changes in local SSTs that steer hurricane tracks. More recently, however, studies seem to favor a mixed-model of generally calm versus active period of cyclogenesis coupled with variation in hurricane tracks (Ting, Kossin, Camargo, & Li, 2019). Yang et al. (2020) produced a 6500-year-long TC record

from the Scotian Shelf in Eastern Canada and found a possible oscillation between asynchronous and synchronous TC signal between low and high latitudes along the western Atlantic coast, wherein for some periods, variation in cyclogenesis across the whole western Atlantic basin is synchronous for both high and low latitudes, and for some other periods, cyclogenesis varies between high and low latitudes. Variation between synchronous and asynchronous periods occurs in concert with variations in the Atlantic meridional overturning circulation (AMOC), that itself mediates the impacts of other climate modes such as ENSO and the West African Monsoon (WAM). However, there are not enough long-term (>3000 years) paleo-storm studies at high latitudes to assess this hypothesis with confidence.

### *2.5.2 Long-term ETC trends*

While the Caribbean and Southeastern US coast have been the focus of tropical cyclone paleo-storm research, much less is known about past storm activity, for both TCs and ETCs, in and north of New England, especially in Canada (Oliva et al., 2017). To date, all paleoclimate research focusing on ETCs comes from western and northern Europe (Raible et al., 2021). The studies that focus on establishing a chronology of stormy periods in Europe all come to the conclusion that different locations were affected by a succession of more windy versus less windy periods, which more often than not coincide with variations in the NAO index (the storm track being situated in northern Europe during the positive NAO phase and in southern Europe during the negative NAO phase) (Pouzet et al., 2018). While the NAO index is often considered to be the key driver of European storminess during the instrumental period (e.g.: Wang, Zwiers, Swail, & Feng, 2009) and in short (< 1000 years) paleo-storm studies, the nature of the relationship between North Atlantic storminess and the NAO on longer (centennial to millennial) timescales is still debated. A review by Orme, Reinhardt, Jones, Charman, Barkwith, et al. (2016) focusing on the British Isles and the Norwegian coast suggests that storminess was closely related to the NAO index during the last 1000 years (on decadal timescales), while the relationship weakens when the last 4000 years are considered. These results raise the question as to whether the NAO is the major influence of storminess over centennial to millennial timescales. Recently, variation in insolation related to the Earth's orbit during the late Holocene was cited as being the primary driver of millennial change in storminess over Europe and a possible mediator in the relationship between the NAO index and storminess on shorter timescales (Goslin et al., 2019; Kylander et al., 2020;

Orme et al., 2017). In particular, a study by Orme et al. (2017) comparing two Holocene storminess reconstructions from northwest Spain and Scotland found that the storm track moved to a higher latitude from a more southern position over the past 4000 years. This is related to the gradual cooling of the polar region along with a warming in the mid-latitudes, resulting in an increased latitudinal temperature gradient and stronger polar vortex. This finding was corroborated by Goslin et al. (2019), who found a negative correlation between insolation and storminess in a core from Denmark. All these findings suggest a teleconnection between storminess, sea-ice extent, and the strength of the polar vortex, which may be then translated by climatic modes such as the NAO to affect storminess across the higher latitudes of the North Atlantic.

## **2.6 Conclusion**

In summary, the eastern region of Canada, especially the Maritimes, is affected by both tropical and extratropical cyclones. TCs and ETCs, despite having distinct geneses, are important hazards for coastal communities, especially in the perspective of increasing sea-level. TCs and ETCs are characterized by their frequency, intensity, and average position of their storm tracks, which are influenced by various climatic modes. Nevertheless, current knowledge on TCs and ETCs does not allow for a comprehensive understanding of the relationship between climatic modes and changes in TCs and ETCs, which prevents us from predicting the possible impacts of climate change on TCs and ETCs, especially at regional scales. In the following chapter, the knowledge gaps in paleotempestological research will be discussed, along with the thesis's research questions and objectives.

### **CHAPTER 3: Research questions and objectives**

The literature review (Chapter 2) highlights some gaps in paleotempestological research in the North Atlantic. First, records from the northeastern US/Eastern Canada are underrepresented; second, records from the northeastern US/Eastern Canada are on average covering a shorter period (going less far back into the Holocene) than records from other regions; and third, paleo-storm records based on wind-related proxies are almost absent from North American/Caribbean records. The necessity of producing a wind-based paleo-storm record from eastern Canada appears essential for two reasons. First, as most European (especially northern European) records are wind-based, developing wind-based storm records in North America would facilitate comparing the records from both regions and would help developing a more general understanding of storminess across the North Atlantic Ocean. Second, the relative scarcity of paleo-storm records in the northeastern US/Canadian region and the short duration of these records prevents us from deepening our understanding of long-term trends in TCs along the northern margin of the hurricane track and, consequently, of other basin-wide trends such as the poleward migration of the hurricane track. My research project, therefore, aims at filling some of these gaps and answering the following questions:

- Is it possible to detect a TC and ETC wind-related signature in ombrotrophic peat cores from eastern Canada?
- How has tropical storm activity – either caused by TCs or ETCs – varied during the Late Holocene on the Magdalen Islands in relation to climate?

The specific objectives of this thesis are: 1) to identify aeolian sediments in ombrotrophic peat bogs in the Magdalen Islands and to validate its relationship with wind-related storm processes; 2) to reconstruct a Holocene record of paleo-storms in the Magdalen Islands; and 3) to improve our understanding of the long-term northward shift of the hurricane track in the North Atlantic in relation to changes in climate modes, particularly the AMV.

## **CHAPTER 4: Research article manuscript**

**Title:** Peatland to the rescue! Late Holocene history of climate and storms as told by coastal peatlands on the Magdalen Islands, Québec, Canada

**Authors:** Antoine Lachance<sup>1</sup>, Matthew Peros<sup>2</sup>, Jeannine-Marie St-Jacques<sup>1</sup>

**Affiliations:** <sup>1</sup>Geography, Planning and Environment, Concordia University; <sup>2</sup>Geography and Environment, Bishop's University

## 4.1 Introduction

Tropical cyclones [TCs] and associated winds, storm surges and heavy precipitation are ever-present hazards for eastern Canadian coastal communities (Danard et al., 2003; Vasseur et al., 2007). Eastern Canada, especially the Maritimes region, is located at the northwestern margin of the North Atlantic TC tracks and has been struck repeatedly by severe tropical storms and hurricanes (e.g. Juan in 2003 (McTaggart-Cowan et al., 2006); Igor in 2010 (Masson, 2014); Dorian in 2019 (Ezer, 2020) and Fiona in 2022 (Insurance Bureau of Canada, 2022)) (Oliva et al., 2018). North Atlantic tropical storms, called hurricanes if above a certain wind velocity threshold, usually form in the warm waters around Cape Verde, in western Africa, just north of the equator (Marks, 2015). From there, storm systems travel westwards to the northeastern coast of South America, Central America, the Caribbean, or the east coast of North America, where they sometimes make landfall (Colbert et al., 2013). Some tropical cyclones travel northward along the east coast of North America until they eventually reach Canada (Plante et al., 2015). At a global scale, it is predicted that average TC precipitation and intensity will increase with anthropogenic climate change (Knutson et al., 2020). Nevertheless, the impacts of climate change on TC variability are still not well understood and have not been studied extensively in eastern Canada, despite the threat that they pose (Colbert et al., 2013; Knutson et al., 2019; Oliva et al., 2018).

Observational and modelling studies show that North Atlantic TC activity is largely influenced by strong temperature gradients (baroclinicity) mostly in the form of land-sea and latitudinal temperature contrasts, and evaporation due to latent heat release (McIlveen, 2010). The distribution and intensity of baroclinicity (temperature and pressure contrast in the atmosphere) and sea surface temperatures fluctuate on annual, decadal, and longer time scales according to changes in climate modes such as the North Atlantic Oscillation (NAO) and the Atlantic Multidecadal Variability (AMV) (Bhatia et al., 2019; Raible et al., 2021). Therefore, the frequency, intensity, storm track position, and the vulnerability of specific regions to TCs also vary in relation to these climate modes. In particular, changes in the AMV, which describes the alternating swing in North Atlantic sea surface temperatures (SSTs) over decades (Vecchi, Delworth, & Booth, 2017), has been related to a recent poleward shift of storm tracks in several studies (Baldini et al., 2016; Kossin et al., 2014; van Hengstum et al., 2016). Such a shift in storm tracks may well expose Eastern Canada to more extreme weather during this century, although the

exact nature of the teleconnections between those systems and North Atlantic cyclones is not well understood (Knutson et al., 2019).

We can improve our understanding of the relationships between climate and tropical cyclones in Eastern Canada by turning to paleoclimate archives. In coastal environments, tropical cyclones often leave a distinct signature indicative of high-energy events that are preserved in otherwise low-energy natural archives such as sediments, trees and carbonate structures such as stalagmites and corals (Engelhart et al., 2019). While many studies have sought to reconstruct paleo-storm records based on storm wave markers like beach ridges, beach scarps, and overwash fan deposits in backbarrier environments (Goslin & Clemmensen, 2017; Masselink & van Heteren, 2014; Rodriguez et al., 2020), this technique may be inadequate to accurately identify storms of lesser intensity, like the TCs that make landfall in Eastern Canada (Goslin & Clemmensen, 2017). Instead, in this study, we take advantage of the properties of ombrotrophic peatlands, which are widely distributed in the temperate and boreal regions of Eastern Canada (Payette & Rochefort, 2001). Ombrotrophic peatlands receive water and minerals mostly through atmospheric processes (Pratte et al., 2017). Aeolian particles (sea spray, dust, sand) deposited in ombrotrophic peatlands serve as proxies for high-velocity wind activity. The most widely applied method to reconstruct storms in these environments is to measure a peatland's variations in ash content and in sand-grain content, expressed as the Aeolian Sand Index (ASI) (Björckl & Clemmensen, 2004). Moreover, in the last decade, new techniques were applied to complement this approach, including x-ray microfluorescence core scanning (XRF-CS), which provides high resolution records of key elements related to detrital mineral inputs and sea spray (Kylander et al., 2020; Orme, Reinhardt, Jones, Charman, Croudace, et al., 2016). Despite these promising advances, limitations inherent to using ombrotrophic peatlands to study paleostorms may not be fully appreciated. Indeed, peatlands are complex environments, and a deeper understanding of their evolution and relationship with climate is key to better isolate the impact of storms from background variability. Additionally, analyses of ombrotrophic bogs in paleo-storm research has been mostly undertaken in Europe (e.g.: (Björckl & Clemmensen, 2004; Kylander et al., 2020; Orme, Reinhardt, Jones, Charman, Barkwith, et al., 2016; Stewart et al., 2017; Vandel et al., 2019)), where tropical cyclone hits are rarer, and applying these techniques to an ombrotrophic peatland in an area affected by TCs should provide important insights about the sensitivity of peatlands to these intense and rare events.

The Magdalen Islands are a small archipelago of eight islands located in the Gulf of St-Lawrence, in Eastern Canada. Being located at the northwestern margin of the North Atlantic TC tracks, the Magdalen Islands provide an excellent location to study long-term northward shifts in storm tracks. Additionally, the archipelago is surrounded by 235 km of beaches and cliffs, providing ample sediments for aeolian transport, and peat accumulation is high given the maritime and moist climate of the area (Hétu, Rémillard, Bernatchez, & St-Onge, 2020). Here, we present the analysis of two composite sediment cores extracted from two ombrotrophic peatlands on *Ile du Havre-Aubert*, the southernmost island of the archipelago and the most exposed to southwestern winds. We used a multi-proxy approach based on sedimentological and geochemical analysis to examine the evolution of the peatlands, as well as local climate on the Magdalen Islands during the past 4000 years, and reconstruct storms during the past 1000 years, i.e., the period for which both cores display ombrotrophic conditions. To attribute event layers identified in the peat records to tropical cyclones, we also compared our storm reconstruction with a record of hurricanes and hurricane wind strengths that tracked less than 100 km from the Magdalen Islands from the 19<sup>th</sup>, 20<sup>th</sup> and 21<sup>st</sup> centuries. Our goal was to make a high-resolution paleoclimate reconstruction focusing on storms, but also the broader climate modes influencing the Magdalen Islands, and in doing so, establish the potential of ombrotrophic peatlands for paleostorm studies in eastern North America. Our paleostorm record is the first in North America to be derived from ombrotrophic peat cores, as well as being one of the northernmost storm reconstructions on the continent. Our specific objectives are: 1) to understand the processes controlling aeolian particle influx at our sites; 2) to reconstruct a late Holocene record of paleo-storms in the Magdalen Islands; and 3) to improve our understanding of the long-term northward shift of the hurricane track in the North Atlantic in relation to changes in climate modes, particularly the AMV.

## 4.2 Regional setting

The Magdalen Islands (47°26'54"N, 61°45'08"W) are located near the center of the Gulf of St. Lawrence, between Newfoundland and Canada's mainland (**Figure 4.1A-C**). The archipelago measures 80 km in length and comprises eight major islands, including six that are connected by sand barrier beaches or tombolos (Hétu et al., 2020). The geomorphology of the archipelago is dominated by basaltic hills of volcanic origin. Each hill is located on top of a salt dome that pushed the volcanic rocks to the surface, along with the sandstone platforms around the hills. Masses of mixed rocks form the karstic foothills between the volcanic hills and their encircling sandstone platforms (Hétu et al., 2020). The sandstone platforms are mainly composed of quartz and are the main source of sand for the surrounding beaches of the islands (Adomat & Gischler, 2017). During the Last Glacial Maximum (LGM), the southern islands were covered by the Escuminac icecap covering much of the Gulf of St. Lawrence, whereas the northern parts of the archipelago were glaciated by an ice flow from Newfoundland (Rémillard et al., 2016). The southern islands were deglaciated shortly after the LGM (Rémillard et al., 2016) and deglaciation of the whole archipelago occurred by ~11.5 ka BCE (Dalton et al., 2020). During deglaciation, relative sea-level (RSL) reached at least +24 m compared to current sea-level on the southern islands, submerging most of the archipelago until ~ 9 ka BCE (Rémillard et al., 2016). After this time, isostatic rebound resulted in the emergence of the archipelago such that RSL reached a low-stand of at least -17 m by the early Holocene at 7.8 ka BCE, followed by a gradual and slow RSL transgression and re-submergence of the islands that is still ongoing today (Rémillard et al., 2016). The system of barrier beaches, tombolos and lagoons that connect some of the islands were formed relatively recently, for the most part after 600 BCE (Barnett, Bernatchez, Garneau, & Juneau, 2017; Rémillard et al., 2015). The Magdalen Islands were heavily deforested starting in the 16<sup>th</sup> century and, since the middle of the 20<sup>th</sup> century, forested areas are found almost exclusively on the hillsides. The forest is mostly comprised of coniferous species like balsam fir (*Abies balsamea*), black spruce (*Picea mariana*) and white spruce (*Picea glauca*) (Roy-Bolduc, 2010).

The Magdalen Islands' climate is strongly maritime, with cool summers, mild winters, and steady winds coming from all directions (Hétu et al., 2020). Winds are stronger in the fall and winter, particularly the westerlies and north-westerlies, which reflects the dominance of winter storms compared to tropical cyclones in defining the Magdalen Islands' wind regime (Figure

4.1D). The effect of anthropogenic climate change is particularly strong on the Magdalen Islands: during the last two millennia, sea-level rose between 1.3 and 2 mm/yr, with an acceleration of 4.3 mm/yr during the 20<sup>th</sup> century (Barnett et al., 2017). The pronounced regional effect of anthropogenic climate change has led to a reduction of protective sea-ice around the archipelago during the winter, when precipitation is heavier and winds are stronger, driving an increase in coastal erosion, with some parts of the coast retreating at more than 5 m/yr (Bernatchez, Drejza, & Dugas, 2012) (Figure 4.1D-E).

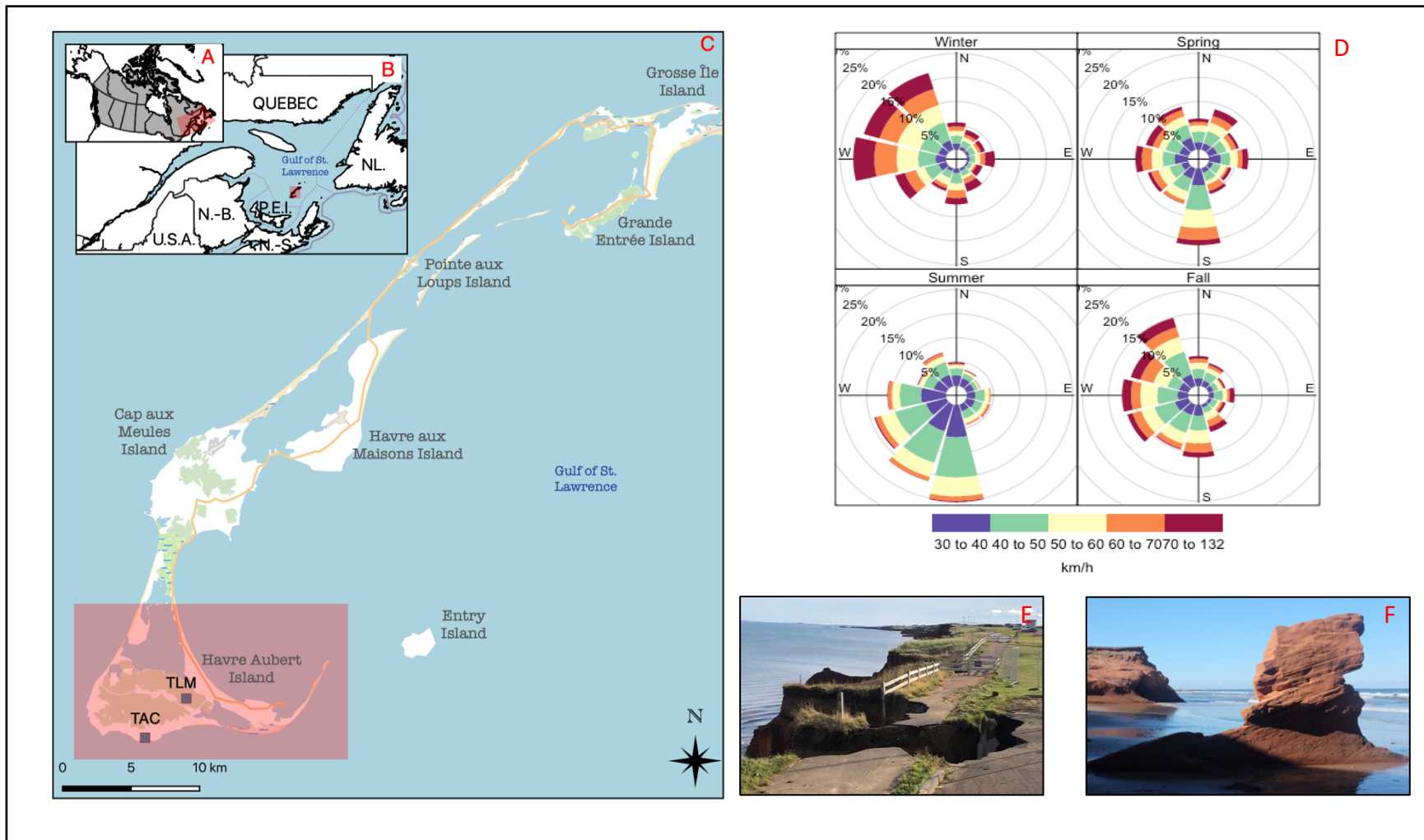


**Figure 4.1** A-C. Location of the Magdalen Islands, Québec, Canada, in the Gulf of St. Lawrence. This study is focused on the southern island, *Ile-du-Havre-Aubert* (red rectangle). The two coring sites are indicated by blue squares. D. Seasonal wind roses displaying 12 directions of incoming winds based on daily peak wind gusts data from 1984 to 2018. The number of days (expressed as %) for any category of speed of peak wind gusts (in km/h) are indicated for each wind direction. Winds are stronger during the fall and winter and mostly coming from the southwest, west and northwest. E-F. Erosional features on the coast of the Magdalen Islands.

## 4.3 Methods

### 4.3.1 Site description and field methods

In August 2020, peat sequences were extracted from two ombrotrophic bogs located on *Ile-du-Havre-Aubert* (IHA), the southernmost island of the archipelago (Figure 4.2A). *Tourbière-de-l'Anse-à-la-Cabane* (TAC) (47°12'54.0"N, 61°57'48.4"W, ~10 m ASL) has an area of 9.0 ha and is located ~210 meters from the nearest coast, which consists of south-facing red sandstone cliffs (Ministère de l'Environnement et de la Lutte contre les changements climatiques, 2021a) (Figure 4.2B). *Tourbière-du-Lac-Maucôque* (TLM) (47°14'30.9"N, 61°55'24.7"W, ~4 m ASL) has an area of 40.2 ha and is located ~2 km from coastal beaches on the south and northeast parts of IHA (Ministère de l'Environnement et de la Lutte contre les changements climatiques, 2021b) (Figure 4.2C). Both sites are designated protected areas by *le Gouvernement du Québec* to protect the endangered population of northern dwarf huckleberry (*Gaylussacia bigeloviana* [Fernald] Sorrie & Weakley), a small coastal shrub growing in acidic bogs, which is found at both locations. The dominant vegetation in the peatlands is *Sphagnum* spp. moss (Lindb.) and shrubs from the *Ericaceae* family, with black spruce (*Picea mariana* [Mill.] Britton, Sterns & Poggenburg) growing around the perimeter. These two sites are similar in terms of ecological composition, but they are likely to be affected by different aeolian and hydrological processes because of their different surroundings. In selecting the sampling locations, we chose open areas away from shrubs and trees and cored near the center of each peatland, which tends to preserve the deepest and oldest peat sequences. We also avoided the walking trails and snowmobile tracks that were visible at TLM (Figure 4.2D-E).

We used a Russian peat corer to extract core segments 50 cm long and 5 cm wide (Figure 4.2F-G) until we were not able to manually push the corer through the sediments, having reached the bottom of the organic layer. At both sites, it was not possible to extract core segments at depths between 0 and ~50 cm, since the surface peat moss was not dense enough, and so we used shovels to extract near-surface monoliths instead. Multiple core drives were extracted at each site at 1 m or less from each other (see Table S2 and Figure S1 for a list of core sections and coring site schematic). In the field, the cores were transferred to PVC split tubes and wrapped in cellophane, and the monoliths were wrapped in cellophane, before being transported to Bishop's University, Sherbrooke, Québec, for storage at 4° Celsius. The top monoliths suffered compaction during

transportation and storage and therefore a multiplicative factor of 1.61 and 1.79 was applied to these for TAC and TLM, respectively.

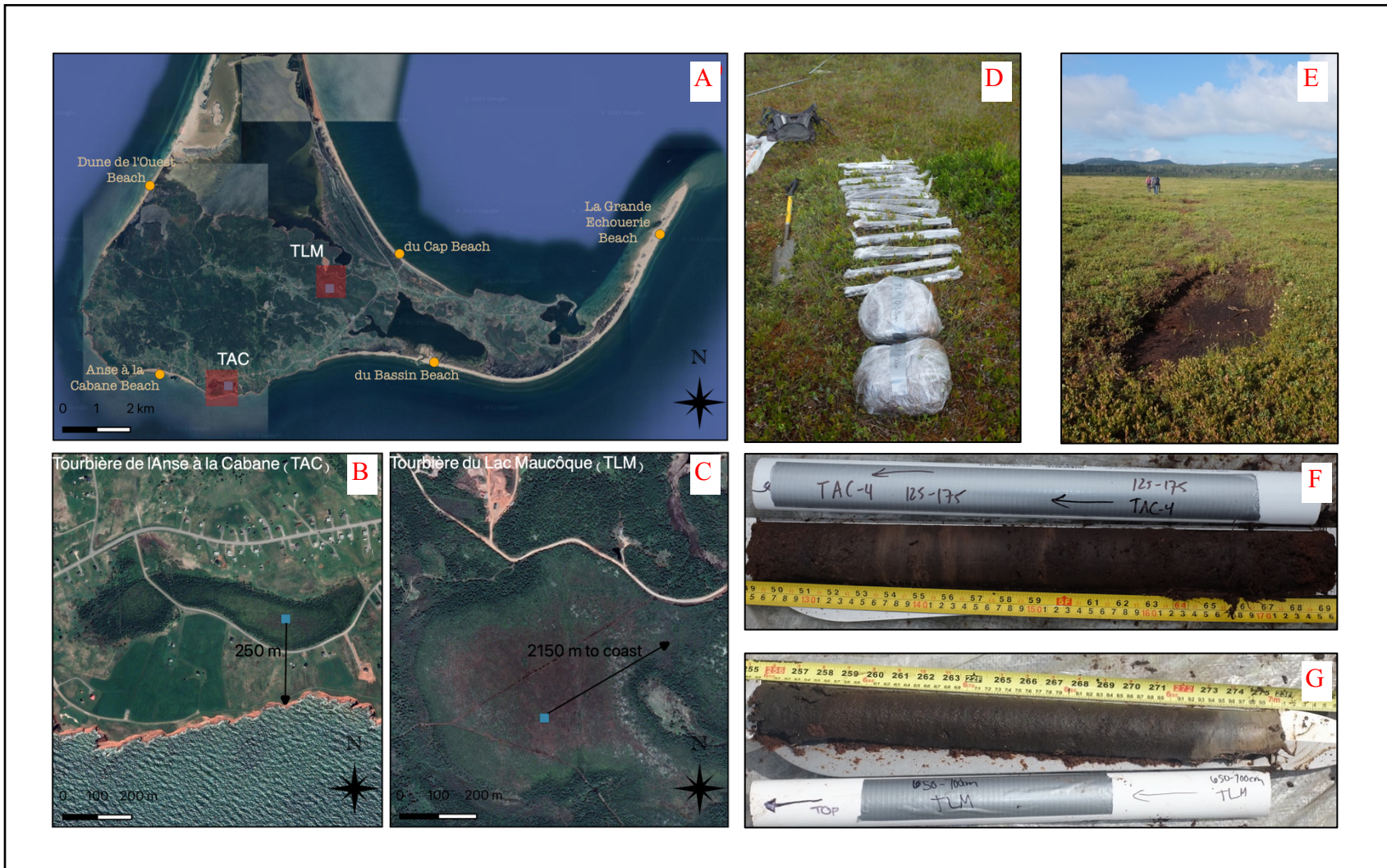


**Figure 4.2** A) Map of *Ile-du-Havre-Aubert*, the southernmost island of the archipelago. The two coring sites, TAC and TLM, are indicated by a blue square overlain by a red square, delimiting the insets B and C. The main beaches surrounding the island are indicated by yellow dots. B-C) TAC and TLM coring sites. The locations where the cores were extracted are indicated by blue squares. The TAC core site is 250 m away from the south facing cliffs, while the TLM core site is 2150 m away from the closest beach, which is du Cap beach. D) Photos of the coring site at TLM. The cores were extracted in 50 cm sections and then wrapped in PVC split-tubes. E) Visible tracks from the snowmobile trail cutting through TLM. F-G) Photos of core sections after they were extracted from the peatland and before transferring them into PVC split-tubes. Panel F shows a section from 125-175 cm from TAC, containing visible sand layers. Panel G shows a section from 600-700 cm from TLM, containing a layer of coarse sand defining the lower limit of the peat column.

#### 4.3.2 Chronology and Peat Accumulation Rates

Twenty-five radiocarbon ( $^{14}\text{C}$ ) dates (16 for TAC and 9 for TLM) were obtained from the A.E. Lalonde AMS Laboratory at the University of Ottawa, on plant macrofossils (which included mostly woody fragments) and bulk sediments (Table 4.1). Plant macrofossils were preferentially selected for dating when available in the core, and bulk peat samples were only selected when no macrofossils were available, usually in highly decomposed peat sections. We chose wood fragments from branches, trunk, or stems, and avoided roots and rootlets, so as to not date material that would be younger than its surrounding matrix. Wood samples were pretreated with an acid-alkali-acid (AAA) treatment, whereas bulk sediments were pretreated only with an acid wash (for a detailed explanation of pre-treatment and processing methods, see Crann et al. (2017)).

$^{210}\text{Pb}$  activity was measured on bulk sediments from the 50-cm long monolith of TAC and TLM to establish age-depth models for the most recent 150 years. Samples taken every 2 cm were spiked with the chemical tracer  $^{209}\text{Po}$ , then subjected to an acid digestion, and mounted onto sliver plates, as described by De Vleeschouwer, Sikorski, and Fagel (2010).  $^{210}\text{Pb}$  activity was indirectly determined through measurement of  $^{210}\text{Po}$  (a daughter product of  $^{210}\text{Pb}$  decay) using an EGG-Ortec Type 576ATM alpha spectrometer at the GEOTOP Laboratory at the Université du Québec à Montréal (UQAM).

The age-depth model for TAC was constructed by combining the  $^{210}\text{Pb}$  and  $^{14}\text{C}$  dates using the PLUM package in R (M Blaauw, Christen, & Aquino-Lopez, 2021). The age-depth model for TLM was constructed from the  $^{14}\text{C}$  dates using the BACON package in R software (see Results) (M Blaauw et al., 2022). Both models used the IntCal20 calibration curve for the  $^{14}\text{C}$  dates (Reimer et al., 2020) and are based on Bayesian methods (Aquino-López, Blaauw, Christen, & Sanderson, 2018; Maarten Blaauw & Christen, 2011). The date for the surface of the core was set to 2019 CE, the year the cores were extracted. The dates are given in Common Era/Before Common Era (CE/BCE) throughout the text. The Peat Accumulation Rate (PAR) was calculated by dividing each centimeter of peat accumulation by the number of years spanned by that centimeter of peat and is given in cm/yr.

#### 4.3.3 Peat type analysis

The identification of peat type was performed on the TAC and TLM cores based on the Troels-Smith method (Birks & Birks, 1980; Troels-Smith, 1955) to describe textural variations, variations

in peat composition, and variations in the degree of humification (degree of decomposition of organic matter) in each core. Peat samples of 1 cm<sup>3</sup> were extracted every 4 or 8 cm from the TAC and TLM cores, respectively. The sample resolution was increased to 1 or 2 cm when peat type boundaries were identified. Each sample was diluted in deionized water and examined under a stereoscopic microscope (4x-40x magnification) to determine the relative abundance of each peat type. We focused on four main peat types: bryophytic peat (dominated by *Sphagnum* spp. moss remains), herbaceous peat (dominated by sedge remains), ligneous peat (dominated by twigs and bark fragments), and humous peat (highly degraded peat in which specific components can no longer be distinguished). Mineral-rich layers were also noted. The relative abundance of each peat type was defined using the following categories: important (peat type represents >75% of total peat sample), high (50-75%), medium (25-50%), low (12.5-25%), and trace (0-12.5%). For each sample, the degree of decomposition was noted and categorized as preserved (plant remains are easily recognizable with no or very few signs of decomposition), degraded (some plant remains are recognizable, mixed with decomposed matter), and highly degraded (few plant remains are recognizable). The presence of some macrofossils (seeds, leaves, needles) were identified using the Continental Paleocology Laboratory reference collection at the GEOTOP Laboratory at UQAM (Garneau, 1995).

#### 4.3.4 Computerized tomography and x-ray radiography

Selected cores from TLM (depth 100-700 cm) and TAC (depth 75-325 cm) were analysed at the CT-Scan Lab at the *Institut National de la Recherche Scientifique* (INRS) in Québec City, using computerized tomography (CT) scanning which uses x-rays to produce a 3-D representation of the cores. This allows the examination of variations in sediment type and density in the cores without destructive sampling. The x-ray radiographs are based on the attenuation coefficient, which is a measure of the absorption of the x-ray beam by the material (Emmanouilidis et al., 2020). The attenuation coefficient is expressed in Hounsfield units (HU), with the value of 0 representing water and -1000 representing air (Emmanouilidis et al., 2020). These values are then expressed as a grayscale to create images of the scans. As density is one of the main factors affecting X-ray attenuation, it is possible to use the HU profile as a proxy for this parameter. This is particularly useful to quickly identify areas of interest within the core, such as segments with a succession of dense/less dense sedimentary layers that are not visible to the naked eye.

#### 4.3.5 $\mu$ -XRF analysis

XRF-Core-Scanning (XRF-CS) is a non-destructive and rapid method that uses micro-x-ray fluorescence ( $\mu$ -XRF) to quantify the elemental composition of sediment cores (Croudace & Rothwell, 2015). Typically applied to marine and lacustrine sediments (Longman, Veres, & Wennrich, 2019), its use has recently been expanded to peat cores (Chawchai, Kylander, Chabangborn, Löwemark, & Wohlfarth, 2016; Kern et al., 2019; Orme, Reinhardt, Jones, Charman, Croudace, et al., 2016). An ITRAX Core Scanner (ITRAX-CS) from the *Laboratoire de géochimie, imagerie et radiographie des sédiments (GIRAS)* at the INRS was used to measure the inorganic geochemical composition of the peat sequences. Measurements were made at 1-mm increments for TAC and 2-mm increments for TLM with a chromium (Cr) tube set to 40 kV, 10 mA and an acquisition time of 20 s. After experimenting with a Cr tube and a Molybdenum (Mo) tube on two 50-cm sections from TAC and TLM, these settings were found to be the most efficient in capturing variation in lighter elements such as chlorine (Cl). The XRF-CS results are given in thousands counts per second (kCPS).

Despite some studies that advise that the XRF-CS results be divided by the sum of coherent and incoherent peaks (Goslin et al., 2019; Orme et al., 2015), which represents the Compton and Rayleigh scattering and is considered a proxy for downcore variation in organic matter, this transformation was not applied, since it was shown to be of limited use when looking at small variations in organic/mineral content (Chawchai et al., 2016). Our analysis focused on elements associated with terrigenous mineral inputs (potassium [K], titanium [Ti], silicon [Si], zirconium [Zr] and iron [Fe]); on elements abundant in ocean water (bromine [Br], chlorine [Cl] and sulfur [S]), and other elements such as manganese (Mn) and calcium (Ca) that were present in the core and that may indicate other sedimentary delivery processes such as provenance and water table depth.

#### 4.3.6 Mineral and organic content

Mineral and organic content in each core were determined by the loss-on-ignition (LOI) procedure of Heiri, Lotter, and Lemcke (2001). Five cm<sup>3</sup> of wet sediment was extracted every cm for TAC and every other cm for TLM. Each sample was dried overnight at 105 °C to determine the dry

weight  $DW_{105}$ . The dried organic matter was then burnt at 550 °C, giving weight  $DW_{550}$ . The organic content and mineral content were calculated as:

$$\text{Organic (\%)} = (DW_{105} - DW_{550}/DW_{105}) * 100$$

$$\text{Minerals (\%)} = (DW_{550}/DW_{105}) * 100$$

Dry bulk density (DBD) and ash bulk density (ABD) were calculated by dividing the  $DW_{105}$  and the  $DW_{550}$  by the volume of wet sediment (5 cm<sup>3</sup>), respectively, and are given in g/cm<sup>3</sup>. Ash-free bulk density (AFBD; bulk density of the organic content without the mineral content) was calculated by dividing the  $DW_{105}$  minus the  $DW_{550}$  by 5 cm<sup>3</sup>. Finally, carbon accumulation rate (CAR) (g C/m<sup>2</sup>·yr) was calculated by multiplying the AFBD (in g/cm<sup>3</sup>) by the PAR (in cm/yr), a multiplying the result by a factor of 10,000.

#### 4.3.7 Aeolian Sand Influx

After completing the LOI procedure, the residue from each sample was then treated for one hour with a solution of 10% hydrochloric acid (HCl) and 10% potassium hydroxide (KOH) to eliminate any remaining carbonate matter and to deflocculate the sediments, as in Vaasma (2008). The samples were then washed with deionized water and sieved using a 125 µm sieve for TAC and a 63 µm sieve for TLM to establish the aeolian sand profiles along the cores. Finally, the sieved aeolian sand samples (> 125 µm for TAC and > 63 µm for TLM) were dried overnight at 105 °C and weighed. These size boundaries correspond to the fine/very fine sand (< 125 µm) and sand-silt (< 63 µm) fractions (Wentworth, 1922). A smaller sieve was used for TLM due to the much lower proportion of mineral matter in that core compared to TAC; since TLM is located further away from the coast, mineral particles need to be transported for a longer distance to reach this peatland. The relationships among grain size, wind stress and transport competence determine the magnitude of winds able to transport in suspension the grains of the different size classes. For example, Goslin et al. (2019) calculated an ASI based on the assumption that sand particles > 125-µm require winds > 78 km/h to be transported in suspension. To calculate the ASI, the aeolian sand weight was multiplied by the PAR. Results are reported in g/m<sup>2</sup>·yr for each grain class, as described by Björckl and Clemmensen (2004).

#### 4.3.8 Multivariate analysis

*Cluster analysis* – Stratigraphically constrained cluster analysis (CONISS) was performed on the geochemical variables, mineral content and ASI to establish zonation of the cores. The geochemical variables were first downsampled by averaging to a 1-cm resolution to match the resolution of the mineral and ASI data. CONISS was then done using the Rioja package in R (Juggins, 2022). The maximum plausible number of zones (the number of zones whose dispersion is larger than what would be expected from a cluster analysis of a random shuffle of the data) for each dataset was extracted and compared with visual observations of the core and data from the peat type analysis to establish the zonation.

*Principal component analysis* – Principal component analysis (PCA) was applied to the 10 geochemical elements listed above (see Section 3.5  $\mu$ -XRF analysis) to explore trends and similarities within TAC and TLM. The PCA was calculated for the entire composite core sequences, excluding the basal sand layers that are not part of the organic portions of the cores. First, to confirm the appropriateness of the PCA, we applied a Detrended Correspondence Analysis (DCA) to measure the heterogeneity of the datasets, i.e. to determine that the lengths of the first DCA axis are smaller than 3 standard deviations, and hence that the datasets are homogenous and suitable for linear (i.e. PCA) methods (Leps & Smilauer, 2003). The PCA was done using the factoMineR package in R (Husson, Julie, Le, & Mazet, 2016). Beforehand, a z-score transformation was applied to the variables and the PCA was done using the correlation matrix. Additionally, the LOI-derived variables (Minerals %, DBD, CAR and ASI) were included as supplementary/passive variables in the PCA to examine their relationship with the geochemical variables without assuming any statistical relationships. Since the LOI data do not have the same resolution as the geochemical data (1-2 cm versus 1-2 mm), a simple linear interpolation was applied to fill-in the gaps in the latter dataset.

We tested the significance of the PCA-generated eigenvalues with the R package PCAtest (Camargo, 2022). The PACtest algorithm applies a permutation-based test by shuffling the observations in each variable to create a null distribution with which to compare the empirical distribution and test whether the variables used in the PCA are correlated. The random sample was created with 1000 bootstrap replicates to which 1000 random permutation were applied.

#### *4.3.9 Determining storm frequency*

To determine storm frequency, we followed the approach by Donnelly et al. (2015), itself based on the approach by Lane, Donnelly, Woodruff, and Hawkes (2011). Storm detection is based on two proxies, Ti CPS and ASI. Storm detection is based primarily on identifying Ti peaks in the records, while ASI is used as further confirmation that the Ti peaks are associated with the mineral content of the core. Furthermore, the storm record was calibrated using the NOAA Best Track record (IBTrACTS) (Knapp et al., 2010) as well as a record of daily wind speed on the Magdalen Islands (Environment and Climate Change Canada, 2020). Titanium (Ti) was chosen as a storm proxy after a careful analysis of geochemical and sedimentological data (see Results and discussion).

*Calibration data* – Before determining storm frequency from the peat core records, we first needed an estimate of storm frequency from instrumental data from the Magdalen Islands. To do this, we used the IBTrACTS dataset (Knapp et al., 2010) to calculate the number of hurricanes or tropical storms that passed within a distance of less than 100 km from the Magdalen Islands in 2019-1851 CE. The IBTrACTS is a collection of up-to-date and homogenized hurricane best track data from meteorological agencies worldwide, endorsed by the World Meteorological Organization (WMO) as an official resource for best track data (Knapp et al., 2010). To verify whether a hurricane had an impact or not on the Magdalen Islands, we investigated impacts reported in local newspapers as well as in a compilation of shipwrecks, which are well documented on the Magdalen Islands for the past 200 years and often include the cause of the wreck (Landry, 1989, 1994). Additionally, we also compared our data with a record of daily winds exceeding 116 km/h (the threshold for hurricane-strength winds) over the period 2019-1985 CE, i.e., the period for which we have reliable daily wind data from the Magdalen Islands, to see whether storms other than hurricanes have impacts on the Magdalen Islands. Wind data was obtained from the Historical Weather dataset available through the Canadian Centre for Climate Services (Environment and Climate Change Canada, 2020). The hurricane-strength wind record was calculated using the daily wind data from July to December, excluding the data from January to June. This is because during the winter months, the Magdalen Islands are usually covered with snow and ice, and therefore we do not expect that a lot of sediment is being transported from beaches and cliffs into the peatlands

during those months. We therefore assume that if there is a storm signal in our core, it will most likely be from a summer/fall event.

*Storm detection and frequency* – First, to remove low-frequency variability from the Ti record, we subtracted a 30-year running average from the data (Lane et al., 2011). This isolated the Ti peaks associated with short-lived events from the background Ti variations associated with longer-term environmental changes. The Ti values exceeding 99% of the Ti cumulative distribution were excluded from the running average calculation to make it more robust to extreme values (Donnelly et al., 2015), and thus to prevent adjacent large peaks from being excluded from our event records. We then defined the threshold of what constitutes a storm event as the 95<sup>th</sup> percentile of the detrended Ti data over the period 2019-1851, i.e., the historical period for which the IBTrACTS record is available, for which the number of events identified in the Ti records is similar to the number of events identified in the instrumental records that had a known impact on the Magdalen Islands. To generate the storm frequency records, we compiled the sum of the storms identified in the Ti records at TAC and TLM using a sliding window of 168 years to facilitate comparisons with the instrumental period (the period 2019-1851 CE used to calibrate the storm record) (Lane et al., 2011). The storm frequency records were normalized to 100 years. Finally, it is important to note that the calibration of the storm record was done using only the TAC record over the period 2019-1851, because TAC was the only core for which we had a reliable age-depth model during that period based on <sup>210</sup>Pb (see Results and discussion).

## 4.4 Results and discussion

### 4.4.1 Overview

The TAC peat core measures 325 cm in length and is an assemblage of three different core drives: the surface monolith (0-50 cm), the main organic section (50-275 cm), and the bottom section (275-325 cm). There is a basal sand unit located between 317-325 cm that defines the lower limit of peat deposition and therefore our subsequent analysis of TAC. The TLM peat core measures 700 cm in length and is also an assemblage of three different core drives: a section of the surface monolith (0-25 cm), a section of the second core taken at the TLM site (25-100 cm), and the main core (100-700 cm). Its basal sand unit is located between 693-700 cm and defines the onset of peat deposition and therefore of our analysis of TLM. These assemblages cover the full peat sequences at both sites (photos in Figure S3).

### 4.4.2 Age-depth models and PAR

*Tourbière-de-l'Anse-à-la-Cabane (TAC)* – The age-depth model of TAC is based on 16  $^{14}\text{C}$  dates distributed throughout the whole length of the peat core and 15  $^{210}\text{Pb}$  dates from the top 50 cm of the core (Table 4.1, Figure 4.3). The oldest mean modelled date comes from a wood fragment located between 319-320 cm that was dated as 2970 BCE (Table 4.1). Between 2215-2970 BCE, the BACON-derived age-depth model is relatively constant and shows a slow PAR of 0.03 cm/yr, followed by an acceleration to 0.13 cm/yr between 1110-2215 BCE (Figure 4.3). Another period of very low PAR of 0.04 cm/yr was recorded from 1110 BCE and 1015 CE between 133-162 cm that could indicate either a hiatus during that period, a steep reduction in peat accumulation rate, or a mix of the two. At 147-148 cm, a small wood fragment was dated to 495 BCE, but should be treated with caution; the age of this wood fragment may not correspond to the age of its surrounding matrix, as this layer could have been subject to mixing and reworking of the sediments related to an event associated with the hiatus. The rate of peat accumulation is then stable from 1920-1015 CE, at 0.13 cm/yr, and then accelerates markedly in the period from 2019-1920 CE to 0.39 cm/yr, which roughly corresponds to the portion of the core that was dated with  $^{210}\text{Pb}$  and the less decomposed acrotelm layer.

*Tourbière-du-Lac-Maucôque (TLM)* – The age-depth model of TLM is based on nine  $^{14}\text{C}$  dates distributed throughout the length of the peat core (Table 4.1, Figure 4.3).  $^{210}\text{Pb}$  dating was attempted but was not successful on the TLM core, because  $^{210}\text{Pb}$  measurements had not reached the supported  $^{210}\text{Pb}$  background level in our deepest sample near 50 cm. Additionally, the two bottom wood samples, at 669 cm and 674 cm, had calibrated  $^{14}\text{C}$  dates of 7030-6655 BCE and 6581-6433 BCE respectively, but were omitted from the BACON-derived age-depth model due to their age inversion and outlier nature. The oldest modelled date comes from a wood fragment located between 634-635 cm which dated to 2310 BCE (Table 4.1). Between 1455 CE and 2310 BCE, the slope of the age-depth model is constant and shows a PAR of 0.14 cm/yr, followed by a slight acceleration in PAR to 0.22 cm/yr in the period from 2019-1455 CE. The age-depth model between 0-100 cm should be treated and analysed carefully: it is probably flatter towards the top due to the rapid peat accumulation rate in the acrotelm layer, but without surface  $^{210}\text{Pb}$  measurements, the current model does not reflect this.

**Table 4.1** Accelerator mass spectrometry radiocarbon ( $^{14}\text{C}$ ) results for both sites in the Magdalen Islands. Dated material is from bulk peat sediment (bulk) or wood fragments (wood). Uncalibrated  $^{14}\text{C}$  dates are shown as years before 1950 (BP). The  $^{14}\text{C}$  dates were input into the Bayesian (BACON) algorithm in R and calibrated with the IntCal20 calibration curve. Calibrated dates are presented as calibrated years before 1950 (cal. BP) and as Common Era/Before Common Era (CE/BCE).

| Sample depth (cm) | Lab ID    | Material | AMS $^{14}\text{C}$ date BP (uncal.) | Calibrated 2 sigma range |                 | Mean modelled age (BCE/CE) |
|-------------------|-----------|----------|--------------------------------------|--------------------------|-----------------|----------------------------|
|                   |           |          |                                      | Cal. BP                  | BCE/CE          |                            |
| <i>TAC</i>        |           |          |                                      |                          |                 |                            |
| 31-32             | UOC-18435 | Bulk     | 6 ± 21                               | 249 – 41                 | 1701 – 1909 CE  | 1921 CE                    |
| 57-58             | UOC-15803 | Wood     | 162 ± 26                             | 287 – 43                 | 1664 – 1908 CE  | 1718 CE                    |
| 76-77             | UOC-18286 | Wood     | 341 ± 13                             | 469 – 316                | 1482 – 1635 CE  | 1565 CE                    |
| 102-103           | UCO-18436 | Bulk     | 613 ± 20                             | 649 – 551                | 1301 – 1400 CE  | 1347 CE                    |
| 122-123           | UOC-15804 | Wood     | 869 ± 26                             | 900 – 693                | 1050 – 1257 CE  | 1177 CE                    |
| 128-129           | UOC-18287 | Wood     | 964 ± 14                             | 921 – 797                | 1030 – 1154 CE  | 1117 CE                    |
| 133-134           | UCO-18437 | Bulk     | 992 ± 21                             | 957 – 798                | 994 – 1153 CE   | 1016 CE                    |
| 147-148           | UOC-15805 | Wood     | 2469 ± 27                            | 2712 – 2371              | 763 – 422 BCE   | 495 BCE                    |
| 162-163           | UOC-18288 | Wood     | 2928 ± 14                            | 3159 – 3001              | 1210 – 1052 BCE | 1111 BCE                   |
| 185-186           | UOC-18438 | Bulk     | 3052 ± 21                            | 3350 – 3178              | 1401 – 1229 BCE | 1324 BCE                   |
| 199-200           | UOC-15806 | Wood     | 3178 ± 27                            | 3452 – 3361              | 1503 – 1412 BCE | 1438 BCE                   |
| 226-227           | UOC-15807 | Wood     | 3300 ± 28                            | 3571 – 3455              | 1622 – 1506 BCE | 1584 BCE                   |
| 258-259           | UOC-15808 | Wood     | 3508 ± 29                            | 3870 – 3694              | 1921 – 1745 BCE | 1816 BCE                   |
| 283-284           | UOC-15809 | Wood     | 3597 ± 28                            | 3980 – 3834              | 2031 – 1885 BCE | 2007 BCE                   |
| 296-297           | UOC-15810 | Wood     | 3771 ± 30                            | 4240 – 3996              | 2291 – 2047 BCE | 2214 BCE                   |

|            |           |      |           |             |                 |          |
|------------|-----------|------|-----------|-------------|-----------------|----------|
| 319-320    | UOC-18289 | wood | 4376 ± 17 | 5025 – 4865 | 3076 – 2916 BCE | 2973 BCE |
| <i>TLM</i> |           |      |           |             |                 |          |
| 59-60      | UOC-18434 | Bulk | 174 ± 21  | 289 – 73    | 1661 – 1916 CE  | 1751 CE  |
| 122-123    | UOC-14324 | Wood | 417 ± 36  | 526 – 327   | 1425 – 1624 CE  | 1455 CE  |
| 243-244    | UOC-15799 | Wood | 1582 ± 35 | 1532 – 1390 | 418 – 561 CE    | 488 CE   |
| 390-391    | UOC-15800 | Wood | 2491 ± 26 | 2723 – 2469 | 774 – 520 BCE   | 625 BCE  |
| 484-485    | UOC-15801 | Wood | 3014 ± 28 | 3335 – 3078 | 1386 – 1129 BCE | 1265 BCE |
| 577-578    | UOC-14325 | Wood | 3572 ± 37 | 3978 – 3724 | 2029 – 1775 BCE | 1919 BCE |
| 634-635    | UOC-15802 | Wood | 3813 ± 26 | 4346 – 4093 | 2397 – 2144 BCE | 2308 BCE |
| 669-670*   | UOC-18285 | Wood | 7923 ± 19 | 8979 – 8604 | 7030 – 6655 BCE | 2716 BCE |
| 674-675*   | UOC-14326 | Wood | 7650 ± 32 | 8536 – 8382 | 6581 – 6433 BCE | 2768 BCE |

\* The AMS <sup>14</sup>C dates at these depths present an age inversion and were considered outliers by the BACON R software. Therefore, the modelled median date associated with these depths does not reflect the AMS <sup>14</sup>C date.

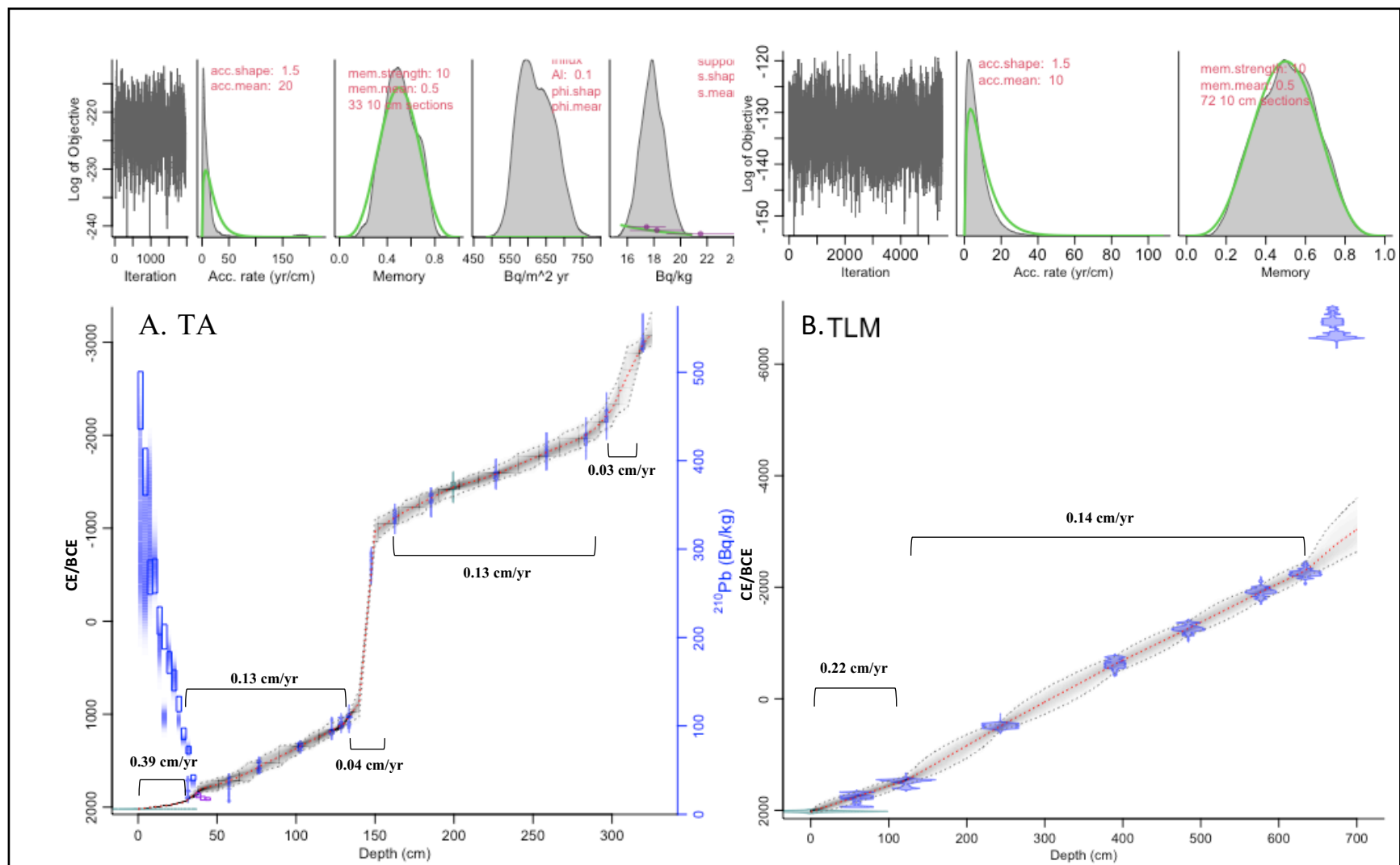


**Figure 4.3.** BACON-derived age-depth models for TAC (A) and TLM (B). Radiocarbon ( $^{14}\text{C}$ ) dates are shown in blue along the age model and  $^{210}\text{Pb}$  dates from the top 50 cm of the TAC core only are shown in purple. The surface date (2019 CE) is indicated in teal. In the TAC core, the rate of supported  $^{210}\text{Pb}$  (right axis) is indicated by the blue boxes on the left-hand side (the blue boxes are the measured  $^{210}\text{Pb}$  values; blue shadings represent the modelled  $^{210}\text{Pb}$  values). For each core, the leftmost upper panel depicts the Markov Chain Monte Carlo (MCMC) iterations; then the prior (green curve) and posterior (grey histogram) distributions the accumulation rate (second panel), and next the memory (third panel). For TAC, the fourth panel indicates  $^{210}\text{Pb}$  influx in  $\text{Bq/m}^2\text{-yr}$  and the fifth panel indicates supported  $^{210}\text{Pb}$  in  $\text{Bq/kg}$ . The peat accumulation rates (PARs) are indicated for certain sections of the cores in  $\text{cm/yr}$ .

#### 4.4.3 Core description: sedimentology of TAC and TLM

The dry bulk density (DBD), carbon accumulation rate (CAR), mineral content and aeolian sand influx (ASI) data are presented for each core, alongside a peat type description (Figures 4.4 and 4.5). Some macrofossil data is also presented, when relevant, to help illustrate each peatland's developmental stages and evolution. A total of 4 distinct units (with 6 subunits) are defined for TAC, and 4 distinct units (with 5 subunits) are defined for TLM.

##### *Tourbière-de-l'Anse-à-la-Cabane (TAC)*

The TAC peat core lies above a basal sand layer located between 317-325 cm, which has a mineral content of 70%. Above this sand layer, the peat core is organic-rich with 88% of its total dry weight consisting of organic matter, and 12% consisting of mineral matter (Figure 4.4; see Figure S3 for the full core with the basal sand layer). The TAC core shows textural variations at different depths, with important variations in peat composition, degree of humification, density, and mineral content (Figure 4.4). The main peat units are herbaceous peat, bryophytic peat, ligneous peat, and detritus peat. Mean DBD is 0.09 g/cm<sup>3</sup> and varies between 0.05 g/cm<sup>3</sup> and 0.20 g/cm<sup>3</sup>, while mean CAR is 90 g/m<sup>2</sup>·yr and varies between 4.9 g/m<sup>2</sup>·yr and 336.1 g/m<sup>2</sup>·yr. The mineral content and the ASI values vary together and generally decrease with depth, but with important local variations, especially above 155 cm. The core is not homogenous and visible sand layers cut through the matrix, especially between 135-155 cm. These sand layers are visible in the x-ray images as light horizontal lines within the darker peat matrix (Figure 4.4) and usually correspond to peaks in the mineral content and ASI records. The total mean ASI is 1.47 g/m<sup>2</sup>·yr, and it varies between 0 g/m<sup>2</sup>·yr and 29.3 g/m<sup>2</sup>·yr.

*Unit 1 (274-316 cm, 1925-2870 BCE)* – Unit 1 is composed of herbaceous-dominated peat. *Carex* seeds and pteridophyte rootlets were identified in this section, suggesting that the peatland started forming as a fen environment (Magnan, Garneau, & Payette, 2014; Warner & Asada, 2006). This unit is relatively dense with a DBD of 0.10 g/cm<sup>3</sup>, despite a mineral content of 6%, and the mean CAR is low at 53.6 g/m<sup>2</sup>·yr, indicating a faster peat decay in this portion of the core. There is one visible sand-enriched layer at 305-309 cm (2500-2610 BCE) which has a peak mineral content of 28% and that separates subunit 1a from subunit 1b, with a corresponding low ASI value of 0.63 g/m<sup>2</sup>·yr. There is a reduction in DBD and an increase in CAR from subunit 1a (306-316 cm, 2515-

2870 BCE) to subunit 1b (274-305 cm, 1925-2480 BCE), indicating a reduction in decay rates throughout unit 1. Subunit 1a is composed of highly degraded and laminated herbaceous peat and has a mean DBD and CAR of 0.14 g/cm<sup>3</sup> and 34.2 g/m<sup>2</sup>·yr, respectively, whereas subunit 1b is composed of visible herbaceous remains and incorporates small to large (up to 5 cm long) twigs and bark fragments in its matrix and has a mean DBD and CAR of 0.09 g/cm<sup>3</sup> and 60.3 g/m<sup>2</sup>·yr, respectively. The first recognizable remains of *Sphagnum* moss start appearing gradually at 290 cm (2085 BCE).

*Unit 2 (156-273 cm, 1035-1920 BCE)* – Unit 2 is composed of different layers of well-preserved, degraded, or highly degraded bryophytic peat. The mean DBD is below the core average at 0.07 g/cm<sup>3</sup>, while the mean CAR is above the core average at 94.1 g/m<sup>2</sup>·yr. This unit corresponds to a period of rapid peat accumulation. Unit 2 has the lowest mineral content and ASI of all the units, with a mean mineral content of 3.3% and an average ASI of 0.1 g/m<sup>2</sup>·yr. Some parts of unit 2 are completely devoid of aeolian sand, especially at depths between 180-200 cm (1275-1440 BCE). There are two peaks in mineral content at 177 cm (1250 BCE) and 167 cm (1160 BCE), where mineral content reaches 8.2% and 9.3%, respectively. These peaks are also visible in the aeolian sand record as slightly larger influxes of 0.36 g/m<sup>2</sup>·yr and 0.25 g/m<sup>2</sup>·yr. The transition between unit 2 and unit 3 starts at 162 cm (1005 BCE), where highly degraded bryophytic peat is gradually replaced by detritus peat.

*Unit 3 (135-155 cm, 970 CE-1020 BCE)* – Unit 3 is composed of detritus peat with few identifiable organic remains. The large timespan of approximately 2000 years of sediment accumulation within 20 cm indicates a drastic reduction in peat accumulation and/or an increase in peat decomposition, compaction, or erosion, and may be an indication of a hiatus in the core. Unit 3 is characterized by an above average DBD of 0.13 g/cm<sup>3</sup> and very low CAR of 29.8 g/m<sup>2</sup>·yr. It is the unit with the highest mineral content with a mean of 23.8%, while the mean ASI is below average at 0.87 g/m<sup>2</sup>·yr. There are two visible main sand-enriched layers located at 151 cm (960 BCE) and 136 cm (955 CE) that have mineral contents of 32% and 55%, respectively. These peaks are also visible in the aeolian sand record as larger influxes of 2.19 g/m<sup>2</sup>·yr and 3.28 g/m<sup>2</sup>·yr. The chronology of the deposition of these sand layers is uncertain as there was not suitable organic material for AMS radiocarbon dating within the sand layers, or directly above or below the layers. The transition

between unit 3 and unit 4 starts at 135 cm (980 CE) in a layer of ligneous peat that is gradually replaced by bryophytic peat.

*Unit 4 (0-134 cm, 2019-995 CE)* – Unit 4 is composed of bryophytic and ligneous peat and is characterized by an average DBD of 0.09 g/cm<sup>3</sup> and a mean CAR of 111 g/m<sup>2</sup>·yr. Unit 4 is also high in minerals, with a mean mineral content of 20.8% and a mean ASI of 3.45 g/m<sup>2</sup>·yr. There is an increase in DBD, CAR, mineral content and ASI from subunit 4a (50-134 cm, 1755-995 CE) to subunit 4b (0-49 cm, 2019-1760 CE). Subunit 4a is composed of different layers of well-preserved or degraded bryophytic or ligneous peat. In subunit 4a, there is a 18.9% peak in mineral content (ASI: 1.39 g/m<sup>2</sup>·yr) at 125 cm (1150 CE), as well as two areas of increased mineral content between 96-102 cm (1405-1350 CE; peak mineral content of 30 % and ASI of 3.47 g/m<sup>2</sup>·yr) and 65-82 cm (1660-1520 CE; peak mineral content of 38 % and ASI of 9.61 g/m<sup>2</sup>·yr). Subunit 4b, which corresponds roughly to the industrial period, is composed entirely of well-preserved bryophytic peat, probably because it corresponds with the acrotelm layer (the surface peat layer containing living peat (Ingram, 1978)). There are three locations in this subunit where mineral content is greater than 40%: 41-44 cm (1800-1785 CE, 48%), 33-35 cm (1900-1870 CE, 45%), and 16-17 cm (1990-1985 CE, 45%). The ASI values associated with these peaks are 12.8 g/m<sup>2</sup>·yr, 5.16 g/m<sup>2</sup>·yr and 29.3 g/m<sup>2</sup>·yr, respectively. The ASI is consistently high in subunit 4b with a mean value of 8.96 g/m<sup>2</sup>·yr.

#### *Tourbière-du-Lac-Maucôque (TLM)*

The peat core at TLM differs from that of TAC in most respects. Here, the basal sand unit, located between 693-700 cm, has an even higher mineral content of 96%. Above this sand layer, TLM is quite different from TAC with regards to peat composition: at TLM, organic matter is even more present and makes up to 96% of the dry weight, and the core's mean mineral content is 4% (Figure 4.5; see Figure S4 for the full core with the basal sand layer). Overall, TLM is more homogenous than TAC, with its main peat units being ligneous peat towards the bottom, followed by a layer of herbaceous peat, and finally bryophytic peat toward the top. There is a single layer of detritus peat located at 244 cm. The mean DBD is 0.07 g/cm<sup>3</sup>, and varies between 0.04 g/cm<sup>3</sup> and 0.16 g/cm<sup>3</sup>, while the mean CAR is 94.7 g/m<sup>2</sup>·yr, and varies between 57.5 g/m<sup>2</sup>·yr and 171.6 g/m<sup>2</sup>·yr. DBD generally increases with depth, which is consistent with patterns of long-term decomposition in

peatland sequences (Glaser & Janssens, 1986; Payette & Rochefort, 2001) (Figure 4.5). Except for the basal sand unit, there are no other visible sand layers in the core. The total mean ASI of TLM is  $0.64 \text{ g/m}^2\cdot\text{yr}$ , much lower than that of TAC, and it varies between  $0 \text{ g/m}^2\cdot\text{yr}$  and  $16.8 \text{ g/m}^2\cdot\text{yr}$ .

*Unit 1 (568-692 cm, 1850-2955 BCE)* – Unit 1 is composed of highly degraded and layered mixed ligneous and herbaceous peat. Seeds from bog beans (*Menyanthes trifoliata* L.), a common aquatic plant growing in North American shallow water environments (Magnan et al., 2014), were identified throughout unit 1, an indication that TLM started forming in a shallow-water environment. Unit 1 is characterized by a mean DBD of  $0.10 \text{ g/cm}^3$  and a mean CAR of  $98.8 \text{ g/m}^2\cdot\text{yr}$ . Contrary to unit 1 in TAC, unit 1 in TLM has a high mean mineral content at 13.5% and an ASI value of  $3.26 \text{ g/m}^2\cdot\text{yr}$ . There is a peak in mineral content of 28 % at 680 cm (2825 BCE), with a corresponding ASI value of  $14.5 \text{ g/m}^2\cdot\text{yr}$ . There is also another visible sand-enriched layer between 652-656 cm (2505-2555 BCE), which chronologically corresponds with a sand-enriched layer in TAC at 305-309 cm, with a peak mineral content of 33.7%, and a peak ASI value of  $16.8 \text{ g/m}^2\cdot\text{yr}$ . There is a decrease in mineral content and DBD, and an increase in CAR, between subunit 1a (644-692 cm, 2415-2955 BCE) and subunit 1b (568-642 cm, 1855-2390 BCE). Subunit 1a is composed of highly humified peat with small (lengths of a few mm at most) wood fragments and is characterized by a mean DBD of  $0.12 \text{ g/cm}^3$  and a mean CAR of  $83.3 \text{ g/m}^2\cdot\text{yr}$ . This subunit has the highest mineral content of the core (19.5%). Subunit 1b is also composed of highly humified peat, but with large wood fragments up to several centimeters long and is characterized by a mean DBD of  $0.09 \text{ g/cm}^3$  and a mean CAR of  $109.1 \text{ g/m}^2\cdot\text{yr}$ . There is a 12.8% peak in minerals at 570 cm (1865 BCE) with an ASI value of  $5.69 \text{ g/m}^2\cdot\text{yr}$  that corresponds to the transition between unit 1 and unit 2.

*Unit 2 (424-566 cm, 855-1840 BCE)* – Unit 2 in TLM corresponds to a transition from primarily ligneous peat to herbaceous peat and finally bryophytic peat. Above the sand-enriched layer at 570 cm, there is an abrupt transition between unit 1 and 2 at 564 cm (1825 BCE), where the mix of highly decomposed ligneous and herbaceous peat is replaced by herbaceous-dominated peat. Unit 2 is characterized by a mean DBD of  $0.07 \text{ g/cm}^3$  and a mean CAR of  $107.6 \text{ g/m}^2\cdot\text{yr}$ , while mineral content and ASI sharply drop to 2.2% and  $0.04 \text{ g/m}^2\cdot\text{yr}$ . There are two small peaks in mineral content at 478 cm (1220 BCE, 2.5%) and at 470 cm (1165 BCE, 4.8 %). There is a corresponding

ASI value peak only at 478 cm ( $0.55 \text{ g/m}^2\cdot\text{yr}$ ), and none at 470 cm. Remains of bryophytic peat, including *Sphagnum* leaves and stems, begins at 485 cm (1270 BCE).

*Unit 3 (142-422 cm, 1305 CE - 845 BCE)* – Unit 3 is composed of different layers of well-preserved, degraded, or highly degraded bryophytic peat. It is characterized by a mean DBD of  $0.06 \text{ g/cm}^3$  and a mean CAR of  $77.1 \text{ g/m}^2\cdot\text{yr}$ , both of which are stable throughout this unit. Unit 3 is the poorest in minerals and ASI, with a mean mineral content of 1.4% and an ASI value of  $0.01 \text{ g/m}^2\cdot\text{yr}$ . Mineral content is below 2% at all depths of unit 3, except at 244 cm (485 CE, 2%), which corresponds to a layer of detritus peat and is associated to a small ASI value of  $0.13 \text{ g/m}^2\cdot\text{yr}$  and visible peaks in DBD and CAR. The ASI is also low in unit 3 except for an aeolian sand signal at 156 cm (1195 CE) with an ASI value of  $0.38 \text{ g/m}^2\cdot\text{yr}$  that is not associated with a visible increase in mineral content.

*Unit 4 (0-140 cm, 2019-1320 CE)* – Unit 4 is mostly composed of well-preserved bryophytic peat. It is characterized by a low DBD value of  $0.06 \text{ g/cm}^3$  and the highest CAR value at  $114.1 \text{ g/m}^2\cdot\text{yr}$ . Unit 4 is richer in minerals compared to unit 3, with a mean mineral composition of 1.8%, while the mean ASI value is much higher at  $0.12 \text{ g/m}^2\cdot\text{yr}$ . Peaks in mineral composition occur at 108 cm (1530 CE, 2.8%), 32-34 cm (1875-1865 CE, 5.2 %), and at 28 cm (1890 CE, 3.7%) and have corresponding ASI peaks of  $1.11 \text{ g/m}^2\cdot\text{yr}$ ,  $1.05 \text{ g/m}^2\cdot\text{yr}$  and  $0.36 \text{ g/m}^2\cdot\text{yr}$ , respectively. The mineral content and ASI values are consistently higher in the portion from 0-40 cm (2019-1840 CE), a trend that is also visible in the TAC core.

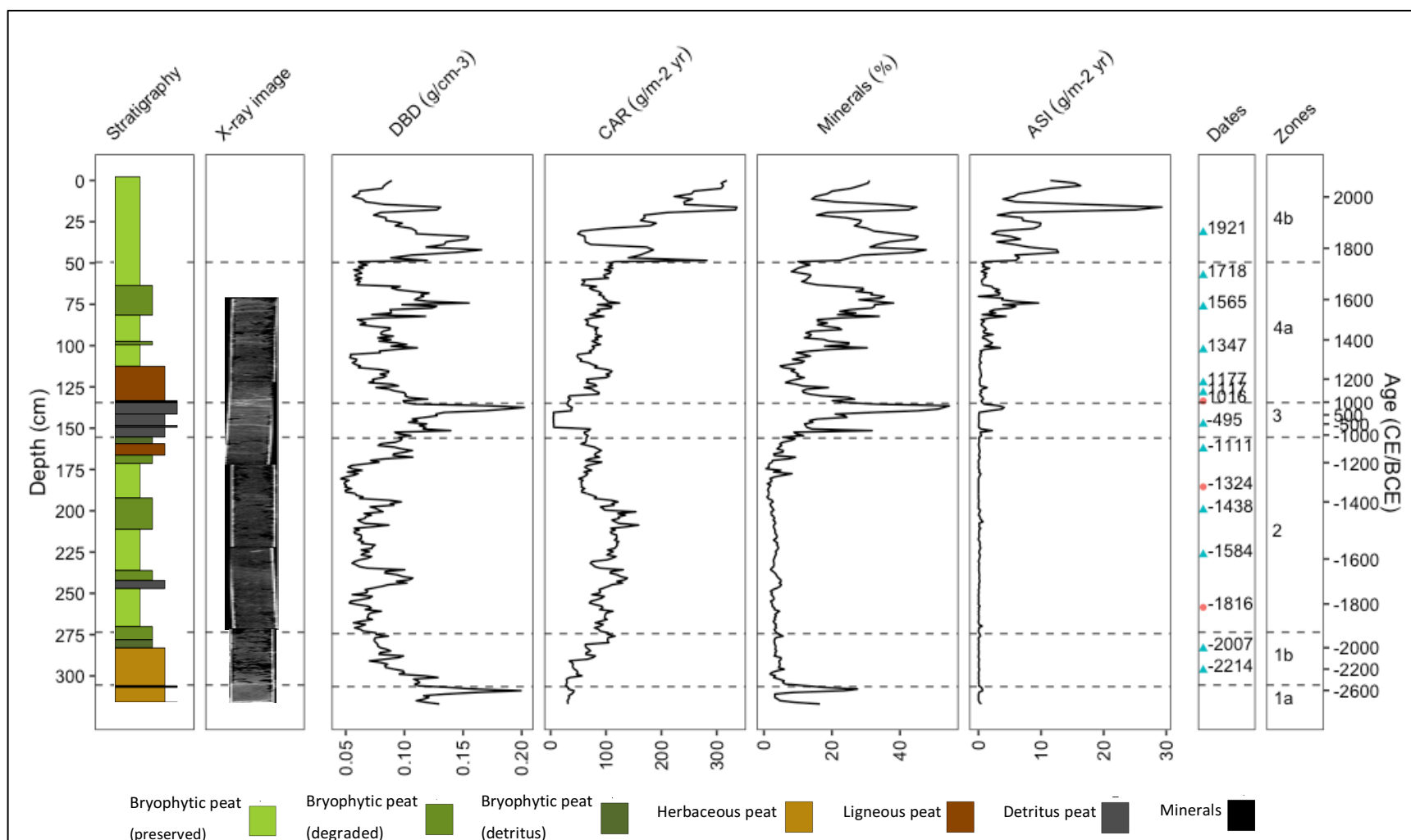


**Figure 4.4** Lithology and sedimentology of the TAC core without the basal sand layers. The core is plotted by depth (left-hand side) with the corresponding age from the age-depth model on the right-hand side, in CE/BCE. The x-ray images were taken by computerized-tomography scanning (CT-Scan). Peat stratigraphy is indicated by color. The width of each layer is a qualitative indication of density. Dry bulk density (DBD) is shown as  $\text{g}/\text{cm}^3$ . Carbon accumulation rate is shown as  $\text{g}/\text{m}^2\cdot\text{yr}$ . Mineral content is the percent of minerals in  $5 \text{ cm}^3$  of dried peat. Aeolian sand influx (ASI) is presented in  $\text{g}/\text{m}^2\cdot\text{yr}$  per year. Modelled AMS  $^{14}\text{C}$  dates are shown as a blue triangle for a date from wood, and as a red circle for a date from bulk peat. Core units calculated by CONISS algorithm are also shown on the right of each plot.

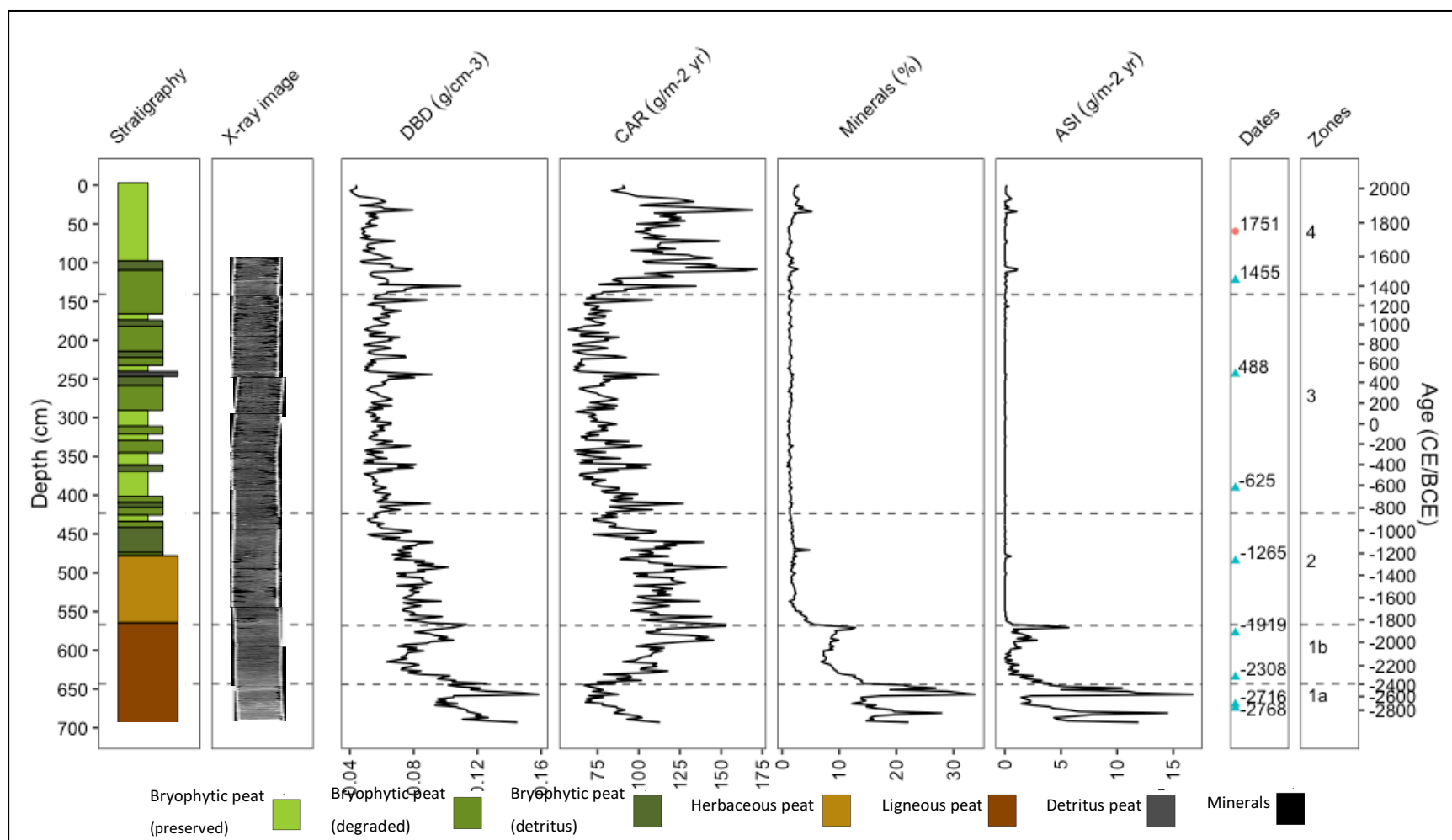


**Figure 4.5** Lithology and sedimentology of the TLM core without the basal sand layers. The core is plotted by depth (left-hand side) with the corresponding age from the age-depth model on the right-hand side, in CE/BCE. The x-ray images were taken by computerized-tomography scanning (CT-Scan). Peat stratigraphy is indicated by color. The width of each layer is a qualitative indication of density. Dry bulk density (DBD) is shown as  $\text{g/cm}^3$ . Carbon accumulation rate is shown as  $\text{g/m}^2\text{-yr}$ . Mineral content is the percent of minerals, in  $5 \text{ cm}^3$  of dried peat. Aeolian sand influx (ASI) is presented in  $\text{g/m}^2\text{-yr}$  per year. Modelled AMS  $^{14}\text{C}$  dates are shown as a blue triangle for a date from wood, and as a red circle for a date from bulk peat. Core units calculated by CONISS algorithm are also shown on the right of each plot.

#### 4.4.4 $\mu$ -XRF elemental downcore variations

The XRF results include 20 elements, but we focus our analysis on the 10 elements that were either the most abundant in the core, or that we considered of importance for storm detection (Figures 6 and 7). The XRF elemental variations throughout the two cores (excluding the basal sand layers) are shown in Figure 4.6A and Figure 4.7A, together with black lines showing the smoothed data, where data points were averaged every centimeter. A PCA was applied to these 10 elements for TAC and TLM separately. Sedimentological variables were passively incorporated into the PCA, and the basal sand layers were excluded from the PCA. The results from the DCA show that a PCA is appropriate for both cores as all gradient lengths are less than 3 (Table S3). The first three principal components (PCs) were considered for analysis and tested for significance (see Figure S5 for PCA significance tests). For TAC, the first three PCs were significant at the 0.05 significance level; for TLM, only the first two PCs were significant at the 0.05 significance level. Therefore, only the results from PC1 and PC2 for TLM and TAC are presented in the text (Table 4.2). Biplots of the PCAs are presented in Figure 4.8, while Figures 4.6B and 4.7B show PC1 and PC2 plotted as a function of depth/age smoothed by solid black lines. Only the statistically significant ( $p < 0.05$ ) relationships between the variables and the PC axes are discussed in the text.

*Tourbière-de-l'Anse-à-la-Cabane (TAC)* – The downcore trends of the elemental counts of the terrigenous elements K, Ti, Si and Zr are similar (Figure 4.6A) and parallel the TAC's mineral content (Figure 4.4): these elements have high variability and are relatively higher in subunit 1a, unit 3 and subunit 4b, which are also higher in mineral content, and are relatively lower in subunit 1b, in unit 2 and in subunit 4a, which are lower in mineral content. The marine-related elements Br and Cl show similar variations throughout the core and closely follow the variations of the terrigenous elements K, Ti, Si and Zr, except in subunit 4b, close to the core top, where Br shows limited variation and where there is a peak in Cl around 12 cm (1996 CE) that is not visible in the other elements, except for Ca (Figure 4.6A). Iron (Fe), Mn, Ca and S behave similarly: these elements do not vary as much as the other elements, and they are not associated with the large peaks in mineral content visible in subunit 1a and unit 3 (Figure 4.4). Iron (Fe), however, shows similar variations to the elements K, Ti, Si and Zr in subunit 4b, near the surface. This is consistent with Fe's known mobility in the peat column (Croudace & Rothwell, 2015); when Fe is deposited in a peatland, it behaves like other terrigenous elements, but as peat accumulates and Fe gets buried

lower into the peat column and under the water table, it becomes mobile, accumulates deeper in the peat, and behaves like Mn, Ca and S, which are also mobile (Kylander et al., 2020). There is a visible drop in Fe, Mn, Ca and S around 238 cm (1665 BCE). Subunit 4b shows the most variability, with visible short-term peaks in the K, Ti and Si record.

*Tourbière-du-Lac-Maucôque (TLM)* – The downcore trends in elemental counts in TLM (Figure 4.7A) show some similarities to that of TAC (Figure 4.6A). Overall, the abundance of K, Ti, Si and Zr in TLM is higher in unit 1, and lower in units 2, 3 and 4, reflecting the distribution of mineral content in the core (Figure 4.5). While K, Ti, Si and Zr co-vary with mineral content in subunit 1a (Figure 4.5), it is Fe and Mn that co-vary with the mineral content in subunit 1b, perhaps indicating a change in mineral source in TLM between subunit 1a and subunit 1b. Contrary to what is seen in TAC, Br and Cl do not seem to co-vary with the terrigenous elements K, Ti, Si or Zr in any of the units, and they both show low kCPS and little variability throughout the core, except for Cl that increases slightly in unit 4 close to the core top like in TAC. Iron (Fe), Mn, Ca and S are most abundant towards the bottom of the core in unit 1, before decreasing at the boundary between unit 1 and unit 2. These elements decrease steadily in unit 2 and stabilize in low abundance in unit 3. All elemental counts in unit 2 and 3 are low, reflecting the low content in minerals in those units. The only exceptions are some small peaks that are visible mostly in the Ti and Fe records. As in TAC, unit 4 shows some variability, with corresponding peaks in Ti and Fe at 24 cm, while K, Ca and Cl all show an increase in the top 25 cm, but overall, the elemental concentrations a core top are much lower than what is seen at TAC.

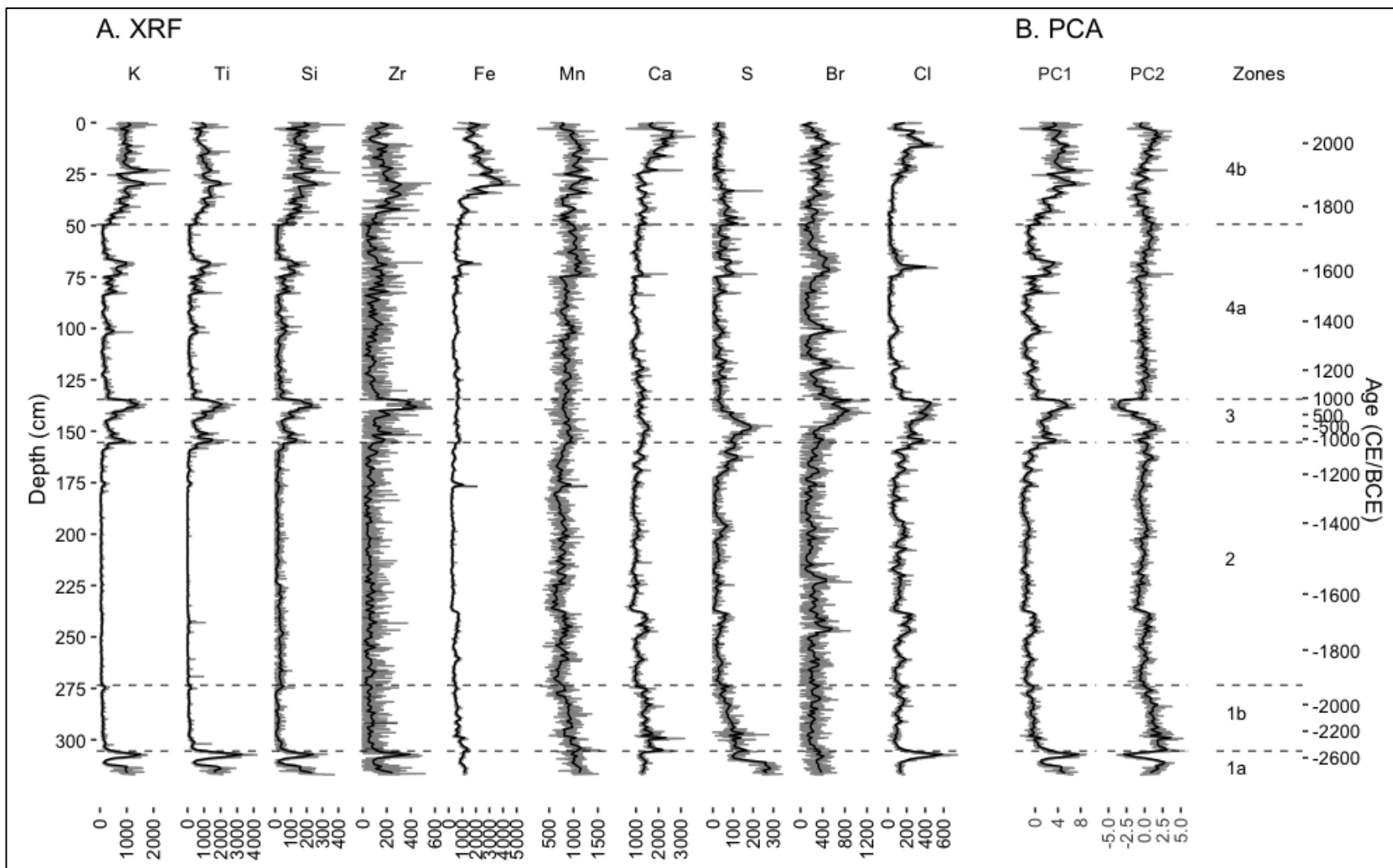


**Figure 4.6** TAC XRF data (A) and principal component results (B), by zones. XRF data are expressed in thousands counts per second (kCPS). The black lines in A and B are smoothers, showing data averaged every centimeter

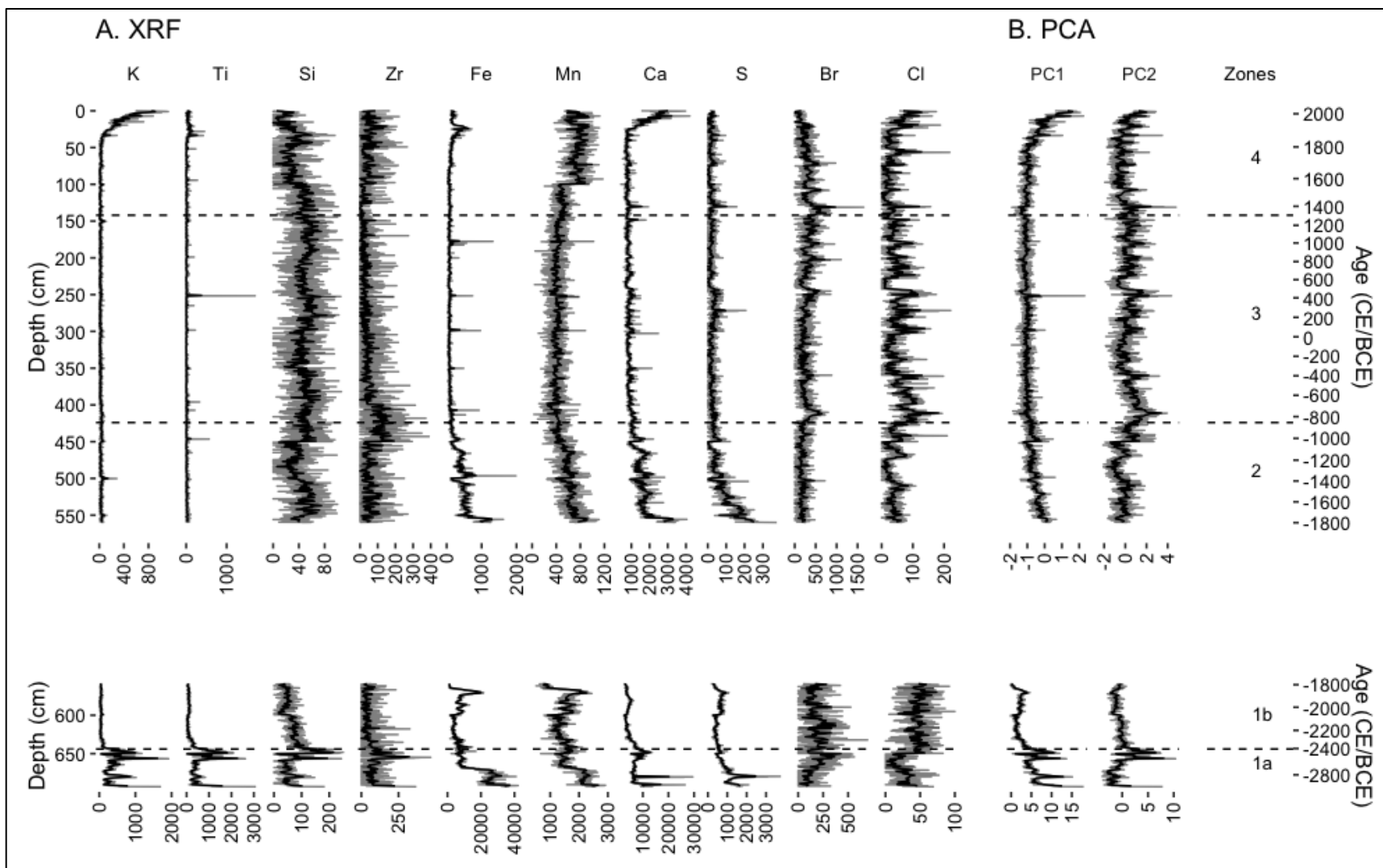


**Figure 4.7** TLM XRF data (A) and principal component results (B), by zones. XRF data are expressed in thousand counts per second (kCPS). The black lines in A and B are smoothers, showing data averaged every centimeter. Note the break in the y-axis near 550 cm and the different x-axis scales in these two sections.

#### 4.4.5 PCA and biplot of elemental data

*Tourbière-de-l'Anse-à-la-Cabane (TAC)* – The first two PCs in the TAC geochemical dataset explain 60.5% of the total data variance (Table 4.2 and Figures 4.8). PC axis 1 explains 47.8% (95% CI = 47-48.6%) of the variance and is positively correlated to all elements. The main significant contributors to PC axis 1 are K, Ti, Si and Fe, and it is positively correlated with the supplementary variables DBD, CAR, mineral content and ASI (Table 4.2). PC axis 2 explains 12.7% (95% CI = 12.2-13.5%) of the variance. The main significant contributors to PC axis 2 are Ca, S, Mn (positive correlations) and Zr (negative correlation). PC2 is also negatively correlated to DBD and mineral content (Table 4.2). The biplot in Figure 4.8 shows that the elements are distributed between two main groups along the PC2 gradient: the terrigenous elements K, Ti, Si and Zr, along with Br and Cl on the negative side of PC2, and the redox-sensitive elements Mn and Fe, and the carbonate elements Ca and S, on the positive side of PC2. However, Fe sits between those groups, showing that it shares characteristics of both. PC1 scores at TAC are mostly positive for the samples from subunit 1a, unit 3 and subunit 4b, which are all mineral-rich (Figure 4.6A).

*Tourbière-du-Lac-Maucôque (TLM)* – The first two PCs in the TLM geochemical dataset explain 61.3% of the total data variance (Table 4.2 and Figure 4.8). PC axis 1 explains 47.1% (95% CI = 46.3-48.3%) of the variance and is positively related to all variables, except Cl and Br. The main significant contributors to PC axis 1 are Ca, S, Mn, Fe and Ti, and it is positively correlated to minerals, ASI and DBD (Table 4.2). PC axis 2 explains 14.1% (95% CI = 13.5-14.9%) of the variance. The main significant contributors to PC2 are Si, Cl and Br (positive correlations). PC2 is also negatively correlated with CAR and has a very weak positive correlation with ASI (Table 4.2). The biplot in Figure 4.8 shows that, in a similar manner to TAC, the elements are divided into two groups: the terrigenous elements K, Ti, Si and Zr, as well as Br and Cl, form one group which all score positively along PC axis 2, while Ca, S, Mn and Fe form a second group, with generally negative scores on PC axis 2. PC1 scores are mostly negative for samples in mineral-poor units 2 and 3, and mostly positive for samples in mineral-rich units 1 and 4 (Figure 4.8 and Figure 4.7A).

**Table 4.2** Correlations between the first two principal components (PCs), and the XRF variables and supplementary variables for TAC and TLM. Only the first two statistically significant ( $p < 0.05$ ) PCs are shown. Statistically significant ( $p < 0.01$ ) correlations are shown in bold dark blue (positive correlations) and bold red (negative correlations). Non-statistically significant correlations are in black.

|                                      | PC1            |                  | PC2              |                  |
|--------------------------------------|----------------|------------------|------------------|------------------|
|                                      | TAC            | TLM              | TAC              | TLM              |
| <b>% variance explained (95% CI)</b> | 47.8 (47-48.6) | 47.2 (46.3-48.3) | 12.7 (12.2-13.6) | 14.1 (13.5-14.9) |
| <b>Cumulative %</b>                  | 47.8           | 47.2             | 60.5             | 61.3             |
| <i>PCA Variables</i>                 |                |                  |                  |                  |
| Cl                                   | <b>0.59</b>    | <b>-0.06</b>     | <b>-0.11</b>     | <b>0.57</b>      |
| Br                                   | <b>0.44</b>    | <b>-0.28</b>     | <b>-0.22</b>     | <b>0.43</b>      |
| S                                    | <b>0.44</b>    | <b>0.91</b>      | <b>0.53</b>      | <b>-0.23</b>     |
| K                                    | <b>0.92</b>    | <b>0.75</b>      | <b>-0.18</b>     | <b>0.34</b>      |
| Ti                                   | <b>0.89</b>    | <b>0.81</b>      | <b>-0.22</b>     | <b>0.35</b>      |
| Si                                   | <b>0.89</b>    | <b>0.41</b>      | <b>-0.20</b>     | <b>0.60</b>      |
| Zr                                   | <b>0.62</b>    | <b>0.25</b>      | <b>-0.45</b>     | <b>0.32</b>      |
| Fe                                   | <b>0.76</b>    | <b>0.86</b>      | <b>0.17</b>      | <b>-0.28</b>     |
| Ca                                   | <b>0.59</b>    | <b>0.93</b>      | <b>0.58</b>      | -0.02            |
| Mn                                   | <b>0.55</b>    | <b>0.87</b>      | <b>0.51</b>      | <b>-0.27</b>     |
| <i>Supplementary Variables</i>       |                |                  |                  |                  |
| DBD                                  | <b>0.68</b>    | <b>0.77</b>      | <b>-0.10</b>     | -0.02            |
| CAR                                  | <b>0.14</b>    | <b>0.05</b>      | 0.00             | <b>-0.23</b>     |
| Minerals                             | <b>0.65</b>    | <b>0.94</b>      | <b>-0.30</b>     | 0.00             |
| ASI                                  | <b>0.50</b>    | <b>0.45</b>      | 0.00             | <b>0.09</b>      |

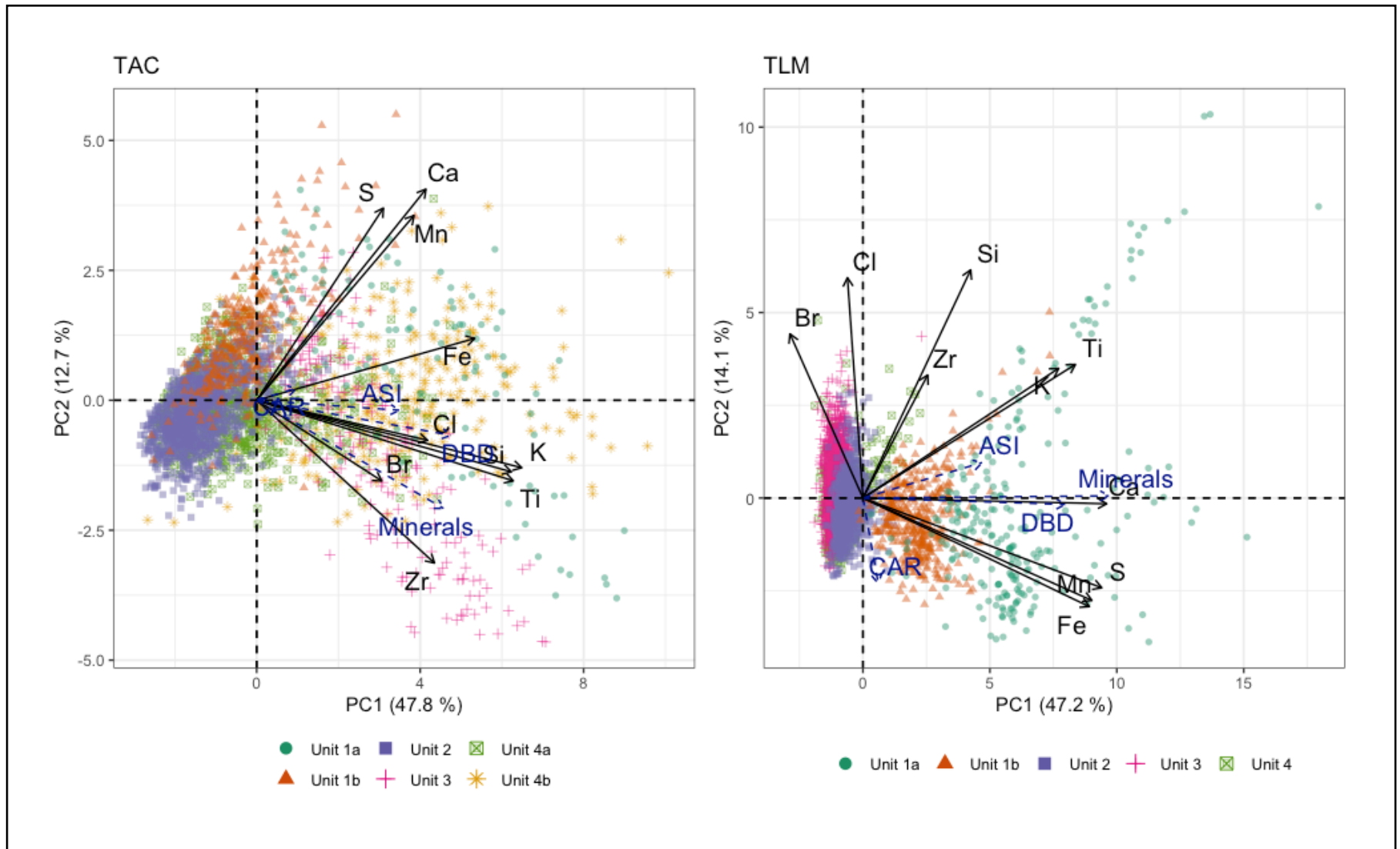


**Figure 4.8** PCA analyses of the 10 major elements for TAC and TLM. Each subunit is represented by a different colored symbol. The supplementary variables (CAR, ASI, DBD and Minerals) are represented by the dashed blue arrows, while the variables used in the PCA analysis are in solid black. Note that the CAR arrow in TAC overlaps with the Fe arrow and that the DBD arrow in TLM overlaps with the Ca arrow.

#### 4.4.6 Processes controlling sediment inputs at each core site

In both the TAC and TLM cores, PC axis 1 can be interpreted as being an indication of mineral inputs, which is consistent with other studies applying PCA to geochemical datasets from highly organic cores (Kylander et al., 2020; Pratte et al., 2017). PC 2 axis allows the identification of two main groups of elements in the cores: K, Ti, Si, Zr, Br and Cl as group 1, and Ca, S, Mn and Fe as group 2.

The surface geology of the Magdalen Islands suggests that the mineral source for the elements of group 1 is mostly local sand from the beaches and sandstone. Quartz ( $\text{SiO}_2$ ) is a major component of the sandstone and sand on the Magdalen Islands (Sabina, 2003), while k-feldspar ( $\text{KAlSi}_3\text{O}_8$ ), rutile ( $\text{TiO}_2$ ), and ilmenite ( $\text{FeTiO}_3$ ) are fairly weather resistant and found in coarse beach sand (Howie, Zussman, & Deer, 1992; Shotyk et al., 2001). Additionally, Br and Cl, which can be indicators of sea-spray (Moreno et al., 2017), also occur in group 1. The elements from group 2 are redox-sensitive and mobile in the peat column and are associated with sulphides, sulphate and carbonate minerals like pyrite ( $\text{FeS}_2$ ), gypsum ( $\text{CaSO}_4$ ), calcite ( $\text{CaCO}_3$ ), and dolomite ( $\text{MgCO}_3 \cdot \text{CaCO}_3$ ) (Howie et al., 1992), which could be derived from the gypsum and dolomite deposits mixed with manganese that are fairly abundant on *Ile-du-Havre-Aubert*, near La Butte des Demoiselles (Sabina, 2003).

One can roughly associate a specific process with each of these two groups of elements. In general, the elements from group 1 can be indicative of aeolian processes, since they are associated with both the coarse minerals from the beach and sandstone, as well as sea-spray (Br and Cl), which rely on winds for transport to the peatlands, at least in the ombrotrophic portion (Orme et al., 2015; Stewart et al., 2017). However, the presence of elements from group 1 in the core could indicate transport through air suspension (which necessitates a high wind threshold, for example that which occurs during intense storms) and/or through creeping and saltation (particles drifting or rolling on or close to the surface, which happens at lower wind speeds) (Anderson, Sørensen, & Willetts, 1991). The elements from group 2 can also be indicative of aeolian processes, but because they are also less resistant to weathering (they react with oxygen and water (Howie et al., 1992)), they are probably associated with the transport of smaller mineral particles in the peatland, either through the aeolian processes described above, or by upward mineral dissolution from the sediments below the peatland (Shotyk et al., 2001). As such, the much larger concentration of elements from group 2 in the basal layer of TLM compared to TAC could indicate differences in

the sedimentological substrate (Shotyk, 1996), with gypsum and dolomite deposits being dominant under the TLM peatland. As the elements associated to these minerals are redox-sensitive, they can indicate intense interaction with groundwater and with the water table depth, with a larger concentration of elements from group 2 meaning wetter conditions and shallow water table, and vice-versa (Steinmann & Shotyk, 1997). Additionally, in early minerotrophic peatland developmental stages, elements from group 2 could have been supplied to the peatland by surface water that has reacted with sulphates, sulphides and carbonates minerals (Shotyk, 1996).

#### *4.4.7 Insights from core sedimentology and geochemistry on peatland development*

In this section, I will discuss peatland development from the mid to late Holocene at TAC and TLM and examine sediment input and provenance at each site. Figure 4.9 presents selected sedimentological and geochemical variables (CAR, minerals content, ASI and PC2) for TAC and TLM spanning the mid to late Holocene. Note that the sign of PC2 for TAC is reversed from how it is reported in Table 2 and Figure 8 so that the direction of effect is the same between the two cores, with positive values meaning relatively more elements from group 1 (aeolian) and negative values meaning relatively more elements from group 2 (redox-sensitive).

*Early peatland formation (3000-2600 BCE)* – The differences in the deepest peat recovered from TAC and TLM that date between 3000-2600 BCE suggest that the sites likely formed in different environments (Figure 4.9). The initial layers were deposited as highly degraded and slightly laminated mineral-rich peats (Figures 4.4-4.5) corresponding to the elevated mineral content seen in both cores (Figure 4.9). At TAC, the presence of herbaceous remains mixed with relatively small ligneous fragments suggest that the peatland originally formed as a fen, directly above the basal mineral layer. The absence of large wooden remains indicates that the site was not heavily forested at the time of peat inception, meaning that the peatland formed through primary paludification (i.e. a direct shift from bare land to peatland) (Kuhry & Turunen, 2006). At TLM, the presence of *Menyanthes trifoliata* seeds within a matrix of herbaceous and ligneous peat, suggests an initial shallow water environment (Hewett, 1964) and formation of the peatland through terrestrialization of a water body (Kuhry & Turunen, 2006). This is further supported by the high mineral content in TLM subunit 1a compared to TAC (Figure 4.5B, 19.7% vs 11%) and the accumulation of Fe and Mn near the base of the core (Figures 4.7A). The abundance of and

strong correlation between Mn and Fe at TLM suggests that their presence in subunit 1a was controlled by redox processes associated with high water content (Kylander, Ampel, Wohlfarth, & Veres, 2011).

*Trophic transitions and pathways to ombrotrophy (2600-1000 BCE)* – The period after 2600 BCE is characterized by important changes at both sites, characterized by a sharp and relatively short-lived increase in mineral content between 2615-2465 BCE at TAC (150 years) and 2580-2410 BCE at TLM (170 years) (Figures 4.9). The synchronicity of this signal at both TAC and TLM suggests a climatically-induced change in the peat environment: the period from 2400-1000 BCE marks the end of the Holocene Climate Optimum (HCO) in the GSL, with decreasing temperatures and moderately elevated precipitation (Sauvé, 2016). There are no increases in Fe or Mn that suggest a switch to a wetter environment during that period (Kylander et al., 2011), but a positive phase of PC2 (relatively larger concentration of group 1 elements in the core) at both sites suggests enhanced aeolian activity (Figures 4.9). This large input of minerals probably helped initiate the trophic transition that is visible after 2400 BCE at both TAC and TLM and that corresponds to subunit 1b. That is, a fen environment without ligneous remains was established at TAC from 2465-1920 BCE, with the first noted presence of *Sphagnum* remains visible by 2090 BCE, suggesting a more open peatland (Peros et al., 2016). At TLM, a forested wet fen was established between 2410-1825, as indicated by the presence of large wooden fragments, the trend towards a negative PC2 (Figure 4.9), and quantity of Fe and Mn during that period (Figure 4.7). This was followed by an abrupt transition to a dry herbaceous-dominated fen at TLM at 1825 BCE, visible in the steep decrease in minerals and a switch to a more positive phase of PC2 (fewer reducing elements) (Figure 4.9). This dryer fen environment at TLM persisted until the first appearance of *Sphagnum* at ca. 1330 BCE and corresponds roughly to unit 2. At both sites, the transition into ombrotrophy probably followed the first appearance of *Sphagnum* remains, which became dominant at ca. 1920 BCE for TAC and at ca. 1270 BCE at TLM. Ombrotrophic peat sections are isolated from the water table, resulting in a decrease in the accumulation of reducing elements (Shotyk, 1996). Indeed, at both sites, the switch towards *Sphagnum* dominated peat was quickly followed by decreases in Fe, Mn, Ca and S (resulting in positive PC2 values) that are visible at ca. 1670 BCE for TAC and at ca. 1030 BCE for TLM, which means there was a lag of about 250 years between the moment that *Sphagnum* became dominant and the full ombrotrophication of each site.

*Neoglacial Cooling (1000 BCE-1000 CE)* – The period starting from 1000 BCE to 1000 CE is marked by an abrupt transition from ombrotrophic conditions to dry, mineral-rich ligneous peat at TAC between 1100 BCE and 970 CE, while at TLM it corresponds to a relatively stable period of ombrotrophic conditions (Figure 4.9). These changes correspond to unit 3 in both cores and could be related with the onset of Neoglacial cooling, which lasted for a period of about 2000 years from 1000 BCE to 1000 CE in the GSL (Magnan et al., 2014; Peros et al., 2016; Perrier, Garneau, Pratte, & Sanderson, 2022; Viau, Gajewski, Sawada, & Fines, 2006). During that period at TAC, the CAR is very low, and there is a trend of increasing mineral content that culminates at ca. 970 CE in a sudden delivery of sand and finer sediment (Figure 4.9). The origin of the two mineral-rich peaks at 970 BCE and 970 CE is unclear, as they have no equivalent in the TLM record. The second and most recent peak (970 CE) is dominated by elements from group 1 (coarse sand fraction), the sources of which were perhaps migrating sand dunes, as they are a prominent feature on the Magdalen Islands coastal landscape (Hétu et al., 2020). The first and older peak (970 BCE), however, has a different geochemical signature: it is dominated by elements from group 2 (redox-sensitive elements). One hypothesis for the cause of this prominent sand layer is that a shallow water pool developed at TAC during the early Neoglacial period, leading to the accumulation of Fe and Mn rich minerals in the sediments, and, upon drying, only the minerals were left behind. Nevertheless, this would necessitate a drastic and rapid change in the hydrology of TAC, a question that is outside the scope of this current work.

*Late Holocene peatland development (1000-2019 CE)* – Following the Neoglacial period after 1000 CE, there is a return to ombrotrophic conditions at TAC as shown by the abundance of *Sphagnum* remains in the ligneous peat (Figure 4.4) and a visible increase in peat productivity (CAR) (Figure 4.9). A return to optimal peat development is associated with the transition into the Medieval Climate Anomaly, a period of elevated temperatures and precipitation in the GSL (Sauvé, 2016; Wu, de Vernal, Fréchette, Moros, & Perner, 2022). At TAC, during the period from 1000-1350 CE, CAR increases and mineral content decreases, while conditions are stable at TLM during that time and show only a slight increase in CAR (Figure 4.9). The period after 1350 CE is when the ASI signal starts increasing in both cores, but mostly in TAC (Figure 4.9). CAR is at its highest in both TAC and TLM during the period from 1350 CE to the present. There is an increase

in sediment in both cores starting ca. 1900 CE, which continues to the present and is evidence of human impacts because of widespread forest clearance and mining for building purposes (Figure 4.9).

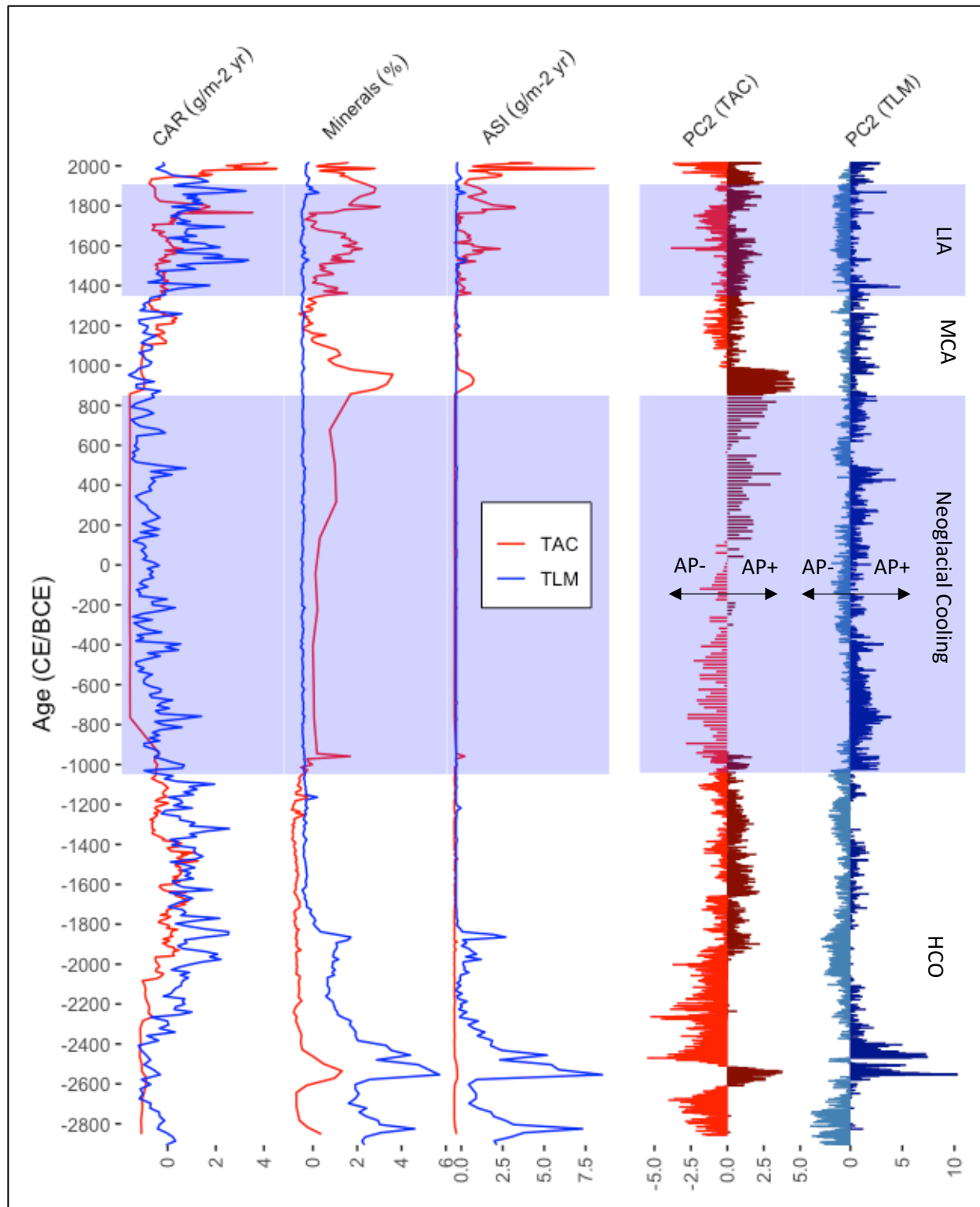


**Figure 4.9** Comparison of selected sedimentological and geochemical variables between the two Magdalen Islands sites (TAC in red and TLM in blue) plotted by age (CE/BCE). Note that the sign of PC2 for TAC is reversed from how it is reported in Table 2 and Figure 8 so that the direction of the effect is the same between the two cores, with positive values meaning relatively more elements from group 1 (enhanced aeolian processes [AP+]) and vice-versa (AP-). Blue zones represent documented periods of cold climate in the northern hemisphere: the Neoglacial cooling from 1050 BCE – 850 CE and the Little Ice Age (LIA) from 1350-1910 CE, while the white zones are periods of warmer climate: the Holocene Climate Optimum (HCO) from 9700 – 1000 BCE and the Medieval Climate Anomaly (MCA) from 950-1350 CE (Magnan & Garnau, 2014).

#### 4.4.8 Reconstructing storminess over the past 168 years

*Storm proxy and suitability of the core for paleo-storms analysis* – All elements from group 1 (K, Ti, Si, Zr, Br and Cl), as well as PC axes 1 and 2, were considered as potential storm proxies, but Ti was chosen as the best indicator of storms because it is a conservative element abundant in both cores related to the coarser grain fraction that is mostly of aeolian origin, and it is not mobile in the peat column. In paleoclimate studies, Ti is often regarded as the most reliable indicator of detrital inputs (Croudace & Rothwell, 2015). Bromine (Br) has also been used as a storminess indicator because it is present in seawater (Orme et al., 2015; Stewart et al., 2017), but it was not used here due to its very low concentrations in both cores, particularly TLM. Chlorine (Cl), while also present in seawater, was not used as its signal may be influenced by the presence of a salt (NaCl) mine on the Magdalen Islands (*Les Mines Seleine*). The ASI record was not used as a storm proxy because it is very low in some parts of TLM, and it was measured at a relatively coarse-scale resolution of 1-cm, in contrast to the geochemical variables that have a resolution of 1-mm. The ASI measurements combine all aeolian sand found within 1 cm of peat, making the ASI record more sensitive to longer-term change, hence it may be unable to capture short-term changes in the core such as those caused by storms. Therefore, in this study, ASI is used as an independent proxy of aeolian activity rather than storm activity and is used to verify whether peaks in the Ti records are associated with aeolian sand or not.

In order to be reliable archives of atmospheric processes, peatlands must display ombrotrophic conditions (Pratte, Mucci, & Garneau, 2013). Therefore, it is important to select the core sections that are ombrotrophic to avoid different modes of sediment delivery that are not aeolian-related. The sedimentological and geochemical profiles of the cores clearly indicate that they were not ombrotrophic in some sections: TAC probably displayed ombrotrophic conditions between 1920-1100 BCE, and from 1000 CE to the present, while TLM probably displayed ombrotrophic conditions from 1270 BCE to the present. Nevertheless, without a more complete analysis of macrofossils and *Sphagnum* remains, we are not able to pinpoint exactly the location and timing of the ombrotrophic transition. Therefore, to reduce the risk of including non-ombrotrophic sections in our analysis, we decided to reconstruct the paleo-storm records for the period from 1000 CE to the present, for both cores. The ombrotrophy of the cores is more certain during that period and it enables us to compare the storm records from both locations.

*Instrumental records of storms* – The IBTrACKS hurricane dataset reveals that 42 hurricanes passed within less than 100 km from the Magdalen Islands between 1851-2019 (Figure 4.10 and Table S4). While the wind speeds reported range between 46 km/h and 157 km/h, the 5 hurricanes that had an impact on the Magdalen Islands (identified in red in Figure 4.10) all had winds above 110 km/h. The Historical Weather dataset revealed that, between 1985 and 2019, winds above 110 km/h were recorded 13 times on the Magdalen Islands, with 5 of those episodes having winds above 115 km/h (Figure 4.10 and Table S5). The only event that is recorded in both the IBTrACKS and the Historical Weather datasets is Hurricane Dorian that struck the Magdalen Islands on September 7<sup>th</sup>, 2019. We therefore expect those hurricanes with a minimum wind speed of 110 km/h and other types of events with a minimum wind speed of 115 km/h to be significant events for this study.

*Calibration of the Ti record* – Given these storm records, about 5 hurricanes hit hard per 168 years and about 5 other types of wind events (not hurricane related, so excluding the wind event related to Hurricane Dorian in the Historical Weather dataset) have occurred per 35 years (or 24 other types of wind events per 168 years) on the Magdalen Islands during the timeframe of these datasets. These two statistics were used to calibrate the Ti CPS record over the period 1851-2019 and generate a storm record. It is important to note that the calibration was done only using the TAC data site, as the TLM core was not dated with <sup>210</sup>Pb and has large age uncertainties in this section, making storm attribution difficult. After subtracting a 30-year running average from the Ti kCPS data, we applied several thresholds to the detrended data to identify storms, from the 90<sup>th</sup> percentile of the cumulative distribution of Ti kCPS, to the 97.5<sup>th</sup> percentile in increments of 2.5 percentile. This gave us between 22 and 6 events between 1851-2019, which falls within the range of wind events (both hurricane and not hurricane related) we would expect to see on the Magdalen Islands during this period. However, by looking at the co-occurrence of peaks in the Ti and ASI records in Figure 4.10, it appears that more than one Ti peak corresponds to only one ASI peak; in other words, some Ti peaks are grouped in clusters that corresponds to one ASI peak. Four such clusters were identified in the period 1850-2019 CE and are indicated in Figure 4.10 as grey shaded boxes. Given the overlapping age-uncertainties around the Ti peaks in these clusters, it is difficult to say with certainty whether each Ti peaks represent a single storm event or if they pertain to the same storm event. Therefore, to avoid overestimating the number of events identified with the Ti-

over-threshold method, the threshold for TAC was set to the 95<sup>th</sup> percentile, while the threshold at TLM was set to the 92.5<sup>th</sup> percentile, as it is expected that TLM is less sensitive to storms due to its location that is more inland and sheltered.

*Event attribution* – With the technique described above, 11 events were identified in the Ti record (indicated as red points in Figure 4.10) which are grouped into 4 clusters (indicated by the grey shaded boxes in Figure 4.10). Each cluster is associated with a period of increased ASI (the last ASI peak [cluster #4] is not fully visible on Figure 4.10 but can be seen more clearly in Figure 4.11). Cluster #1 contains two events that were dated to 2018 CE (2017-2019 CE) and 2015 CE (2014-2016 CE). The most recent event from cluster #1 may represent Hurricane Dorian (September 7<sup>th</sup>, 2019). Dorian, one of the most powerful hurricanes in the Atlantic Ocean on record, tracked about 40 km north of the Magdalene Islands, registering winds at that position of 140 km/h (Knapp et al., 2010), as well as a storm surge of 1.6 m over the predicted tide (Jardine, Wang, & Fenech, 2021). The second event from cluster #1 could be Hurricane Arthur, for which tropical storm and wind warnings were issued to the Magdalen Islands between July 2<sup>nd</sup> and July 6<sup>th</sup> of 2014 (Canadian Hurricane Center, 2014). However, no damage was reported on the Magdalen Islands related to this event, making its attribution less likely. Cluster #2 contains 3 events with age uncertainties ranging between 1996-1984 CE. They correspond to the largest ASI peak in the period from 1850-2019 CE. During that period, two hurricanes tracked close to the Magdalen Islands: Hurricane Bob in 1991 and Hurricane Alberto in 1988. Hurricane Alberto did not have significant impacts in Eastern Canada (Environment and Climate Change Canada, 1988), while Hurricane Bob did leave severe impacts in New Brunswick, Nova Scotia, and Prince Edward Island, but no impacts were reported for the Magdalen Islands (Environment and Climate Change Canada, 1992). Therefore, it is likely that the events associated with cluster #2 were caused by another type of event, possibly a nor'easter. Notable nor'easters happened on November 7<sup>th</sup>, 1994 (peak wind gusts of 130 km/h) and on December 4<sup>th</sup>, 1989 (peak wind gusts of 122 km/h) and caused notable impacts on the Magdalen Islands (Bernatchez, Boucher-Brossard, & Sigouin-Cantin, 2012). Cluster #3 contains 5 events with age uncertainties ranging between 1950-1929 CE. While there is no known hurricane that had an impact on the Magdalen Islands during this period, this cluster corresponds to a period of heightened hurricane activity in the GSL, when at least 8 hurricanes tracked close to the Magdalen Islands (Figure 4.10). It is also possible that the events

from cluster #3 are related to the unnamed hurricanes of 1927, known as the 1927 August Gale, and for which the impacts across the GSL are well documented. Finally, it is not possible to attribute the last event identified in the record, which corresponds to cluster #4, since its age uncertainty also includes the period before 1851 for which there is no data on hurricanes.

It is clear from the analysis above that attributing a known event to Ti peaks in the core records is very difficult, especially because of the age uncertainty around those peaks and the possible post-depositional movement of mineral particles and geochemical elements in the peat matrix. It also appears that the storm record at TAC, and most probably at TLM, is sensitive to both hurricanes and other types of events, as suggested by cluster #2. However, it is important to note that the record is not sensitive to all events. One hurricane that caused severe damage to the Magdalen Islands is hurricane Blanche in 1975, with winds up to 115 km/h accompanied by 120 mm of rain (Public Safety Canada, 2022), and this event does not seem to have been recorded in the TAC record. Finally, it is difficult to relate the presence of Ti peaks to a precise event due to the lack of reliable data on the relationship between storms' wind strengths and local impacts on the Magdalen Islands. Nevertheless, the concordance between the Ti record and the ASI record indicates the suitability of using Ti as a wind proxy.

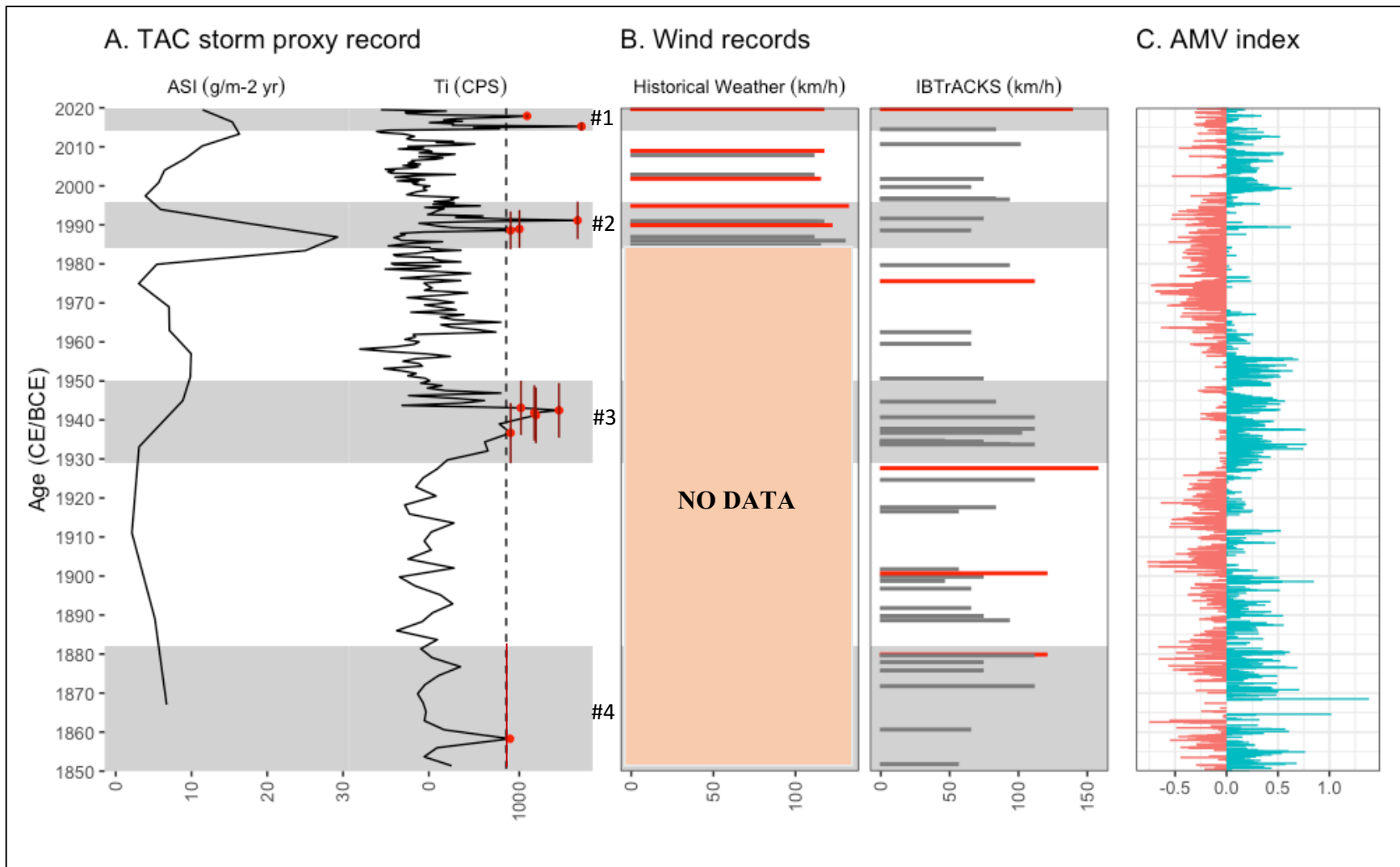


**Figure 4.10** A) Storm proxies from the TAC core for 1850-2019 CE: ASI in  $\text{g/m}^2 \cdot \text{yr}$  and Ti counts. The Ti count data was detrended by subtracting a 30-year moving average. The dotted black line represents the threshold for storm detection, i.e., any Ti measurements above the 95<sup>th</sup> percentile of the detrended Ti count data. All identified storms are identified with a red dot. The grey shaded boxes represents clusters of events, i.e., the range between the positive and negative age uncertainty around the most recent and oldest storm detected within a cluster (indicated by vertical red lines). B) Bar chart of wind data from the IBTrACKS and Historical Weather datasets. For the Historical Weather dataset, only days with winds above 110 km/h are shown. C) All hurricanes that tracked less than 100 km from the Magdalen Islands and peak winds (in km/h) recorded at the hurricane location at the time of passage are shown. Wind events that had a recorded impact on the Magdalen Islands are indicated in red. D) The AMV index from van Oldenborgh, te Raa, Dijkstra, and Philip (2009) with the positive (negative) phases highlighted in blue (red).

#### 4.4.9 Storm frequency over the last 1000 years

Since 1000 CE, the Ti record exceeded the storm threshold 14 times at both TAC and TLM, for an average storm frequency of 1.4 events/century (Figure 4.11). The storm time-series from both TAC and TLM show similar features, highlighting two periods of increased storm frequency during the last ~150 to 200 years and between ca. 1450-1650 CE. It is important to note that the chronology for TLM in the most recent part (~1800-2019 CE) of the record is less reliable compared to that of TAC, with uncertainties around the TLM Ti peaks being much larger than those of TAC (by a factor of about 10), as shown by the age uncertainties around the events identified in Figure 4.11 between ~1800-2019 CE. An alternative age-depth model for TLM in which the  $^{210}\text{Pb}$  values from TAC were used for the TLM core and adjusted for the TLM peat accumulation rate (Supplemental Figure S6), shows a much more rapid PAR at the core top and more similarities between the peaks in the ASI records for TAC and TLM between 1850-2019 CE (Supplemental Figure S7). Therefore, some of the events or event clusters highlighted in pale grey in Figure 4.11 from TAC may be related to apparently older events at TLM, especially in the part of the core that is younger than ca. 1800 CE.

The storm frequency during the historic period (1851-2019 CE) was 6.5 events/century for TAC and 6 events/century for TLM, about 6 times more than the long-term average for both cores. It is not clear whether this discrepancy is caused by a real increase in storm frequency in the last 150 years, a change in the sensitivity of the sites to storms, or a change in the availability of sediments near the sites. At TAC, which has a better age-model for the recent portion of the core, the data shows a clear increase in the number of events identified, particularly after 1930 CE. On the Magdalen Islands, this corresponds to a period of intensive gravel road construction near the sites (Fortin, 2003), which may have delivered new sources of sediment closer to the peatlands. Another possibility to explain why so many storms were identified in the period 1850-2019 is a conservation bias known as the “Sadler effect”, which is the observation that the completeness of a sedimentological record increases when made over smaller timescale (Sadler, 1981; Vachula, Sheppard, & Cheung, 2022). In our case, the lack of compaction in the core top (the acrotelm layer containing living peat (Ingram, 1978)) means that each cm of peat represents a smaller timescale compared to deeper parts of the core, therefore reducing the risk of having multiple events “squished” together by peat compaction.

More definitively, the data from both cores show evidence of more frequent storm activity in the period from ca. 1450-1650 CE, with an average frequency of 2 events/century during this time (Figure 4.11). There appear to be three events dated at ca. 1625 CE (1540-1710), 1590 CE (1510-1660), and 1515 CE (1630-1595) at TAC, and ca. 1590 (1495-1700), 1565 (1470-1675), and 1525 (1440-1630) at TLM. The period from 1000-1450 CE shows no evidence of storms in either core. Overall, the similarity between the two cores suggests reproducibility across at least *Ile-du-Havre-Aubert*, where the two sites are located.

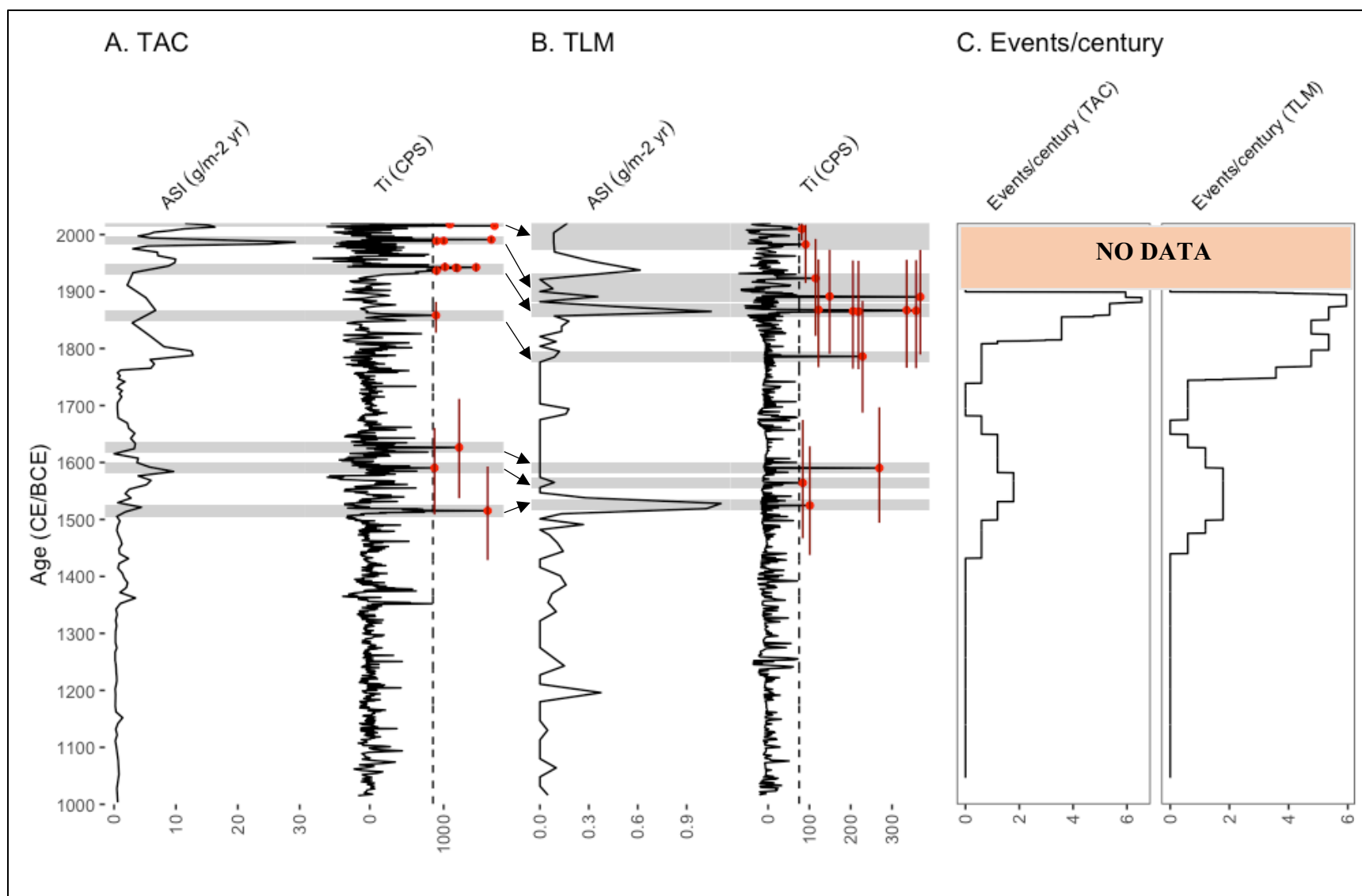


**Figure 4.11** Storm proxies from the TAC (A) and TLM (B) cores for 1000-2019 CE, including ASI in  $\text{g/m}^2 \cdot \text{yr}$  and Ti counts. The Ti count data was detrended by subtracting a 30-year moving average. The dotted black line in A and B represent the threshold for storm detection, i.e., any Ti measurements above the 95<sup>th</sup> percentile of the detrended Ti count data are counted as storms. All storms are identified with a red dot, together with their age uncertainty. The grey shaded boxes are used to highlight events or clusters of events. C) Time-series of events/century for TAC and TLM. Given our use of a centered 168 years sliding window to calculate the running sum, we do not have storm frequency data for the first 84 years of the record.

#### *4.4.10 Regional paleostorm patterns and climate*

While the two cores from the Magdalen Islands provide a local record of storm activity for at least the last millennium, we can examine more general, basin-wide trends by comparing our data with other paleo-storm records from the northeast Atlantic Ocean region. A period of increased storm activity was identified on the Magdalen Island between 1450-1650 CE, and several paleo-storm records from this region also suggest heightened storm activity from during that same period (Boldt, Lane, Woodruff, & Donnelly, 2010; Donnelly et al., 2015; Oliva et al., 2018; van Hengstum et al., 2014). A storm reconstruction from Salt Pond, Massachusetts, indicates an active storm period between 1400-1675 CE, with 10 events identified and 2 having been attributed to known hurricanes (the Great Colonial Hurricane of 1635 and the 1675 hurricane) (Donnelly et al., 2015) (Figure 4.12C). At Robinson Lake, Nova Scotia, there is evidence of at least 4 hurricane strikes between 1475-1670 CE based on a bromine lake core record (Oliva et al., 2018), while the record from Mattapoisett Marsh, Massachusetts, shows that the 15<sup>th</sup> and 16<sup>th</sup> centuries were the most active of the last millennium, with 7 storms identified during that period (Boldt et al., 2010). In the northern Caribbean, the Bahamas experienced a particularly active period between 1350 and 1650 CE based on data from a sediment core from Thatchpoint Bluehole (van Hengstum et al., 2014). All these records also show a quiescent period during ca. 1100-1400 CE, similar to the Magdalen Islands (Figure 4.12). The second period of heightened storm activity during the last millennium identified on the Magdalen Islands is between 1800-2019 CE (Figure 4.11-4.12). At Salt Pond and at Robinson Lake, there was evidence of at least one hurricane strike during this period (Hurricane Juan in 2003 at Robinson Lake and Hurricane Bob in 1991 at Salt Pond), but otherwise no significant increase in overall storm activity (Donnelly et al., 2015; Oliva et al., 2018) (Figure 4.12C). Only at Thatchpoint Bluehole in the Bahamas does the record indicates an increase in storms from 1800 CE to the present, following a quiescent period from 1650-1800 CE (van Hengstum et al., 2014).

The consistency between these records, especially with respect to the pre-instrumental period, demonstrates that the Magdalen Islands, and most probably the GSL region, is affected by the same processes driving storminess as those elsewhere on the Atlantic seaboard. It also suggests that the events with the most impact on the Magdalen Islands are mostly hurricanes, or hurricanes downgraded to tropical cyclones. This is an important finding, as there is very little research on long-term hurricane strikes in more northern latitudes, where winter storms and nor'easters also

cause widespread damage (Oliva et al., 2017; 2018). The lack of evidence for storm activity from 1100-1400 CE and, conversely, the consistent evidence for an active period from 1400-1650 CE, suggests basin-wide changes in climate that favors or halts storm activity in the North Atlantic. It has been shown that periods of quiescent and active storm activity alternate between the northeast Atlantic and the Caribbean region; for example, many records from the Gulf of Mexico show an active period between 1100-1400 CE, corresponding to a quiescent period in North Atlantic (Donnelly et al., 2015; Lane et al., 2011; Yang et al., 2020). This suggests that changes in climate factors either halted cyclogenesis (the formation of cyclones) for the North Atlantic and/or affected the storm tracks by steering the storms towards the Caribbean during that period.

An important factor in North Atlantic hurricane frequency is sea-surface temperature (SST), as warm water in the Atlantic Main Development Region (AMDR), which stretches from offshore western Africa to the Caribbean just above the equator line, favors hurricane cyclogenesis (Donnelly et al., 2015; Mann, Woodruff, et al., 2009; McCloskey & Liu, 2012). Related to SST is the Atlantic Multidecadal Variation (AMV), an indicator of SST and sea-level pressure variations between the North and South Atlantic that is related to change in the thermohaline circulation (Figure 10C and 12D) (Klotzbach, Gray, & Fogarty, 2015). A positive AMV indicates above average water temperatures, below average sea level pressure and reduced vertical wind shears over the North Atlantic, all of which favours hurricane formation and intensification (Klotzbach et al., 2015). Positive AMV phases during the 20<sup>th</sup> and 21<sup>st</sup> century were indeed related to particularly active hurricane periods in the eastern North Atlantic basin between 1926-1969 and 1995-2012 (Klotzbach et al., 2015). In Figure 4.10C, the IBTrACKS hurricane record varies with the AMV index: more hurricanes are occurring in the vicinity of the Magdalen Islands when the AMV is positive. All events identified during this period with the Ti record correspond to heightened hurricane activity and a positive AMV index when considering the age-uncertainty around the Ti measurements, thus providing evidence for a relationship between the AMV and storms at the Magdalen Islands, at least during the instrumental period.

On longer timescale, however, the relationship between the AMV and storms in the period 1450-1650 CE at the Magdalen Islands does not hold. While a diatom-based SST reconstruction from Trinity Bay, Newfoundland, suggests a trend of increasing SSTs culminating at ca. 1600 CE (Orme et al., 2021), which corresponds to the active storm period at the Magdalen Islands, the SST at that time was still below the long-term average (with negative anomalies) (Figure 4.12E).

Indeed, at ca. 1350 CE, the large-scale climate reorganization associated with the Little Ice Age (LIA) brought colder temperatures and water in the North Atlantic (Mann, Zhang, et al., 2009). This is evident from the negative AMV index in Figure 4.12D, which indicates cooler than average SSTs over the North Atlantic (Mann, Zhang, et al., 2009). Cooler AMDR SSTs during the LIA should have halted cyclogenesis of intense storms in the North Atlantic and promoted quiescent storm conditions, just as the records from the Caribbean show (Donnelly et al., 2015; Lane et al., 2011; Yang et al., 2020), but our record, as well as other records from the North American east coast (Boldt et al., 2010; Donnelly et al., 2015; Oliva et al., 2018; van Hengstum et al., 2014) show the opposite. This therefore suggests that there is another forcing mechanism, perhaps unrelated to SSTs variations, responsible for an increase in storm activity in the North Atlantic and at the Magdalen Island during the LIA. For example, Donnelly et al. (Donnelly et al., 2015) points out that, at higher latitudes, hurricanes often develop through extratropical transition, suggesting that a colder climate in the northern latitudes may lead to larger baroclinicity in the North Atlantic, especially on the northeast coast, thus favoring the extratropical transitions of tropical cyclones. Another hypothesis could be that the cyclogenesis location shifted in the western North Atlantic along the eastern coast of the United States as a result of regional change in ocean conditions, thus favoring the genesis of cyclone that tracks mostly towards the east coast (Donnelly et al., 2015). Considering these findings, it appears that the more recent increase in storm activity, visible at TAC from ca. 1925 CE to the present, was probably not caused by the same climate factors related to the 1400-1650 CE increase.

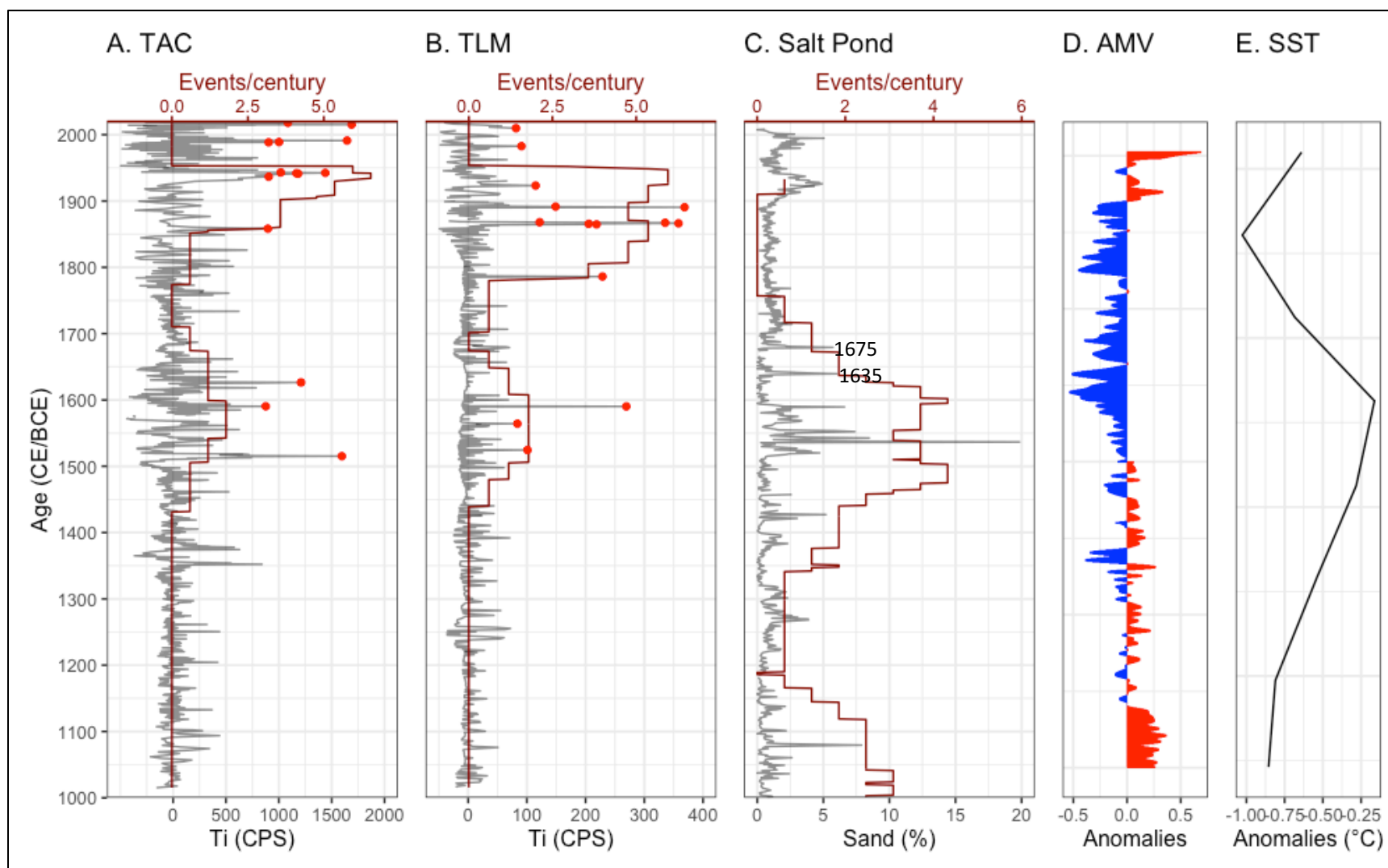


**Figure 4.12** Comparison of our two Magdalen Islands storm (Ti CPS) records to previously published research (C. Salt Pond, Massachusetts, storm records from Donnelly et al. (2015); D. Atlantic Multidecadal Variability (AMV) record from Mann, Zhang, et al. (2009); and E. North Atlantic SST anomalies from Orme et al. (2021)).

## 4.5 Conclusion

Our study is the first paleo-storm reconstruction from a peat core in North America, as well as the most northerly paleo-storm reconstruction focusing on tropical cyclone in North America. As such, it provides important insights about the potential of ombrotrophic peatlands for paleo-storm studies in the western North Atlantic and the climatic factors controlling storm variability in the GSL region. We show that it is possible to reconstruct paleo-storms from a peat core in a region affected by hurricanes, but also that it is of the utmost important to understand the peatland's own evolution and relationship with the climate. Peat being a live environment, particular attention should be given to developing a precise age-depth model that considers the various accumulation rates found in a peat core. We demonstrate that  $Ti$  is a useful proxy in paleotempestology, especially used in combination with the ASI. Our paleo-storm reconstruction is consistent with other reconstructions from the North Atlantic and shows that the 1450-1600 CE active storm period documented elsewhere was also persistent in the GSL. Our results also highlight the complexity of the relationship between the climate and storms. SST (examined through the AMV index), which is known to be related to storms at least during the instrumental (1850-present) period, is not related to the 1450-1650 active period and, therefore, the more recent increase in storm activity was probably not caused by the same climate factors related to the 1400-1650 CE increase. Ultimately, our study indicates that it is possible, in the GSL, to have period of heightened storm activity under two very different climatic regimes.

Anthropogenic climate change is likely to determine future storm trends (Colbert et al., 2013), potentially exposing coastal communities in eastern Canada to more extreme weather events. Studying intervals during the Holocene with intense storm activity is important for evaluating future storm risks. Future paleotempestological studies in eastern Canada should pay particular attention at the influence of large-scale climatic mode, such as the AMV, on storm activity, as this information is critical to understand future change in storm activity in eastern Canada.

## **CHAPTER 5: General conclusions and future directions**

This thesis aimed to review paleo-storm research along the margin of the Northeast Atlantic Ocean and to understand the relevance and significance of paleo-storm records in Eastern Canada, while contributing to paleotempestology by presenting a new paleo-storm record from the Magdalen Islands, in the Gulf of St. Lawrence. In Chapter 2, we showed that paleo-storms records from the northeastern US/Eastern Canada are underrepresented in the paleotempestological research of the North Atlantic Ocean and that the paleo-storm records from that region are on average covering a shorter period than records from other regions. Additionally, paleo-storm records based on wind-related proxies are almost absent from North American/Caribbean records, whereas most European (especially northern European) records are wind-based. It therefore appeared necessary to produce a wind-based paleo-storms record from eastern Canada, as such a record would help us deepening our understanding of long-term trends in TCs along the northern margin of the hurricane track, would facilitate the comparison of paleo-storms records from Europe and North America and, consequently, would help developing a general understanding of storminess across the whole North Atlantic Ocean. The literature review helped define our objectives for the research paper, which were to make a high-resolution paleoclimate reconstruction focusing on storms and to establish the potential of ombrotrophic peatlands for wind-based paleostorm studies in eastern North America. Our results are promising for future paleotempestological research in eastern Canada. Our high-resolution 1000 years reconstruction is one of the most northernmost paleo-storms record focusing on tropical cyclones in the North Atlantic and provides context and perspective on Holocene storm activity. In the past decades, researchers have slowly assembled the pieces of the complex puzzle of long-term storm variations; now, we know that we can also study peat cores from eastern Canada to complete the picture.

Our results provide directions for future research. First, it would be useful to understand in greater details the mechanisms of sediment transport and delivery into ombrotrophic peatlands during storm events. For example, setting up sediment traps in multiple places across the surface of a peatland would help us understand spatial variation in the deposition of sediments during storms, and such information would eventually provide a strong basis when choosing a coring site. The analysis of sediment traps data would also provide site-specific information on the relationship between the storm track position, the intensity of the storm, and sediment delivery, which would

improve the interpretation of sediment deposits. Second, developing longer records of paleo-storms in eastern Canada (> 4000 years) would increase both the temporal coverage and the spatial density of coverage in areas on the margins of the hurricane track. It is important to look at past periods of intense storm activity as analogs for future storm risks (Donnelly et al., 2015), but also to evaluate long-term trend such as the poleward migration of the hurricane track. Third, as Oliva et al. (2017) suggest, with an increasing number of paleo-storms record being produced in the North Atlantic, it is time now to start a more systematic analysis of regional storm trends. For example, studying the cause and context of the increase in storms during the Little Ice Age (1450-1650 CE) on the northeastern coast of North America would expand our understanding of the relationship between the climate and storms. We also argue that it is time to start integrating paleo-storms records from North America and Europe. Some studies proposed models to describe long-term storm trends on the North American east coast (Donnelly et al., 2015; Mann, Woodruff, et al., 2009; McCloskey & Liu, 2012; Yang et al., 2020) and in Europe (Orme et al., 2017; Orme, Reinhardt, Jones, Charman, Barkwith, et al., 2016), but none so far focused on integrating both regions. It would interesting, for example, to study the relationship between North American TCs and European ETCs through the lens of extratropical transition. Finally, the justification for reconstructing past storms is often to inform future storm; it would therefore be relevant now to identify mechanisms to systematically include paleo-storm records into climate change adaption policies, for example by calculating storm return periods.

## References

- Adomat, F., & Gischler, E. (2017). Assessing the suitability of Holocene environments along the central Belize coast, Central America, for the reconstruction of hurricane records. *International Journal of Earth Sciences*, 106(1), 283-309.
- Anderson, R. S., Sørensen, M., & Willetts, B. B. (1991). *A review of recent progress in our understanding of aeolian sediment transport*. Paper presented at the Aeolian Grain Transport 1, Vienna.
- Aquino-López, M. A., Blaauw, M., Christen, J. A., & Sanderson, N. K. (2018). Bayesian Analysis of 210-Pb Dating. *Journal of Agricultural, Biological and Environmental Statistics*, 23(3), 317-333.
- Arias, P., Bellouin, N., Coppola, E., Jones, R., Krinner, G., Marotzke, J., . . . Rogelj, J. (2021). Technical Summary. In *Climate Change 2021: The Physical Science Basis. Contribution of Working Group I to the Sixth Assessment Report of the Intergovernmental Panel on Climate Change*: Cambridge University Press, Cambridge, United Kingdom and New York, NY, USA.
- Aryal, Y. N., Villarini, G., Zhang, W., & Vecchi, G. A. (2018). Long term changes in flooding and heavy rainfall associated with North Atlantic tropical cyclones: Roles of the North Atlantic Oscillation and El Niño-Southern Oscillation. *Journal of hydrology*, 559, 698-710.
- Baldini, L. M., Baldini, J. U., McElwaine, J. N., Frappier, A. B., Asmerom, Y., Liu, K.-b., . . . Kennett, D. J. (2016). Persistent northward North Atlantic tropical cyclone track migration over the past five centuries. *Scientific Reports*, 6, 37522.
- Barnett, R. L., Bernatchez, P., Garneau, M., & Juneau, M. N. (2017). Reconstructing late Holocene relative sea-level changes at the Magdalen Islands (Gulf of St. Lawrence, Canada) using multi-proxy analyses. *Journal of Quaternary Science*, 32(3), 380-395.
- Bernatchez, P., Boucher-Brossard, G., & Sigouin-Cantin, M. (2012). Contribution des archives à l'étude des événements météorologiques et géomorphologiques causant des dommages aux côtes du Québec maritime et analyse des tendances, des fréquences et des temps de retour des conditions météo-marines extrêmes. *Rapport remis au ministère de la Sécurité publique du Québec. Chaire de recherche en géoscience côtière, Laboratoire de dynamique et de gestion intégrée des zones côtières, Université du Québec à Rimouski*, 140 p.
- Bernatchez, P., Drejza, S., & Dugas, S. (2012). Marges de sécurité en érosion côtière: évolution historique et future du littoral des îles de la Madeleine. *Laboratoire de dynamique et de gestion intégrée des zones côtières, Université du Québec à Rimouski. Rapport remis au ministère de la Sécurité publique du Québec*, 71 p.
- Bernatchez, P., Fraser, C., Friesinger, S., Jolivet, Y., Dugas, S., Drejza, S., & Morissette, A. (2008). Sensibilité des côtes et vulnérabilité des communautés du golfe du Saint-Laurent aux impacts des changements climatiques. *Laboratoire de dynamique et de gestion intégrée des zones côtières, Université du Québec à Rimouski. Rapport de recherche remis au Consortium OURANOS et au FACC*, 256 p.

- Bhatia, K. T., Vecchi, G. A., Knutson, T. R., Murakami, H., Kossin, J., Dixon, K. W., & Whitlock, C. E. (2019). Recent increases in tropical cyclone intensification rates. *Nature communications*, *10*(1), 1-9.
- Birks, H. J. B., & Birks, H. H. (1980). *Quaternary palaeoecology*: Edward Arnold: London.
- Björckl, S., & Clemmensen, L. B. (2004). Aeolian sediment in raised bog deposits, Halland, SW Sweden: a new proxy record of Holocene winter storminess variation in southern Scandinavia? *The Holocene*, *14*(5), 677-688.
- Blaauw, M., Christen, J., Aquino, M., Vazquez, J., Gonzalez, O., Belding, T., & Karney, C. (2022). rbacon: Age-Depth Modelling Using Bayesian Statistics. Retrieved from <https://cran.r-project.org/web/packages/rbacon/rbacon.pdf>
- Blaauw, M., Christen, J., & Aquino-Lopez, M. (2021). rplum: Bayesian Age-Depth Modelling of Cores Dated by Pb-210. R package version 0.2. 2. Retrieved from <https://cran.r-project.org/web/packages/rplum/rplum.pdf>
- Blaauw, M., & Christen, J. A. (2011). Flexible paleoclimate age-depth models using an autoregressive gamma process. *Bayesian analysis*, *6*(3), 457-474.
- Boldt, K. V., Lane, P., Woodruff, J. D., & Donnelly, J. P. (2010). Calibrating a sedimentary record of overwash from Southeastern New England using modeled historic hurricane surges. *Marine Geology*, *275*(1-4), 127-139.
- Brown, A. L., Reinhardt, E. G., van Hengstum, P. J., & Pilarczyk, J. E. (2014). A coastal Yucatan sinkhole records intense hurricane events. *Journal of Coastal Research*, *30*(2), 418-428.
- Buynevich, I. V., FitzGerald, D. M., & Goble, R. J. (2007). A 1500 yr record of North Atlantic storm activity based on optically dated relict beach scarps. *Geology*, *35*(6), 543-546.
- Camargo, A. (2022). PCAtest: testing the statistical significance of Principal Component Analysis in R. *PeerJ*, *10*, e12967.
- Canadian Hurricane Center. (2014). 2014 Tropical Cyclone Season Summary. Retrieved from [https://publications.gc.ca/collections/collection\\_2015/ec/En55-8-2014-eng.pdf](https://publications.gc.ca/collections/collection_2015/ec/En55-8-2014-eng.pdf)
- Castagno, K. A., Donnelly, J. P., & Woodruff, J. D. (2021). Grain-Size Analysis of Hurricane-Induced Event Beds in a New England Salt Marsh, Massachusetts, USA. *Journal of Coastal Research*, *37*(2), 326-335.
- Chaumillon, E., Bertin, X., Fortunato, A. B., Bajo, M., Schneider, J.-L., Dezileau, L., . . . Créach, A. (2017). Storm-induced marine flooding: Lessons from a multidisciplinary approach. *Earth-Science Reviews*, *165*, 151-184.
- Chawchai, S., Kylander, M. E., Chabangborn, A., Löwemark, L., & Wohlfarth, B. (2016). Testing commonly used X-ray fluorescence core scanning-based proxies for organic-rich lake sediments and peat. *Boreas*, *45*(1), 180-189.
- Cohen, J., Screen, J. A., Furtado, J. C., Barlow, M., Whittleston, D., Coumou, D., . . . Overland, J. (2014). Recent Arctic amplification and extreme mid-latitude weather. *Nature geoscience*, *7*(9), 627-637.

- Colbert, A. J., Soden, B. J., Vecchi, G. A., & Kirtman, B. P. (2013). The impact of anthropogenic climate change on North Atlantic tropical cyclone tracks. *Journal of climate*, 26(12), 4088-4095.
- Crann, C. A., Murseli, S., St-Jean, G., Zhao, X., Clark, I. D., & Kieser, W. E. (2017). First status report on radiocarbon sample preparation techniques at the AE Lalonde AMS Laboratory (Ottawa, Canada). *Radiocarbon*, 59(3), 695-704.
- Croudace, I. W., & Rothwell, R. G. (2015). *Micro-XRF Studies of Sediment Cores: Applications of a non-destructive tool for the environmental sciences* (Vol. 17): Springer.
- Dalton, A. S., Margold, M., Stokes, C. R., Tarasov, L., Dyke, A. S., Adams, R. S., . . . Attig, J. W. (2020). An updated radiocarbon-based ice margin chronology for the last deglaciation of the North American Ice Sheet Complex. *Quaternary Science Reviews*, 234, 106223.
- Danard, M., Munro, A., & Murty, T. (2003). Storm surge hazard in Canada. *Natural Hazards*, 28(2-3), 407-434.
- De Vleeschouwer, F., Sikorski, J., & Fagel, N. (2010). Development of lead-210 measurement in peat using polonium extraction. A procedural comparison. *Geochronometria*, 36, 1-8.
- Delgado-Fernandez, I., & Davidson-Arnott, R. (2011). Meso-scale aeolian sediment input to coastal dunes: The nature of aeolian transport events. *Geomorphology*, 126(1-2), 217-232.
- DeVries-Zimmerman, S., Fisher, T. G., Hansen, E. C., Dean, S., & Björck, S. (2014). Sand in lakes and bogs in Allegan County, Michigan, as a proxy for eolian sand transport. *Geological Society of America Special Papers*, 508, 111-131.
- Donnelly, J. P., Bryant, S. S., Butler, J., Dowling, J., Fan, L., Hausmann, N., . . . Westover, K. (2001). 700 yr sedimentary record of intense hurricane landfalls in southern New England. *Geological Society of America Bulletin*, 113(6), 714-727.
- Donnelly, J. P., Hawkes, A. D., Lane, P., MacDonald, D., Shuman, B. N., Toomey, M. R., . . . Woodruff, J. D. (2015). Climate forcing of unprecedented intense-hurricane activity in the last 2000 years. *Earth's Future*, 3(2), 49-65.
- Donnelly, J. P., Roll, S., Wengren, M., Butler, J., Lederer, R., & Webb, T. (2001). Sedimentary evidence of intense hurricane strikes from New Jersey. *Geology*, 29(7), 615-618.
- Donnelly, J. P., & Woodruff, J. D. (2007). Intense hurricane activity over the past 5,000 years controlled by El Niño and the West African monsoon. *Nature*, 447(7143), 465-468.
- Emmanouilidis, A., Messaris, G., Ntzanis, E., Zampakis, P., Prevedouros, I., Bassukas, D. A., & Avramidis, P. (2020). CT scanning, X-ray fluorescence: Non-destructive techniques for the identification of sedimentary facies and structures. *Revue de Micropaléontologie*, 67, 100410.
- Engelhart, S. E., Pilarczyk, J., & Rovere, A. (2019). storms and extreme events: insights from the historical and paleo record. *Past Global Change*, 27, 2017-2018.
- Environment and Climate Change Canada. (1988). Résumé de la saison des cyclones tropicaux au Canada en 1988. Retrieved from <https://www.ec.gc.ca/ouragans-hurricanes/default.asp?lang=fr&n=71F87DE9-1>

- Environment and Climate Change Canada. (1992). Résumé de la saison des cyclones tropicaux au Canada en 1991. Retrieved from <https://www.ec.gc.ca/ouragans-hurricanes/default.asp?lang=fr&n=9D24F0EE-1>
- Environment and Climate Change Canada. (2020). Historical Data. Retrieved from [https://climate.weather.gc.ca/historical\\_data/search\\_historic\\_data\\_e.html](https://climate.weather.gc.ca/historical_data/search_historic_data_e.html)
- Ezer, T. (2020). The long-term and far-reaching impact of hurricane Dorian (2019) on the Gulf Stream and the coast. *Journal of Marine Systems*, 208. doi:10.1016/j.jmarsys.2020.103370
- Feser, F., Barcikowska, M., Krueger, O., Schenk, F., Weisse, R., & Xia, L. (2015). Storminess over the North Atlantic and northwestern Europe—A review. *Quarterly Journal of the Royal Meteorological Society*, 141(687), 350-382.
- Forbes, D. L., Parkes, G. S., Manson, G. K., & Ketch, L. A. (2004). Storms and shoreline retreat in the southern Gulf of St. Lawrence. *Marine Geology*, 210(1-4), 169-204.
- Fortin, J.-C. (2003). *Histoire des Iles-de-la-Madeleine*. Sainte-Foy: Institut quebécois de recherche sur la culture.
- Frajka-Williams, E., Beaulieu, C., & Duchez, A. (2017). Emerging negative Atlantic Multidecadal Oscillation index in spite of warm subtropics. *Scientific Reports*, 7(1), 1-8.
- Francis, J. A., & Vavrus, S. J. (2012). Evidence linking Arctic amplification to extreme weather in mid-latitudes. *Geophysical research letters*, 39(6).
- Frappier, A. B., Pyburn, J., Pinkey-Drobnis, A. D., Wang, X., Corbett, D. R., & Dahlin, B. H. (2014). Two millennia of tropical cyclone-induced mud layers in a northern Yucatán stalagmite: Multiple overlapping climatic hazards during the Maya Terminal Classic “megadroughts”. *Geophysical research letters*, 41(14), 5148-5157.
- Frappier, A. B., Sahagian, D., Carpenter, S. J., González, L. A., & Frappier, B. R. (2007). Stalagmite stable isotope record of recent tropical cyclone events. *Geology*, 35(2), 111-114.
- Garneau, M. (1995). Collection de référence de graines et autres macrofossiles végétaux de taxons provenant du Québec méridional et boréal et de l'arctique canadien. *Geological Survey of Canada, Division de la science des terrains, Sainte-Foy*, 47 p.
- Gischler, E., Shinn, E. A., Oschmann, W., Fiebig, J., & Buster, N. A. (2008). A 1500-year Holocene Caribbean climate archive from the Blue Hole, Lighthouse reef, Belize. *Journal of Coastal Research*, 24(6 (246)), 1495-1505.
- Glaser, P. H., & Janssens, J. A. (1986). Raised bogs in eastern North America: transitions in landforms and gross stratigraphy. *Canadian Journal of Botany*, 64(2), 395-415. doi:10.1139/b86-056
- Goslin, J., & Clemmensen, L. B. (2017). Proxy records of Holocene storm events in coastal barrier systems: Storm-wave induced markers. *Quaternary Science Reviews*, 174, 80-119.
- Goslin, J., Fruergaard, M., Sander, L., Gałka, M., Menviel, L., Monkenbusch, J., . . . Clemmensen, L. B. (2018). Holocene centennial to millennial shifts in North-Atlantic storminess and ocean dynamics. *Scientific Reports*, 8(1), 1-12.

- Goslin, J., Gałka, M., Sander, L., Fruergaard, M., Mokenbusch, J., Thibault, N., & Clemmensen, L. B. (2019). Decadal variability of north-eastern Atlantic storminess at the mid-Holocene: New inferences from a record of wind-blown sand, western Denmark. *Global and Planetary Change*, *180*, 16-32.
- Gustafsson, M. E., & Franzén, L. G. (2000). Inland transport of marine aerosols in southern Sweden. *Atmospheric Environment*, *34*(2), 313-325.
- Hart, R. E., & Evans, J. L. (2001). A climatology of the extratropical transition of Atlantic tropical cyclones. *Journal of climate*, *14*(4), 546-564.
- Heiri, O., Lotter, A. F., & Lemcke, G. (2001). Loss on ignition as a method for estimating organic and carbonate content in sediments: reproducibility and comparability of results. *Journal of Paleolimnology*, *25*(1), 101-110.
- Hétu, B., Rémillard, A. M., Bernatchez, P., & St-Onge, G. (2020). Landforms and Landscapes of the Magdalen Islands: The Role of Geology and Climate. In *Landscapes and Landforms of Eastern Canada* (pp. 431-451): Springer.
- Hewett, D. (1964). *Menyanthes trifoliata* L. *Journal of Ecology*, *52*(3), 723-735.
- Hippensteel, S. P. (2010). Paleotempestology and the pursuit of the perfect paleostorm proxy. *GSA Today*, *20*(4), 52-53.
- Howie, R., Zussman, J., & Deer, W. (1992). *An introduction to the rock-forming minerals*: Longman London, UK.
- Husson, F., Julie, J., Le, S., & Mazet, J. (2016). FactoMineR: multivariate exploratory data analysis and data mining. Retrieved from <https://cran.r-project.org/web/packages/FactoMineR/FactoMineR.pdf>
- Ingram, H. (1978). Soil layers in mires: function and terminology *Journal of Soil Science*, *29*(2), 224-227. doi:10.1111/j.1365-2389.1978.tb02053.x
- Insurance Bureau of Canada. (2022). Hurricane Fiona causes \$660 million in insured damage. Retrieved from <http://www.IBC.ca/ns/resources/media-centre/media-releases/hurricane-fiona-causes-660-million-in-insured-damage>
- Jardine, D. E., Wang, X., & Fenech, A. L. (2021). Highwater mark collection after post tropical storm Dorian and implications for Prince Edward Island, Canada. *Water*, *13*(22), 3201.
- John Cangialosi, R. B. (Producer). (2012). Hurricane life cycle and hazards. [PowerPoint slides] Retrieved from [https://www.nhc.noaa.gov/outreach/presentations/2012\\_02nhcL311\\_hurricaneLifeCycleHazards.pdf](https://www.nhc.noaa.gov/outreach/presentations/2012_02nhcL311_hurricaneLifeCycleHazards.pdf)
- Joly, A. (2015). Synoptic Meteorology: Extratropical Cyclones. In *Encyclopedia of Atmospheric Sciences: Second Edition* (pp. 304-336): Elsevier.
- Juggins, S. (2022). rioja: Analysis of Quaternary Science Data. Retrieved from <https://cran.r-project.org/web/packages/rioja/rioja.pdf>
- Kern, O. A., Koutsodendris, A., Maechtle, B., Christanis, K., Schukraft, G., Scholz, C., . . . Pross, J. (2019). XRF core scanning yields reliable semiquantitative data on the elemental

- composition of highly organic-rich sediments: Evidence from the Füramoos peat bog (Southern Germany). *Science of the Total Environment*, 697, 134110.
- Kilbourne, K. H., Moyer, R. P., Quinn, T. M., & Grottoli, A. G. (2011). Testing coral-based tropical cyclone reconstructions: An example from Puerto Rico. *Palaeogeography, Palaeoclimatology, Palaeoecology*, 307(1-4), 90-97.
- Klotzbach, P. J., Bowen, S. G., Pielke, R., & Bell, M. (2018). Continental US hurricane landfall frequency and associated damage: Observations and future risks. *Bulletin of the American Meteorological Society*, 99(7), 1359-1376.
- Klotzbach, P. J., Gray, W., & Fogarty, C. (2015). Active Atlantic hurricane era at its end? *Nature geoscience*, 8(10), 737-738.
- Klotzbach, P. J., Wood, K. M., Schreck III, C. J., Bowen, S. G., Patricola, C. M., & Bell, M. M. (2022). Trends in Global Tropical Cyclone Activity: 1990–2021. *Geophysical research letters*, e2021GL095774.
- Knapp, K. R., Kruk, M. C., Levinson, D. H., Diamond, H. J., & Neumann, C. J. (2010). The international best track archive for climate stewardship (IBTrACS) unifying tropical cyclone data. *Bulletin of the American Meteorological Society*, 91(3), 363-376.
- Knutson, T., Camargo, S. J., Chan, J. C., Emanuel, K., Ho, C.-H., Kossin, J., . . . Walsh, K. (2019). Tropical cyclones and climate change assessment: Part I: Detection and attribution. *Bulletin of the American Meteorological Society*, 100(10), 1987-2007.
- Knutson, T., Camargo, S. J., Chan, J. C., Emanuel, K., Ho, C.-H., Kossin, J., . . . Walsh, K. (2020). Tropical cyclones and climate change assessment: Part II: Projected response to anthropogenic warming. *Bulletin of the American Meteorological Society*, 101(3), E303-E322.
- Knutson, T., McBride, J. L., Chan, J., Emanuel, K., Holland, G., Landsea, C., . . . Sugi, M. (2010). Tropical cyclones and climate change. *Nature geoscience*, 3(3), 157-163.
- Kossin, J. P., Emanuel, K. A., & Vecchi, G. A. (2014). The poleward migration of the location of tropical cyclone maximum intensity. *Nature*, 509(7500), 349-352.
- Kuhry, P., & Turunen, J. (2006). The postglacial development of boreal and subarctic peatlands. In *Boreal peatland ecosystems* (pp. 25-46): Springer.
- Kylander, M. E., Ampel, L., Wohlfarth, B., & Veres, D. (2011). High-resolution X-ray fluorescence core scanning analysis of Les Echets (France) sedimentary sequence: new insights from chemical proxies. *Journal of Quaternary Science*, 26(1), 109-117.
- Kylander, M. E., Söderlindh, J., Schenk, F., Gyllencreutz, R., Rydberg, J., Bindler, R., . . . Skelton, A. (2020). It's in your glass: a history of sea level and storminess from the Laphroaig bog, Islay (southwestern Scotland). *Boreas*, 49(1), 152-167.
- Landry, F. (1989). *Derniere Course: Aventures maritimes dans le Golfe du Saint-Laurent*. Havre-Aubert, Ile-de-la-Madeleine: La Boussole.
- Landry, F. (1994). *Piege de sable*. Havre-Aubert, Iles-de-la-Madeleine: La Boussole.

- Lane, C. S., Hildebrandt, B., Kennedy, L. M., LeBlanc, A., Liu, K.-B., Wagner, A. J., & Hawkes, A. D. (2017). Verification of tropical cyclone deposits with oxygen isotope analyses of coeval ostracod valves. *Journal of Paleolimnology*, 57(3), 245-255.
- Lane, P., Donnelly, J. P., Woodruff, J. D., & Hawkes, A. D. (2011). A decadal-resolved paleohurricane record archived in the late Holocene sediments of a Florida sinkhole. *Marine Geology*, 287(1-4), 14-30.
- Lases-Hernández, F., Medina-Elizalde, M., & Frappier, A. B. (2020). Drip water  $\delta^{18}\text{O}$  variability in the northeastern Yucatán Peninsula, Mexico: Implications for tropical cyclone detection and rainfall reconstruction from speleothems. *Geochimica et Cosmochimica Acta*, 285, 237-256.
- Lekshmy, P., Midhun, M., Ramesh, R., & Jani, R. (2014).  $^{18}\text{O}$  depletion in monsoon rain relates to large scale organized convection rather than the amount of rainfall. *Scientific Reports*, 4(1), 1-5.
- Leps, J., & Smilauer, P. (2003). *Multivariate analysis of ecological data using CANOCO*: Cambridge University Press, Cambridge, United Kingdom and New York, NY, USA.
- Li, Z.-H., Labbé, N., Driese, S. G., & Grissino-Mayer, H. D. (2011). Micro-scale analysis of tree-ring  $\delta^{18}\text{O}$  and  $\delta^{13}\text{C}$  on  $\alpha$ -cellulose spline reveals high-resolution intra-annual climate variability and tropical cyclone activity. *Chemical Geology*, 284(1-2), 138-147.
- Longman, J., Veres, D., & Wennrich, V. (2019). Utilisation of XRF core scanning on peat and other highly organic sediments. *Quaternary International*, 514, 85-96.
- Magnan, G., & Garnau, M. (2014). Evaluating long-term regional climate variability in the maritime region of the St. Lawrence North Shore (eastern Canada) using a multi-site comparison of peat-based paleohydrological records. *Journal of Quaternary Science*, 29(3), 209-220.
- Magnan, G., Garneau, M., & Payette, S. (2014). Holocene development of maritime ombrotrophic peatlands of the St. Lawrence North Shore in eastern Canada. *Quaternary Research*, 82(1), 96-106.
- Mann, M. E., Woodruff, J. D., Donnelly, J. P., & Zhang, Z. (2009). Atlantic hurricanes and climate over the past 1,500 years. *Nature*, 460(7257), 880-883.
- Mann, M. E., Zhang, Z., Rutherford, S., Bradley, R. S., Hughes, M. K., Shindell, D., . . . Ni, F. (2009). Global signatures and dynamical origins of the Little Ice Age and Medieval Climate Anomaly. *science*, 326(5957), 1256-1260.
- Marks, F. D. (2015). Tropical Cyclones and Hurricanes: Hurricanes: Observation. In *Encyclopedia of Atmospheric Sciences: Second Edition* (pp. 35-56): Elsevier.
- Masselink, G., & van Heteren, S. (2014). Response of wave-dominated and mixed-energy barriers to storms. *Marine Geology*, 352, 321-347.
- Masson, A. (2014). The extratropical transition of Hurricane Igor and the impacts on Newfoundland. *Natural Hazards*, 72(2), 617-632. doi:10.1007/s11069-013-1027-x
- McCloskey, T. A., & Liu, K.-b. (2012). A sedimentary-based history of hurricane strikes on the southern Caribbean coast of Nicaragua. *Quaternary Research*, 78(3), 454-464.

- McCloskey, T. A., & Liu, K.-b. (2013). A 7000 year record of paleohurricane activity from a coastal wetland in Belize. *The Holocene*, 23(2), 278-291.
- McIlveen, R. (2010). *Fundamentals of Weather and Climate (Second edition)*: Oxford University Press.
- McTaggart-Cowan, R., Atallah, E. H., Gyakum, J. R., & Bosart, L. F. (2006). Hurricane Juan (2003). Part I: A diagnostic and compositing life cycle study. *Monthly Weather Review*, 134(7), 1725-1747. doi:10.1175/MWR3142.1
- Ministère de l'Environnement et de la Lutte contre les changements climatiques. (2021a). Habitat floristique de la Tourbière-de-L'Anse-à-la-Cabane. Retrieved from <https://www.environnement.gouv.qc.ca/biodiversite/habitats/tourbiere-anse-cabane/index.htm>
- Ministère de l'Environnement et de la Lutte contre les changements climatiques. (2021b). Habitat floristique de la Tourbière-du-Lac-Maucôque. Retrieved from <https://www.environnement.gouv.qc.ca/biodiversite/habitats/tourbiere-lac-maucoque/index.htm>
- Moreno, J., Fatela, F., Leorri, E., Moreno, F., Freitas, M., Valente, T., . . . Blake, W. (2017). Bromine soil/sediment enrichment in tidal salt marshes as a potential indicator of climate changes driven by solar activity: New insights from W coast Portuguese estuaries. *Science of the Total Environment*, 580, 324-338.
- Moskalewicz, D., Szczuciński, W., Mroczek, P., & Vaikutienė, G. (2020). Sedimentary record of historical extreme storm surges on the Gulf of Gdańsk coast, Baltic Sea. *Marine Geology*, 420, 106084.
- Myrhaug, D. (2017). Wave-induced bottom shear stress estimation in shallow water exemplified by using deep water wind statistics. *Oceanologia*, 59(2), 102-107.
- Neumann, B., Vafeidis, A. T., Zimmermann, J., & Nicholls, R. J. (2015). Future coastal population growth and exposure to sea-level rise and coastal flooding-a global assessment. *PloS one*, 10(3), e0118571.
- Nielsen, P. R., Dahl, S. O., & Jansen, H. L. (2016). Mid-to late Holocene aeolian activity recorded in a coastal dunefield and lacustrine sediments on Andøya, northern Norway. *The Holocene*, 26(9), 1486-1501.
- Nikitina, D. L., Kemp, A. C., Horton, B. P., Vane, C. H., van de Plassche, O., & Engelhart, S. E. (2014). Storm erosion during the past 2000 years along the north shore of Delaware Bay, USA. *Geomorphology*, 208, 160-172.
- Oliva, F., Peros, M., & Viau, A. (2017). A review of the spatial distribution of and analytical techniques used in paleotempestological studies in the western North Atlantic Basin. *Progress in Physical Geography*, 41(2), 171-190.
- Oliva, F., Peros, M., Viau, A., Reinhardt, E., Nixon, F., & Morin, A. (2018). A multi-proxy reconstruction of tropical cyclone variability during the past 800 years from Robinson Lake, Nova Scotia, Canada. *Marine Geology*, 406, 84-97.

- Orme, L. C., Charman, D. J., Reinhardt, L., Jones, R. T., Mitchell, F. J., Stefanini, B. S., . . . Grosvenor, M. (2017). Past changes in the North Atlantic storm track driven by insolation and sea-ice forcing. *Geology*, *45*(4), 335-338.
- Orme, L. C., Davies, S., & Duller, G. (2015). Reconstructed centennial variability of late Holocene storminess from Cors Fochno, Wales, UK. *Journal of Quaternary Science*, *30*(5), 478-488.
- Orme, L. C., Miettinen, A., Seidenkrantz, M.-S., Tuominen, K., Pearce, C., Divine, D. V., . . . Kuijpers, A. (2021). Mid to late-Holocene sea-surface temperature variability off north-eastern Newfoundland and its linkage to the North Atlantic Oscillation. *The Holocene*, *31*(1), 3-15.
- Orme, L. C., Reinhardt, L., Jones, R. T., Charman, D. J., Barkwith, A., & Ellis, M. A. (2016). Aeolian sediment reconstructions from the Scottish Outer Hebrides: Late Holocene storminess and the role of the North Atlantic Oscillation. *Quaternary Science Reviews*, *132*, 15-25.
- Orme, L. C., Reinhardt, L., Jones, R. T., Charman, D. J., Croudace, I., Dawson, A., . . . Barkwith, A. (2016b). Investigating the maximum resolution of  $\mu$ XRF core scanners: A 1800 year storminess reconstruction from the Outer Hebrides, Scotland, UK. *The Holocene*, *26*(2), 235-247.
- Parris, A. S., Bierman, P. R., Noren, A. J., Prins, M. A., & Lini, A. (2010). Holocene paleostorms identified by particle size signatures in lake sediments from the northeastern United States. *Journal of Paleolimnology*, *43*(1), 29-49. Retrieved from <https://www.scopus.com/inward/record.uri?eid=2-s2.0-77949775181&doi=10.1007%2fs10933-009-9311-1&partnerID=40&md5=90cbf4f482254e4ffb0d9a64f5801ac8>
- <https://link.springer.com/article/10.1007/s10933-009-9311-1>
- Payette, S., & Rochefort, L. (2001). *Écologie des tourbières du Québec-Labrador*: Presses Université Laval.
- Peros, M., Chan, K., Magnan, G., Ponsford, L., Carroll, J., & McCloskey, T. (2016). A 9600-year record of water table depth, vegetation and fire inferred from a raised peat bog, Prince Edward Island, Canadian Maritimes HOLOCENE CLIMATE FROM PRINCE EDWARD ISLAND, CANADA. *Journal of Quaternary Science*, *31*(5), 512-525. doi:10.1002/jqs.2875
- Perrier, L., Garneau, M., Pratte, S., & Sanderson, N. K. (2022). Climate-driven Holocene ecohydrological and carbon dynamics from maritime peatlands of the Gulf of St. Lawrence, eastern Canada. *The Holocene*, 09596836221095978.
- Plante, M., Son, S. W., Atallah, E., Gyakum, J., & Grise, K. (2015). Extratropical cyclone climatology across eastern Canada. *International Journal of Climatology*, *35*(10), 2759-2776.
- Pouzet, P., Maanan, M., Piotrowska, N., Baltzer, A., Stéphan, P., & Robin, M. (2018). Chronology of Holocene storm events along the European Atlantic coast: New data from the Island of Yeu, France. *Progress in Physical Geography: Earth and Environment*, *42*(4), 431-450.

- Pratte, S., Garneau, M., & De Vleeschouwer, F. (2017). Late-Holocene atmospheric dust deposition in eastern Canada (St. Lawrence North Shore). *The Holocene*, 27(1), 12-25.
- Pratte, S., Mucci, A., & Garneau, M. (2013). Historical records of atmospheric metal deposition along the St. Lawrence Valley (eastern Canada) based on peat bog cores. *Atmospheric Environment*, 79, 831-840.
- Public Safety Canada. (2022). *Canadian Disaster Database*. Retrieved from: <https://cdd.publicsafety.gc.ca/rslts-eng.aspx?cultureCode=en-Ca&provinces=11&eventTypes=%27EP%27%2c%27IN%27%2c%27PA%27%2c%27AV%27%2c%27CE%27%2c%27DR%27%2c%27FL%27%2c%27GS%27%2c%27HE%27%2c%27HU%27%2c%27SO%27%2c%27SS%27%2c%27ST%27%2c%27TO%27%2c%27WF%27%2c%27SW%27%2c%27EQ%27%2c%27LS%27%2c%27TS%27%2c%27VO%27&normalizedCostYear=1&dynamic=false>
- Raible, C. C., Pinto, J. G., Ludwig, P., & Messmer, M. (2021). A review of past changes in extratropical cyclones in the northern hemisphere and what can be learned for the future. *Wiley Interdisciplinary Reviews: Climate Change*, 12(1), e680.
- Reimer, P. J., Austin, W. E. N., Bard, E., Bayliss, A., Blackwell, P. G., Bronk Ramsey, C., . . . Talamo, S. (2020). The IntCal20 Northern Hemisphere Radiocarbon Age Calibration Curve (0–55 cal kBP). *Radiocarbon*, 62(4), 725-757. doi:10.1017/RDC.2020.41
- Rémillard, A. M., Buylaert, J.-P., Murray, A., St-Onge, G., Bernatchez, P., & Hétu, B. (2015). Quartz OSL dating of late Holocene beach ridges from the Magdalen Islands (Quebec, Canada). *Quaternary Geochronology*, 30, 264-269.
- Rémillard, A. M., St-Onge, G., Bernatchez, P., Hétu, B., Buylaert, J. P., Murray, A. S., & Vigneault, B. (2016). Chronology and stratigraphy of the Magdalen Islands archipelago from the last glaciation to the early Holocene: new insights into the glacial and sea-level history of eastern Canada. *Boreas*, 45(4), 604-628.
- Rodriguez, A. B., Theuerkauf, E. J., Ridge, J. T., VanDusen, B. M., & Fegley, S. R. (2020). Long-term washover fan accretion on a transgressive barrier island challenges the assumption that paleotempestites represent individual tropical cyclones. *Scientific Reports*, 10(1), 1-10.
- Rodriguez, A. B., Yu, W., & Theuerkauf, E. J. (2018). Abrupt increase in washover deposition along a transgressive barrier island during the late nineteenth century acceleration in sea-level rise. In *Barrier dynamics and response to changing climate* (pp. 121-145): Springer.
- Roy-Bolduc, A. (2010). *Portrait et historique d'utilisation de l'écosystème forestier des Îles-de-la-Madeleine rapport de stage en foresterie / Alice Roy-Bolduc*. Havre-aux-Maisons.
- Sabina, A. P. (2003). *Rocks and minerals for the collector: Iles de la Madeleine, Quebec, the Island of Newfoundland, and Labrador* (Vol. 58): Geological Survey of Canada.
- Sadler, P. M. (1981). Sediment accumulation rates and the completeness of stratigraphic sections. *The journal of geology*, 89(5), 569-584.
- Sauvé, A. (2016). Reconstitution holocène de la végétation et du climat pour les régions de Baie-Comeau et d'Havre-Saint-Pierre, Québec.

- Scheffers, A., Engel, M., Scheffers, S., Squire, P., & Kelletat, D. (2012). Beach ridge systems—archives for Holocene coastal events? *Progress in Physical Geography*, 36(1), 5-37.
- Scileppi, E., & Donnelly, J. P. (2007). Sedimentary evidence of hurricane strikes in western Long Island, New York. *Geochemistry, Geophysics, Geosystems*, 8(6).
- Shotyk, W. (1996). Peat bog archives of atmospheric metal deposition: geochemical evaluation of peat profiles, natural variations in metal concentrations, and metal enrichment factors. *Environmental Reviews*, 4(2), 149-183. doi:10.1139/a96-010
- Shotyk, W., Weiss, D., Kramers, J. D., Frei, R., Cheburkin, A. K., Gloor, M., & Reese, S. (2001). Geochemistry of the peat bog at Etang de la Gruère, Jura Mountains, Switzerland, and its record of atmospheric Pb and lithogenic trace metals (Sc, Ti, Y, Zr, and REE) since 12,370 14C yr BP. *Geochimica et Cosmochimica Acta*, 65(14), 2337-2360. doi:10.1016/S0016-7037(01)00586-5
- Steinmann, P., & Shotyk, W. (1997). Geochemistry, mineralogy, and geochemical mass balance on major elements in two peat bog profiles (Jura Mountains, Switzerland). *Chemical Geology*, 138(1), 25-53. doi:10.1016/S0009-2541(96)00171-4
- Stewart, H., Bradwell, T., Bullard, J., Davies, S., Golledge, N., & McCulloch, R. (2017). 8000 years of North Atlantic storminess reconstructed from a Scottish peat record: implications for Holocene atmospheric circulation patterns in Western Europe. *Journal of Quaternary Science*, 32(8), 1075-1084.
- Sun, C., Tian, L., Shanahan, T. M., Partin, J. W., Gao, Y., Piatrunia, N., & Banner, J. (2022). Isotopic variability in tropical cyclone precipitation is controlled by Rayleigh distillation and cloud microphysics. *Communications Earth & Environment*, 3(1), 1-10.
- Tamura, T. (2012). Beach ridges and prograded beach deposits as palaeoenvironment records. *Earth-Science Reviews*, 114(3-4), 279-297.
- Ting, M., Kossin, J. P., Camargo, S. J., & Li, C. (2019). Past and future hurricane intensity change along the US east coast. *Scientific Reports*, 9(1), 1-8.
- Toomey, M. R., Curry, W. B., Donnelly, J. P., & van Hengstum, P. J. (2013). Reconstructing 7000 years of North Atlantic hurricane variability using deep-sea sediment cores from the western Great Bahama Bank. *Paleoceanography*, 28(1), 31-41.
- Troels-Smith, J. (1955). *Characterization of unconsolidated sediments*: Reitzels Forlag.
- Vaasma, T. (2008). Grain-size analysis of lacustrine sediments: a comparison of pre-treatment methods. *Estonian Journal of Ecology*, 57(4).
- Vachula, R. S., Sheppard, R. Y., & Cheung, A. H. (2022). Preservation biases are pervasive in Holocene paleofire records. *Palaeogeography, Palaeoclimatology, Palaeoecology*, 602, 111165.
- van Hengstum, P. J., Donnelly, J. P., Fall, P. L., Toomey, M. R., Albury, N. A., & Kakuk, B. (2016). The intertropical convergence zone modulates intense hurricane strikes on the western North Atlantic margin. *Scientific Reports*, 6(1), 1-10.

- van Hengstum, P. J., Donnelly, J. P., Toomey, M. R., Albury, N. A., Lane, P., & Kakuk, B. (2014). Heightened hurricane activity on the Little Bahama Bank from 1350 to 1650 AD. *Continental Shelf Research*, *86*, 103-115.
- van Oldenborgh, G. J., te Raa, L. A., Dijkstra, H. A., & Philip, S. Y. (2009). Frequency-or amplitude-dependent effects of the Atlantic meridional overturning on the tropical Pacific Ocean. *Ocean science*, *5*(3), 293-301.
- Vandel, E., Vaasma, T., Sugita, S., Tõnisson, H., Jaagus, J., Vilumaa, K., . . . Kont, A. (2019). Reconstruction of past storminess: Evaluation of an indicator approach using aeolian mineral grains buried in peat deposits, Estonia. *Quaternary Science Reviews*, *218*, 215-227.
- Vasseur, L., Catto, N. R., Burton, D. L., Chouinard, O., Hermanutz, L., Jacobs, J., . . . Lacroix, J. (2007). Chapitre 4: Canada atlantique. *Vivre avec les changements climatiques au Canada. DS Lemmen, Warren, FJ, J, L. and E, B. Ottawa, ON, Gouvernement du Canada. édition, 448.*
- Vecchi, G. A., Delworth, T. L., & Booth, B. (2017). Origins of Atlantic decadal swings. *Nature*, *548*(7667), 284-285.
- Viau, A., Gajewski, K., Sawada, M., & Fines, P. (2006). Millennial-scale temperature variations in North America during the Holocene. *Journal of Geophysical Research: Atmospheres*, *111*(D9).
- Walsh, K. J., McBride, J. L., Klotzbach, P. J., Balachandran, S., Camargo, S. J., Holland, G., . . . Sobel, A. (2016). Tropical cyclones and climate change. *Wiley Interdisciplinary Reviews: Climate Change*, *7*(1), 65-89.
- Wang, X. L., Wan, H., & Swail, V. R. (2006). Observed changes in cyclone activity in Canada and their relationships to major circulation regimes. *Journal of climate*, *19*(6), 896-915.
- Wang, X. L., Zwiers, F. W., Swail, V. R., & Feng, Y. (2009). Trends and variability of storminess in the Northeast Atlantic region, 1874–2007. *Climate Dynamics*, *33*(7-8), 1179.
- Warner, B. G., & Asada, T. (2006). Biological diversity of peatlands in Canada. *Aquatic Sciences*, *68*(3), 240-253.
- Wentworth, C. K. (1922). A scale of grade and class terms for clastic sediments. *The journal of geology*, *30*(5), 377-392.
- Williams, H. F. (2013). 600-year sedimentary archive of hurricane strikes in a prograding beach ridge plain, southwestern Louisiana. *Marine Geology*, *336*, 170-183.
- Wu, X., de Vernal, A., Fréchette, B., Moros, M., & Perner, K. (2022). The signal of climate changes over the last two millennia in the Gulf of St. Lawrence, eastern Canada. *Quaternary Research*, *106*, 28-43.
- Yang, Y., Maselli, V., Normandeau, A., Piper, D. J., Li, M. Z., Campbell, D. C., . . . Gao, S. (2020). Latitudinal response of storm activity to abrupt climate change during the last 6,500 years. *Geophysical research letters*, *47*(19), e2020GL089859.

## Supplementary figures

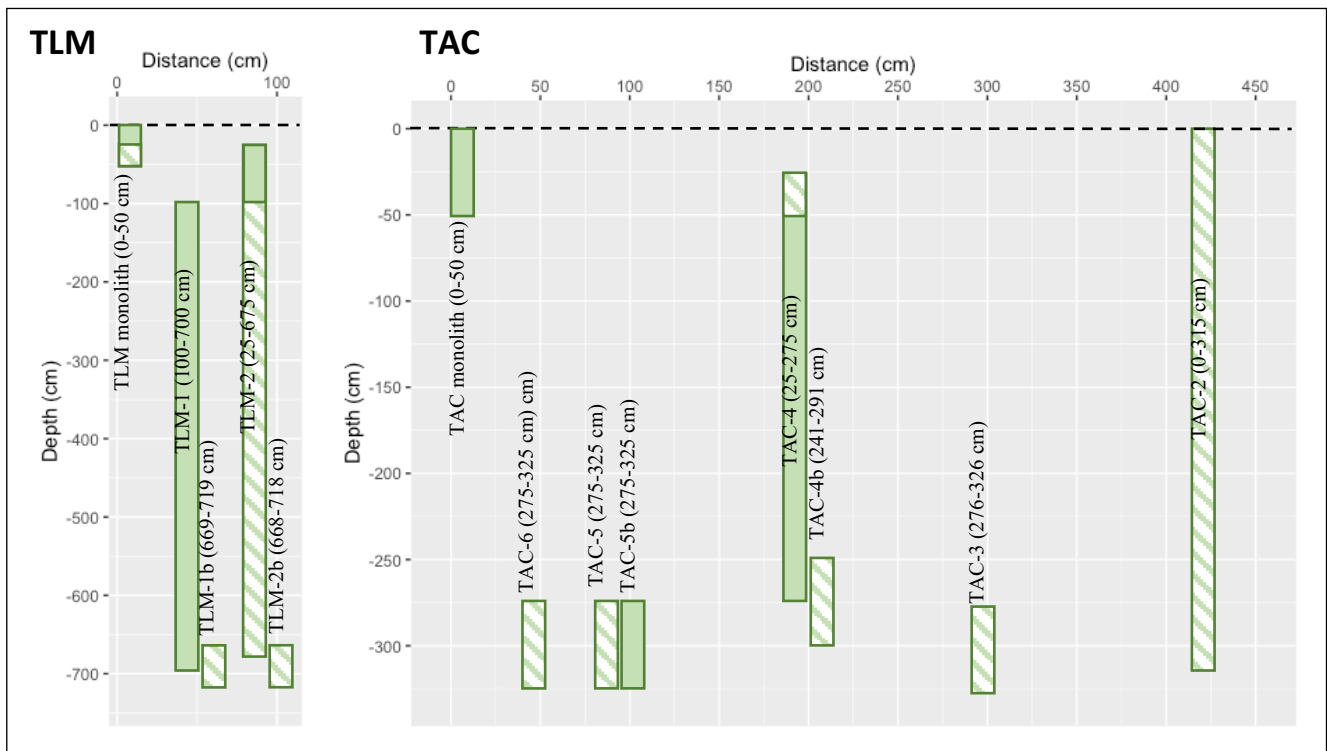


**Figure S1** Diagram of the depths of each segment of the cores (TLM on the left, TAC on the right). The black dashed line on the x-axis represents the surface. Notice the y-axis is different in the two subgraphs. Core drives or core segments that were aggregated to create the composite cores are indicated in solid green. The TLM composite core includes: the segment from the surface to 25 cm from the TLM-monolith; the segment from 25 cm to 100 cm from TLM-2; and the full core drive from TLM-1. The TAC composite core includes: the full TAC-monolith section; the section from 50 cm to 275 cm from TAC-4; and the full TAC-5b core drive. The other cores or core segments (green hatched) were kept for preliminary analysis, other research purposes and for reference, if needed.



**Figure S2 A** Photos of the cores taken at the TAC site after extraction from the peatland. Only cores that are part of the TAC composite core are presented. From right to left: TAC-4 25-75 cm, TAC-4 75-125 cm, TAC-4 125-175 cm, TAC-4 175-225 cm, TAC-4 225-275 cm, TAC-5b 275-325 cm. The top of each core is oriented towards the surface.



**Figure S2 B** Photos of the cores taken at the TLM site after extraction from the peatland. Only cores that are part of the TLM composite core are presented. From right to left: TLM-2 25-75 cm, TLM-2 75-100 cm, TLM-1 100-150 cm, TLM-1 150-200 cm, TLM-1 200-250 cm, TLM-1 250-300 cm, TLM-1 300-350, TLM-1 350-400. The top of each core is oriented towards the surface. (cont'd on next page).

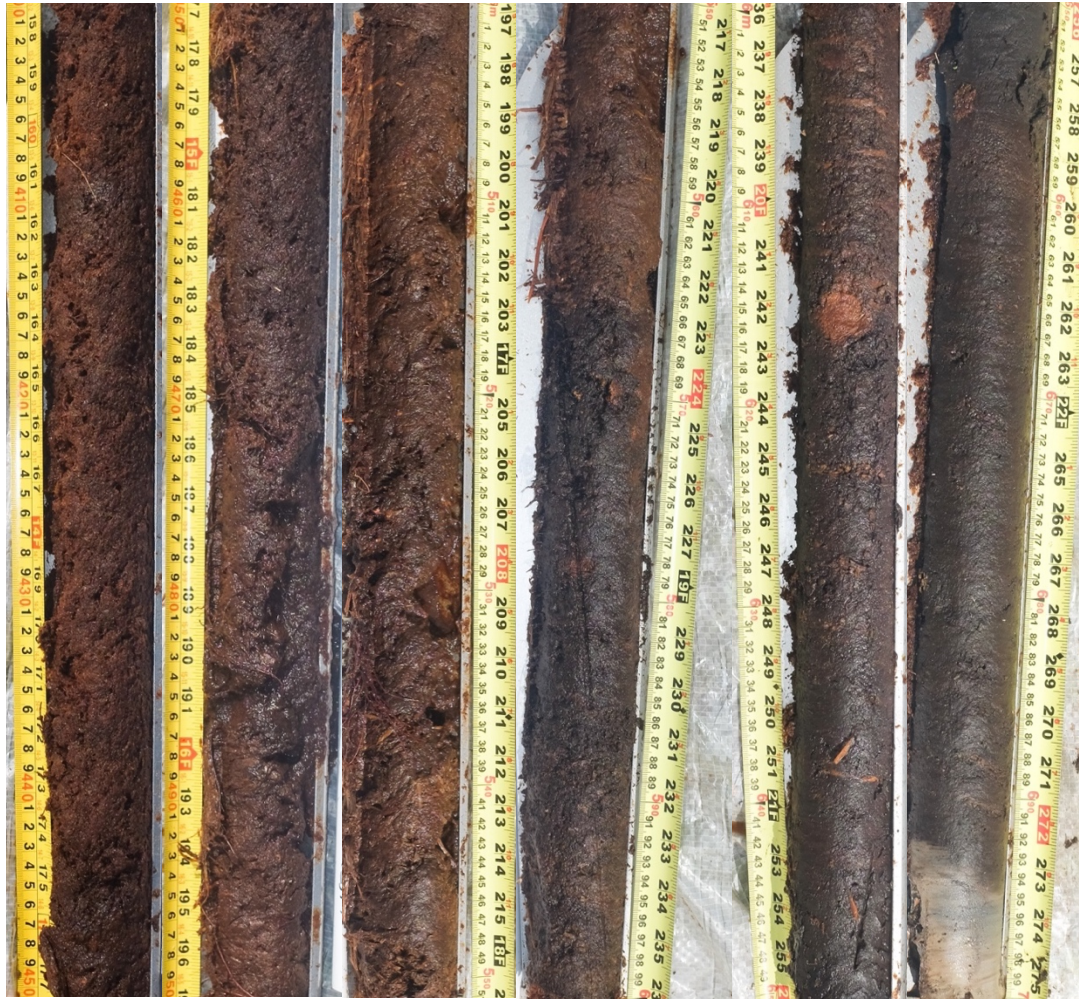
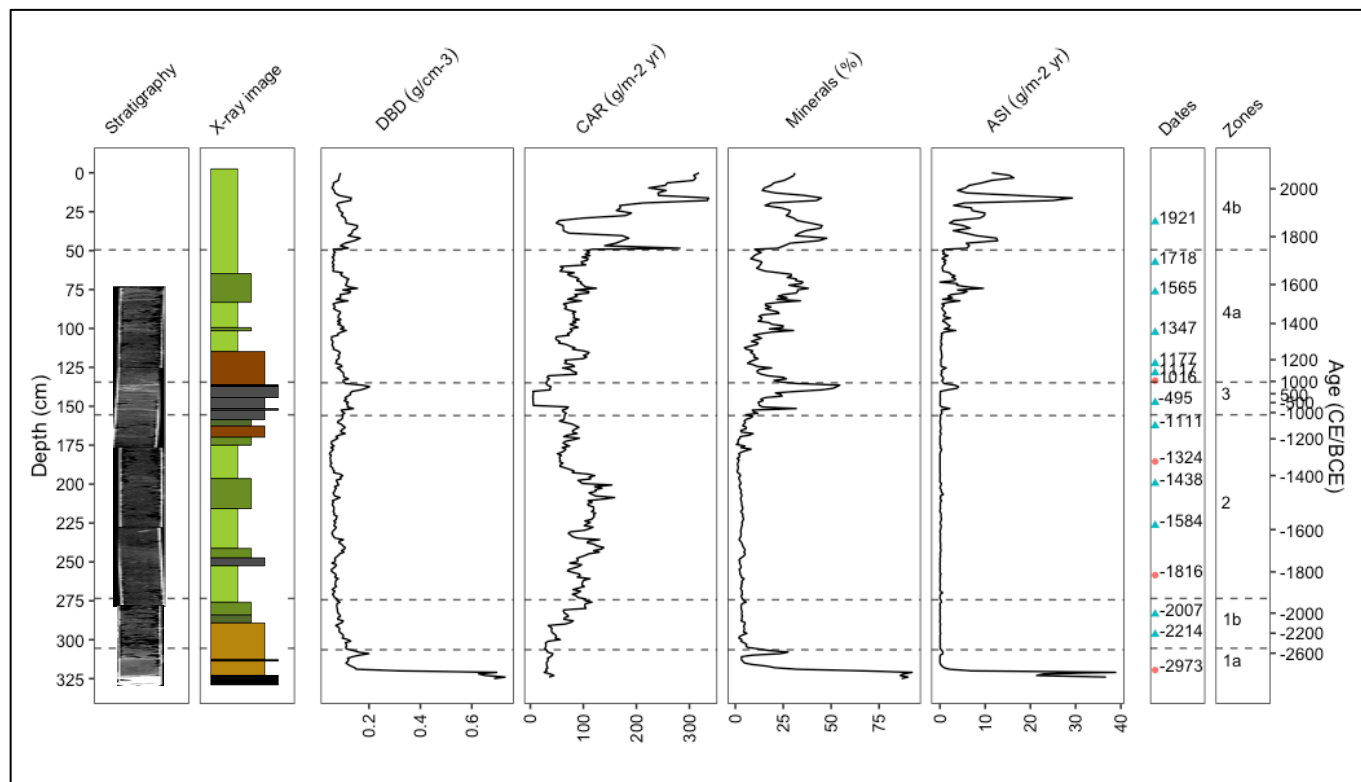


**Figure S2 B (cont'd)** From right to left: TLM-1 400-450 cm, TLM-1 450-500 cm, TLM-1 550-600 cm, TLM-1 600-650 cm, TLM-1 650-700 cm. The top of each core is oriented towards the surface



Bryophytic peat    Bryophytic peat    Bryophytic peat    Herbaceous peat    Ligneous peat    Detritus peat    Minerals   

**Figure S3** Lithology and sedimentology of the TAC core with the basal sand layers. The core is plotted by depth (left-hand side) with the corresponding age from the age-depth model on the right-hand side, in CE/BCE. The x-ray images were taken by computerized-tomography scanning (CT-Scan). Peat stratigraphy is indicated by color. The width of each layer is a qualitative indication of density. Dry bulk density (DBD) is shown as  $\text{g}/\text{cm}^3$ . Carbon accumulation rate is shown as  $\text{g}/\text{m}^2 \cdot \text{year}$ . Mineral content is the percent of minerals, in  $5 \text{ cm}^3$  of dried peat. Aeolian sand influx (ASI) is presented in  $\text{g}/\text{m}^2 \cdot \text{yr}$  per year. Modelled AMS  $^{14}\text{C}$  dates are shown as a blue triangle for a date from wood, and as a red circle for a date from bulk peat. Core units calculated by CONISS algorithm are also shown on the right of each plot.

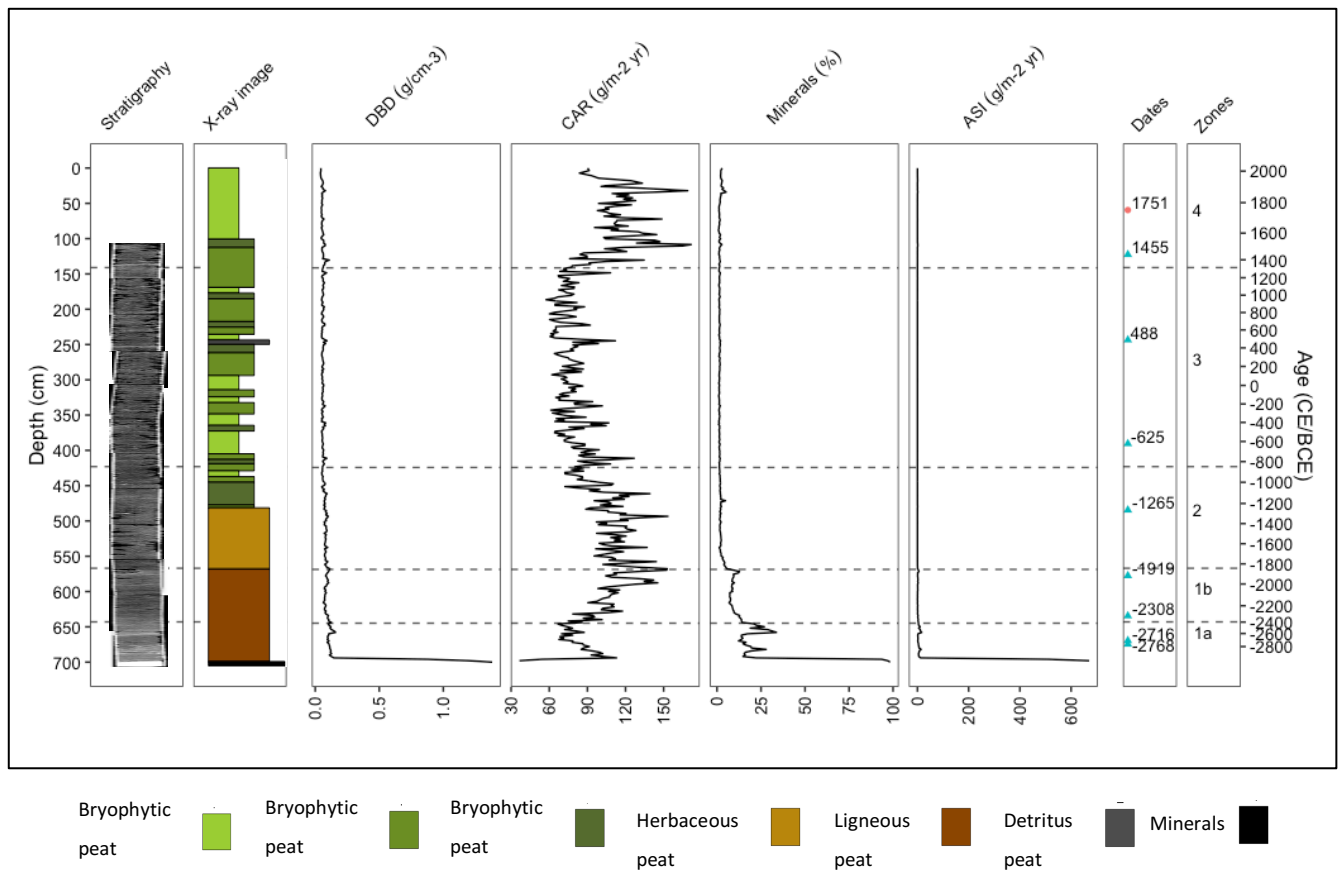


**Figure S4** Lithology and sedimentology of the TLM core with the basal sand layers. The core is plotted by depth (left-hand side) with the corresponding age from the age-depth model on the right-hand side, in CE/BCE. The x-ray images were taken by computerized-tomography scanning (CT-Scan). Peat stratigraphy is indicated by color. The width of each layer is a qualitative indication of density. Dry bulk density (DBD) is shown as  $\text{g}/\text{cm}^3$ . Carbon accumulation rate is shown as  $\text{g}/\text{m}^2 \cdot \text{year}$ . Mineral content is the percent of minerals, in  $5 \text{ cm}^3$  of dried peat. Aeolian sand influx (ASI) is presented in  $\text{g}/\text{m}^2 \cdot \text{yr}$  per year. Modelled AMS  $^{14}\text{C}$  dates are shown as a blue triangle for a date from wood, and as a red circle for a date from bulk peat. Core units calculated by CONISS algorithm are also shown on the right of each plot.

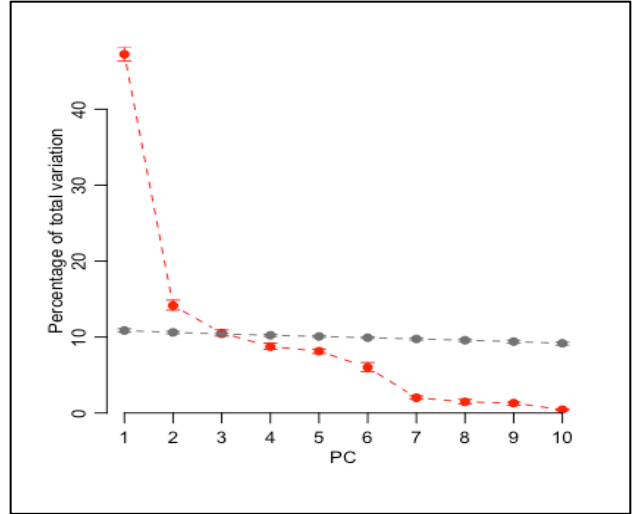
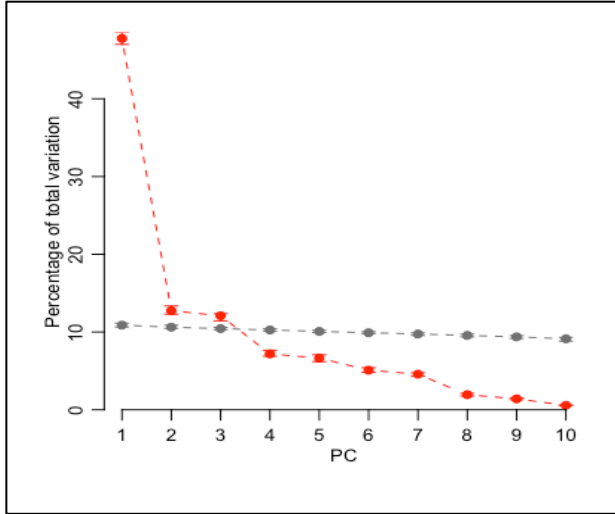


**Figure S5** PCA test performed in R of TAC (left) and TLM (right). PC axes 1, 2 and 3 are significant at  $p$ -value  $< 0.05$  for TAC, and PC axes 1 and 2 are significant at  $p$ -value  $< 0.05$  for TLM.

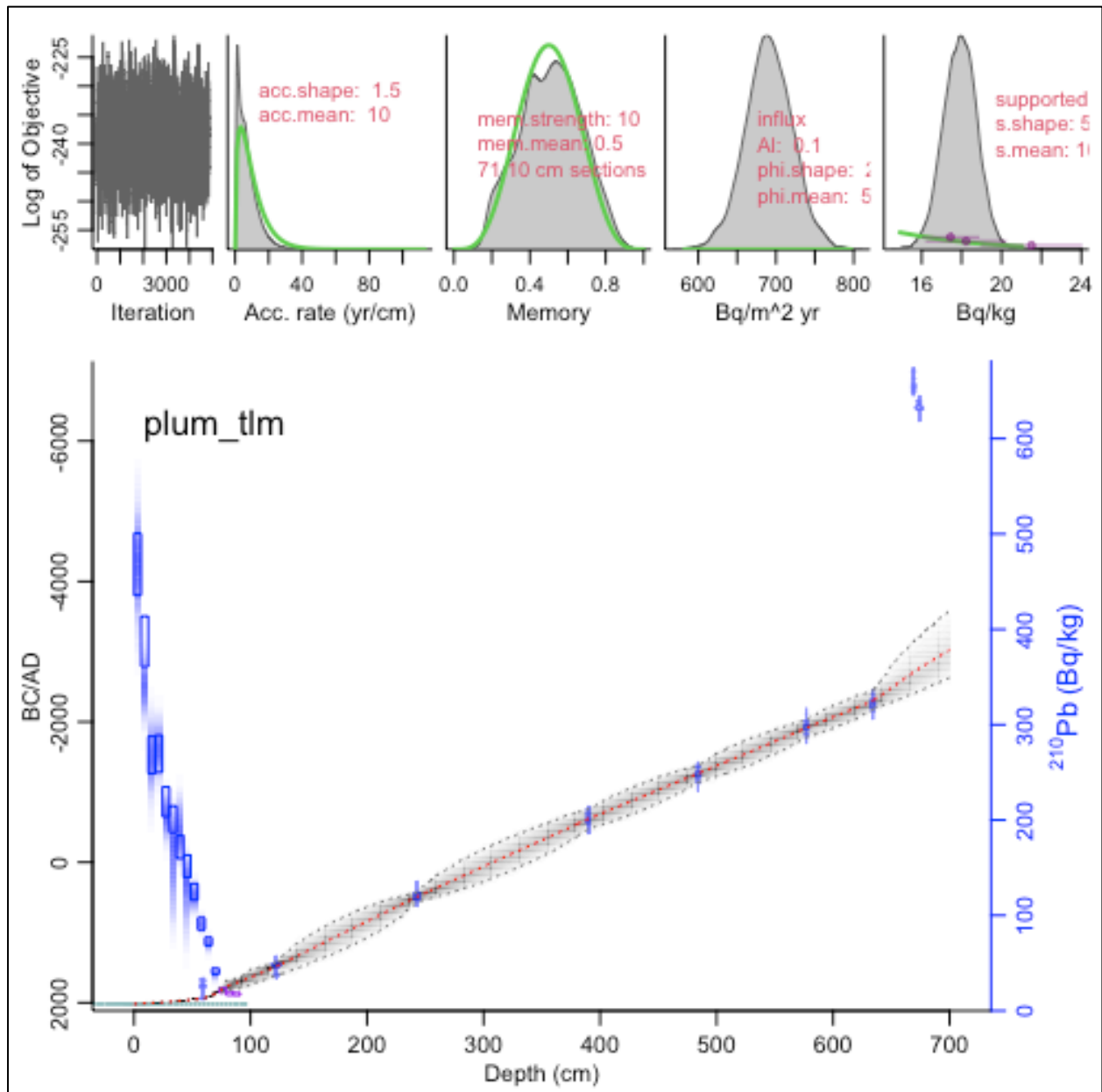


**Figure S6** BACON-derived alternative age-depth models for TLM. Radiocarbon ( $^{14}\text{C}$ ) dates are shown in blue along the age model. The  $^{210}\text{Pb}$  dates from the top 50 cm of the TAC core were plugged into the TLM age-depth model, adjusting for TLM depths, and are shown in purple. The surface date (2019 CE) is indicated in teal. The rate of supported  $^{210}\text{Pb}$  (right axis) is indicated by the blue boxes on the left-hand side (the blue boxes are the measured  $^{210}\text{Pb}$  values; blue shadings represent the modelled  $^{210}\text{Pb}$  values). The leftmost upper panel depicts the Markov Chain Monte Carlo (MCMC) iterations; then the prior (green curve) and posterior (grey histogram) distributions the accumulation rate (second panel), and next the memory (third panel). The fourth panel indicates  $^{210}\text{Pb}$  influx in  $\text{Bq}/\text{m}^2\cdot\text{yr}$  and the fifth panel indicates supported  $^{210}\text{Pb}$  in  $\text{Bq}/\text{kg}$ .

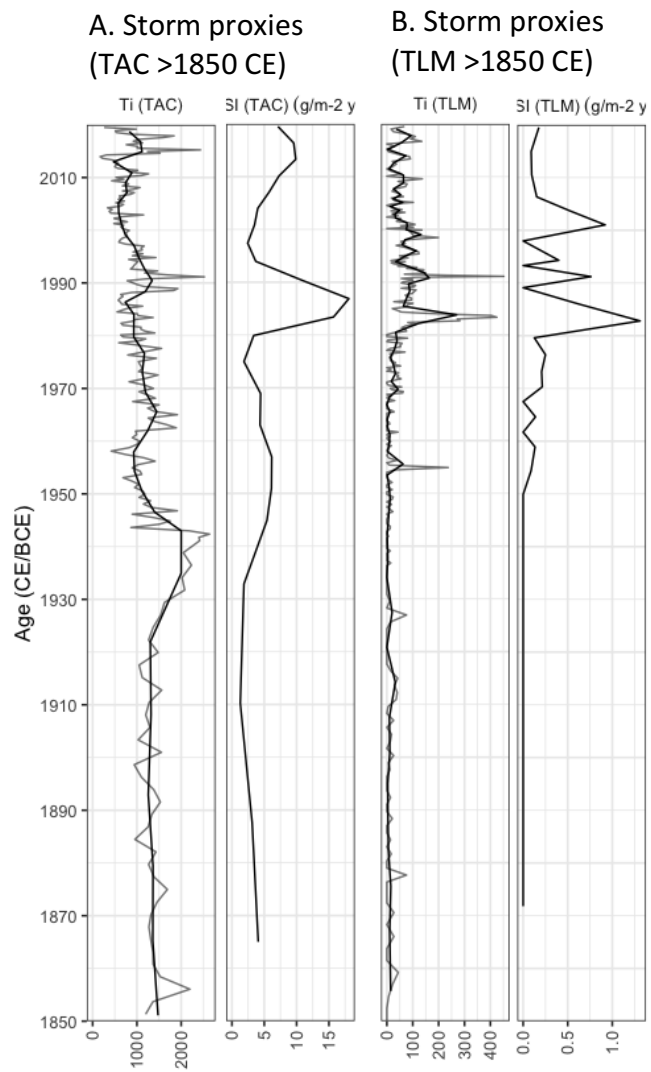


**Figure S7** Comparison of TAC and TLM storm proxies with an alternative age-model for TLM, where  $^{210}\text{Pb}$  values from TAC were plugged into an age-model for TLM (see Supplemental Figure S6). In panel A and B, the ASI and Ti peaks from both cores match together, especially in the period from 2010-1970.

## Supplementary tables

**Table S1** Description of the main characteristics of the 92 studies included in the meta-analysis.

| <b>ID</b> | <b>Reference</b>                     | <b>Location</b>   | <b>Climate archive</b>     | <b>Storm variable</b> | <b>Storm proxy</b>  | <b>Analytical methods</b>                                       | <b>Record duration (years)</b> |
|-----------|--------------------------------------|---|----------------------------|-----------------------|---|---|--------------------------------|
| 1         | <b>Adomat &amp; Gischler 2017</b>    | Manatee Lagoon, Belize                                    | Lagoon core                | Storm surge           | Washover fan/sheetwash  | Grain-size<br>Micropaleontology                                 | 8000                           |
| 2         | <b>Baldini et al. 2016</b>           | Yok Balum Cave, Belize                                    | Speleothems                | Storm precipitation   | $\delta^{18}\text{O}$ and $\delta^{13}\text{C}$ in calcite structures | Stable isotope geochemistry                                     | 430                            |
| 3         | <b>Besonen et al. 2008</b>           | Lower Mystic Lake, Massachusetts, USA                     | Estuary core               | Storm precipitation   | Coarse sediment layers/turbidities                                    | Grain-size<br>Micropaleontology                                 | 1000                           |
| 4         | <b>Bjorckl et al. 2004</b>           | Halland, Sweden   | Ombrotrophic peatland core | Storm winds           | Aeolian sand  | Aeolian sand influx<br>Loss-on-ignition                         | 7000                           |
| 5         | <b>Boldt et al. 2010</b>             | Mattapoisett, Massachusetts, USA                          | Salt marsh core            | Storm surge           | Washover fan  | Loss-on-ignition<br>Grain-size                                  | 2000                           |
| 6         | <b>Brandon et al. 2013</b>           | Spring Creek and Mullet Pond, Apalachee Bay, Florida, USA | Sinkhole core              | Storm winds           | Aeolian sand  | Loss-on-ignition<br>Grain-size                                  | 2500                           |
| 7         | <b>Brandon et al. 2014</b>           | New York, NY, USA   | Pond core                  | Storm surge           | Sheetwash   | Loss-on-ignition<br>Grain-size                                  | 615                            |
| 8         | <b>Braun et al. 2017</b>             | St. Catherines Island, Georgia, USA                       | Salt marsh core            | Storm surge           | Washover fan  | Loss-on-ignition<br>Elemental geochemistry<br>Micropaleontology | 3000                           |
| 9         | <b>Bregy et al. 2018</b>             | Hancock County, Mississippi, USA                          | Pond core                  | Storm surge           | Washover fan  | Loss-on-ignition<br>Grain-size<br>Micropaleontology             | 2500                           |
| 10        | <b>Brown et al. 2014</b>             | Laguna Chumkopó, Mexico                                   | Sinkhole core              | Bottom shear stress   | Coarse sediment layers/turbidities                                    | Loss-on-ignition<br>Grain-size                                  | 7000                           |
| 11        | <b>Buynevich &amp; Donnelly 2006</b> | Cape Cod Bay, Massachusetts, USA                          | Lagoon core                | Storm surge           | Washover fan  | Grain-size  | 1500                           |
| 12        | <b>Buynevich 2007</b>                | Gulf of Maine, Maine, USA                                 | Beach scarps               | Storm surge           | Beach scarps  | Grain-size  | 1100                           |
| 13        | <b>Castagno et al. 2021</b>          | Mattapoisett, Massachusetts, USA                          | Salt marsh core            | Storm surge           | Washover fan  | Grain-size  | 650                            |
| 14        | <b>Clemmensen et al. 2008</b>        | Eastern Jutland, Denmark                                  | Dunefield                  | Storm winds           | Aeolian sand  | Grain-size  | 5000                           |
| 15        | <b>Collins-Key &amp; Altman 2021</b> | Lake Louise, South Central Georgia, USA                   | Tree ring                  | Storm winds           | Storm winds   | Tree-ring width   | 105                            |

|    |                                      |   |                            |                     |  |   |       |
|----|--------------------------------------|---|----------------------------|---------------------|--|---|-------|
| 16 | <b>Das et al. 2013</b>               | Eastern Lake and Western Lake, Florida, USA         | Lake core                  | Storm surge         | Washover fan<br>$\delta^{15}\text{N}$ and $\delta^{13}\text{C}$ in sediments | Grain-size<br>Stable isotope geochemistry                 | 4000  |
| 17 | <b>Dawson et al. 2004</b>            | Outer Hebrides, Scotland                            | Dunefield                  | Storm winds         | Aeolian sand   | Micropaleontology<br>Grain-size                           | 1150  |
| 18 | <b>de Jong 2006</b>                  | Undarsmossen bog, Halland, Sweden                   | Ombrotrophic peatland core | Storm winds         | Aeolian sand   | Loss-on-ignition<br>Grain-size                            | 6500  |
| 19 | <b>Degeai et al. 2015</b>            | Bagna Pond, Languedoc, France                       | Lagoon core                | Storm surge         | Washover fan   | Element geochemistry<br>Grain-size                        | 3000  |
| 20 | <b>Denomme et al. 2014</b>           | Lighthouse Reef, Belize                             | Blue hole core             | Bottom shear stress | Coarse sediment layers/turbidities   | Grain-size  | 1200  |
| 21 | <b>Dezileau &amp; Castaigns 2011</b> | Pierre Blanche Lagoon, Languedoc-Roussillon, France | Lagoon core                | Storm surge         | Washover fan   | Grain-size<br>Element geochemistry                        | 1500  |
| 22 | <b>Donnelly 2001</b>                 | Whale Beach, New Jersey, USA                        | Salt marsh core            | Storm surge         | Washover fan   | Grain-size  | 700   |
| 23 | <b>Donnelly 2001</b>                 | Succotash Marsh, Matunuck, Rhode Island, USA        | Salt marsh core            | Storm surge         | Washover fan   | Grain-size  | 700   |
| 24 | <b>Donnelly et al. 2007</b>          | Laguna Playa Grande, Vieques, Puerto Rico           | Lagoon core                | Storm surge         | Washover fan   | Grain-size  | 5000  |
| 25 | <b>Donnelly et al. 2015</b>          | Salt Pond, Massachusetts, USA                       | Brackish pond core         | Storm surge         | Washover fan   | Loss-on-ignition<br>Element geochemistry                  | 2000  |
| 26 | <b>Ercolani et al. 2015</b>          | Keewaydin Island, Florida, USA                      | Lagoon core                | Storm surge         | Washover fan   | Grain-size<br>Micropaleontology                           | 1000  |
| 27 | <b>Frappier et al. 2007</b>          | Actun Tunichil Muknal Cave, Belize                  | Speleothems growth ring    | Storm precipitation | $\delta^{18}\text{O}$ and $\delta^{13}\text{C}$ in calcite structures        | Stable isotope geochemistry                               | 23    |
| 28 | <b>Frappier et al. 2014</b>          | Cenote Chaltun Ha, Yucatan, Mexico                  | Speleothems growth ring    | Storm precipitation | Coarse sediment layers/turbidities   | Presence of mud layer in stalagmite                       | 2240  |
| 29 | <b>Gischler et al. 2008</b>          | Blue Hole, Lighthouse Reef, Belize                  | Blue hole core             | Bottom shear stress | Coarse sediment layers/turbidities   | Grain-size  | 1500  |
| 30 | <b>Goslin et al. 2018</b>            | Filsø, Denmark                                      | Wetland core               | Storm winds         | Aeolian sand   | Aeolian sand influx<br>Elemental geochemistry             | 10000 |
| 31 | <b>Goslin et al. 2019</b>            | Filsø, Denmark                                      | Wetland core               | Storm winds         | Aeolian sand   | Grain-size<br>Aeolian sand influx<br>Element geochemistry | 4900  |
| 32 | <b>Gregory et al. 2015</b>           | Playa Bailen/Punta de Cartas, Cuba                  | Lagoon core                | Storm precipitation | Coarse sediment layers/turbidities   | Micropaleontology<br>Elemental geochemistry               | 4000  |
| 33 | <b>Heller et al. 2021</b>            | Grape Tree Pond, Jamaica                            | Freshwater lagoon core     | Storm precipitation | Water level  | Element geochemistry<br>Micropaleontology                 | 1500  |

|  |  |                             |                     |   |  |      |
|--|--|-----------------------------|---------------------|---|--|------|
| <b>34 Hippensteel et al. 2013</b>      | Onslow Bay, North Carolina, USA                | Salt marsh core             | Storm surge         | Washover fan/sheetwash                                      | Micropaleontology  | 1500 |
| <b>35 Jahan et al. 2021</b>            | Western Lake and Mullet Pond, Florida, USA     | Lake core                   | Storm surge         | Sheetwash   | Stable isotope geochemistry                              | 180  |
| <b>36 Kalinska-Nartisa et al. 2018</b> | Lake Lilaste, Latvia                           | Lake core                   | Storm winds         | Aeolian sand  | Grain-size   | 8500 |
| <b>37 Kiage 2020</b>                   | Bay Jimmy, Louisiana, USA                      | Salt marsh core             | Storm surge         | Washover fan  | Loss-on-ignition<br>Grain-size                           | 1200 |
| <b>38 Kiage et al. 2011</b>            | Wassaw Island, Georgia, USA                    | Salt marsh core             | Storm surge         | Washover fan  | Loss-on-ignition   | 1900 |
| <b>39 Kylander et al. 2020</b>         | Laphroaig Bog, Islay, Scotland                 | Ombrotrophic peatland core  | Storm winds         | Aeolian sand  | Grain-size<br>Elemental geochemistry                     | 6670 |
| <b>40 Lane et al. 2011</b>             | Apalachee Bay, Florida, USA                    | Sinkhole core               | Storm surge         | Washover fan/sheetwash                                      | Loss-on-ignition<br>Grain-size<br>Micropaleontology      | 4500 |
| <b>41 Lane et al. 2017</b>             | Laguna Alejandro, Barahona, Dominican Republic | Lagoon core                 | Storm precipitation | $\delta^{18}\text{O}$ in calcite structures                 | Stable isotope geochemistry<br>Grain-size                | 950  |
| <b>42 LeBlanc et al. 2017</b>          | Laguna Alejandro, Barahona, Dominican Republic | Lagoon core                 | Storm surge         | $\delta^{18}\text{O}$ in calcite structures<br>Washover fan | Loss-on-ignition<br>Stable isotope geochemistry          | 1000 |
| <b>43 Liu &amp; Fearn 2000</b>         | Western Lake, Florida, USA                     | Lake core                   | Storm surge         | Washover fan  | Loss-on-ignition   | 7000 |
| <b>44 Liu et al. 2008</b>              | Little Lake, Mississippi, USA                  | Lake core                   | Storm surge         | Washover fan  | Micropaleontology<br>Grain-size                          | 1200 |
| <b>45 Liu et al. 2014</b>              | Lake Pontchartrain, Mississippi, USA           | Salt marsh core             | Storm surge         | Sheetwash   | Loss-on-ignition<br>Grain-size<br>Elemental geochemistry | 1200 |
| <b>46 Maanan et al. 2022</b>           | Belle Henriette Lagoon, France                 | Lagoon core                 | Storm surge         | Washover fan  | Grain-size<br>Elemental geochemistry                     | 1400 |
| <b>47 Maio et al. 2016</b>             | Waqoit Bay, Massachusetts, USA                 | Lagoon core                 | Storm surge         | Washover fan  | Grain-size   | 3500 |
| <b>48 McCloskey &amp; Liu 2012</b>     | Bluefields Bay, Nicaragua                      | Lagoon core                 | Storm surge         | Washover fan  | Loss-on-ignition<br>Micropaleontology                    | 5400 |
| <b>49 McCloskey &amp; Liu 2013</b>     | Belize   | Lagoon and salt marsh cores | Storm surge         | Washover fan  | Grain-size   | 7000 |
| <b>50 Medina-Elizalde et al. 2016</b>  | Yucatan Peninsula, Mexico                      | Speleothems growth ring     | Storm precipitation | $\delta^{18}\text{O}$ in calcite structures                 | Stable isotope geochemistry                              | 1250 |
| <b>51 Mora 2007</b>                    | Valdosta, Georgia, USA                         | Longleaf pine tree ring     | Storm precipitation | $\delta^{18}\text{O}$ in cellulose                          | Stable isotope geochemistry                              | 50   |

|                                   |  |                              |                     |                                    |   |       |
|-----------------------------------|--|------------------------------|---------------------|------------------------------------|---|-------|
| <b>52 Moskalewicz et al. 2020</b> | Gulf of Gdańsk, Poland                         | Beach ridge<br>Peatland core | Storm surge         | Washover fan/sheetwash             | Loss-on-ignition<br>Grain-size  | 1300  |
| <b>53 Naquin et al. 2014</b>      | Bay Champagne, Mississippi, USA                | Lagoon core                  | Storm surge         | Washover fan/sheetwash             | Loss-on-ignition<br>Elemental geochemistry  | 2900  |
| <b>54 Nielsen et al. 2016</b>     | Andøya, Norway                                 | Lake core                    | Storm winds         | Aeolian sand                       | Loss-on-ignition<br>Elemental geochemistry  | 6200  |
| <b>55 Nielsen et al. 2016</b>     | Trehynnavatnet, Norway                         | Lake core                    | Storm winds         | Aeolian sand                       | Grain-size<br>Elemental geochemistry  | 2850  |
| <b>56 Nikitina et al. 2014</b>    | Sea Breeze, New Jersey, USA                    | Salt marsh core              | Storm surge         | Washover fan                       | Loss-on-ignition<br>Grain-size  | 2000  |
| <b>57 Oliva et al. 2018</b>       | Robinson Lake, Nova Scotia, Canada             | Lake core                    | Storm surge         | Washover fan/sheetwash             | Grain-size<br>Loss-on-ignition<br>Elemental geochemistry                                | 800   |
| <b>58 Orme et al. 2015</b>        | Cors Fochno, Wales                             | Ombrotrophic peatland core   | Storm winds         | Aeolian sand<br>Marine aerosols    | Loss-on-ignition<br>Grain-size<br>Elemental geochemistry                                | 4500  |
| <b>59 Orme et al. 2016</b>        | Hill Top/Struban Bog, Outer Hebrides, Scotland | Ombrotrophic peatland core   | Storm winds         | Aeolian sand                       | Elemental geochemistry  | 1800  |
| <b>60 Orme et al. 2016b</b>       | Loch Hosta, Outer Hebrides, UK                 | Lake core                    | Storm winds         | Aeolian sand                       | Elemental geochemistry<br>Stable isotope geochemistry<br>Loss-on-ignition<br>Grain-size | 1800  |
| <b>61 Orme et al. 2017</b>        | Pedrino Bog, Spain                             | Ombrotrophic peatland core   | Storm winds         | Aeolian sand                       | Loss-on-ignition  | 4000  |
| <b>62 Parris et al. 2010</b>      | Multiple lakes across Vermont, USA             | Lake core                    | Storm precipitation | Coarse sediment layers/turbidities | Grain-size  | 14000 |
| <b>63 Peros et al. 2015</b>       | Guamá, Santiago de Cuba, Cuba                  | Lagoon core                  | Storm surge         | Washover fan                       | Loss-on-ignition<br>Grain-size<br>Micropaleontology                                     | 4000  |
| <b>64 Pouzet et al. 2018</b>      | Island of Yeu, France                          | Salt marsh core              | Storm surge         | Washover fan                       | Grain-size<br>Loss-on-ignition<br>Elemental geochemistry                                | 7500  |
| <b>65 Ranasinghe et al. 2021</b>  | Choctawhatchee Bay, Florida, USA               | Lagoon core                  | Storm surge         | Washover fan/sheetwash             | Elemental geochemistry<br>Loss-on-ignition<br>Stable isotope geochemistry<br>Grain-size | 8000  |
| <b>66 Rodriguez et al. 2018</b>   | Onslow Beach, North Carolina, USA              | Beach ridge                  | Storm surge         | Beach ridge                        | Grain-size  | 2000  |

|    |                                     |   |                      |                     |   |   |      |
|----|-------------------------------------|---|----------------------|---------------------|---|---|------|
| 67 | <b>Rodysill et al. 2020</b>         | Basin Bayou/Shotgun Pond, Florida, USA                          | Pond core            | Storm surge         | Washover fan/sheetwash  | Grain-size  | 2000 |
| 68 | <b>Sabatier &amp; Dezileau 2010</b> | Gulf of Lion, France  | Lagoon core          | Storm surge         | Washover fan/sheetwash  | Grain-size<br>Micropaleontology                           | 7800 |
| 69 | <b>Sabatier et al. 2008</b>         | Pierre Blanche Lagoon, Languedoc-Roussillon, France             | Lagoon core          | Storm surge         | Washover fan/sheetwash  | Grain-size  | 250  |
| 70 | <b>Sabatier et al. 2010</b>         | Pierre Blanche Lagoon, Languedoc-Roussillon, France             | Lagoon core          | Storm surge         | Washover fan/sheetwash  | Loss-on-ignition<br>Grain-size<br>Elemental geochemistry  | 250  |
| 71 | <b>Sabatier et al. 2012</b>         | Gulf of Lion, France  | Lagoon core          | Storm surge         | Washover fan/sheetwash  | Grain-size<br>Elemental geochemistry<br>Micropaleontology | 7000 |
| 72 | <b>Scileppi et al. 2007</b>         | Long Island, NY, USA  | Salt marsh core      | Storm surge         | Washover fan  | Grain-size  | 700  |
| 73 | <b>Sjögren 2009</b>                 | Sørøya, Norway  | Dunefield            | Storm winds         | Aeolian sand  | Loss-on-ignition  | 800  |
| 74 | <b>Stewart et al. 2017</b>          | Shebster, Scotland  | Peatland core        | Storm winds         | Aeolian sand<br>Marine aerosols   | Loss-on-ignition<br>Elemental geochemistry                | 8000 |
| 75 | <b>Tisdall et al. 2013</b>          | Stronsay, Scotland, UK  | Dunefield            | Storm winds         | Aeolian sand  | Grain-size (ASI)<br>Loss-on-ignition                      | 8000 |
| 76 | <b>Toomey et al. 2013</b>           | Great Bahama Bank, Bahamas                                      | Offshore basin core  | Bottom shear stress | Coarse sediment layers/turbidities  | Grain-size  | 7000 |
| 77 | <b>Tucker et al. 2018</b>           | Grand Bay National Estuarine Research Reserve, Mississippi, USA | Slash Pine tree ring | Storm surge         | Storm surge   | Tree-ring width   | 110  |
| 78 | <b>Urquhart 2009</b>                | Laguna Negra, Nicaragua   | Lagoon core          | Storm surge         | Washover fan/sheetwash  | Loss-on-ignition  | 8000 |
| 79 | <b>van Hengstum et al. 2014</b>     | Thatchpoint Bluehole, Little Bahama Bank, Bahamas               | Blue hole core       | Bottom shear stress | Coarse sediment layers/turbidities  | Loss-on-ignition<br>Grain-size                            | 900  |
| 80 | <b>van Hengstum et al. 2015</b>     | Walsingham Cavern, Bermuda                                      | Underwater cave      | Storm precipitation | $\delta^{18}\text{O}$ in calcite structures<br>Coarse sediment layers/turbidities | Grain-size<br>Stable isotope geochemistry                 | 3100 |
| 81 | <b>van Hengstum et al. 2016</b>     | Blackwood sinkhole, North Abaco, Bahamas                        | Sinkhole core        | Storm surge         | Washover fan  | Grain-size  | 3000 |
| 82 | <b>Van Vliet-Lanë et al. 2014</b>   | Bay of Audierne, France   | Dunefield            | Storm surge         | Washover fan/sheetwash  | Grain-size  | 6000 |
| 83 | <b>Vandel et al. 2019</b>           | Estonian coast  | Peatland core        | Storm winds         | Aeolian sand  | Aeolian sand influx<br>Elemental geochemistry             | 600  |

|                                |   |                     |                     |                                    |                                      |      |
|--------------------------------|---|---------------------|---------------------|------------------------------------|--------------------------------------|------|
| <b>84 Wallace et al. 2019</b>  | South Andros Islands, Bahamas                     | Blue hole core      | Bottom shear stress | Coarse sediment layers/turbidities | Grain-size                           | 1500 |
| <b>85 Wallace et al. 2021</b>  | Long Island, Bahamas                              | Blue hole core      | Bottom shear stress | Coarse sediment layers/turbidities | Grain-size                           | 1050 |
| <b>86 Wallace et al. 2021</b>  | Middle Caicos, Turks and Caicos Islands           | Blue hole core      | Bottom shear stress | Coarse sediment layers/turbidities | Grain-size                           | 1500 |
| <b>87 Williams 2013</b>        | Blue Buck Ridge, Louisiana, USA                   | Beach ridges        | Storm surge         | Beach ridge                        | Loss-on-ignition<br>Grain-size       | 600  |
| <b>88 Winkler et al. 2020</b>  | Thatchpoint Bluehole, Little Bahama Bank, Bahamas | Blue hole core      | Bottom shear stress | Coarse sediment layers/turbidities | Grain-size                           | 700  |
| <b>89 Winkler et al. 2022</b>  | Cay Sal Bank, The Bahamas                         | Blue hole core      | Bottom shear stress | Coarse sediment layers/turbidities | Grain-size                           | 530  |
| <b>90 Woodruff et al. 2008</b> | Laguna Playa Grande, Puerto Rico                  | Lagoon core         | Storm surge         | Sheetwash                          | Grain-size                           | 5000 |
| <b>91 Yang et al. 2020</b>     | Emerald Basin, Nova Scotia, Canada                | Offshore basin core | Bottom shear stress | Coarse sediment layers/turbidities | Grain-size<br>Elemental geochemistry | 6500 |
| <b>92 Yao et al. 2020</b>      | Shark River Estuary, Florida, USA                 | Salt marsh core     | Storm surge         | Washover fan/sheetwash             | Elemental geochemistry               | 3500 |

**Table S2** List of cores drives from the TLM and TAC. Cores with a *b* suffix were taken in the same hole as their corresponding core and therefore have overlapping material (for example, TLM-1b corresponds to depth 669-719 cm and was taken from the same hole as TLM-1, which corresponds to depth 100-700 cm. Therefore, there is overlapping material between the two core sections). Cores with an asterisk (\*) were used to create the composite cores.

| Core name                  | Depth (cm) |
|----------------------------|------------|
| <i>TLM</i>                 |            |
| TLM-monolith* <sup>1</sup> | 0-50       |
| TLM-1*                     | 100-700    |
| TLM-1b                     | 669-719    |
| TLM-2* <sup>2</sup>        | 25-675     |
| TLM-2b                     | 668-718    |
| <i>TAC</i>                 |            |
| TAC-monolith*              | 0-50       |
| TAC-2                      | 0-315      |
| TAC-3                      | 276-326    |
| TAC-4* <sup>3</sup>        | 25-275     |
| TAC-4b                     | 241-291    |
| TAC-5                      | 275-325    |
| TAC-5b*                    | 275-325    |
| TAC-6                      | 275-325    |

**Notes:**

<sup>1</sup> Only the portion from 0-25 cm was used in the TLM composite core.

<sup>2</sup> Only the portion from 25-100 cm was used in the TLM composite core.

<sup>3</sup> Only the portion from 50-275 cm was used in the TAC composite core.

**Table S3** Results of DCA analysis with Decorana algorithm in R, on XRF data at the mm-scale for TAC and TLM. The first DCA axis length is less than 3 standard deviations for both TLM and TAC, therefore a linear analysis is possible (PCA).

|                 | DCA1 (TAC) | DCA1 (TLM) |
|-----------------|------------|------------|
| Eigenvalues     | 0.03225    | 0.03519    |
| Decorana values | 0.03761    | 0.03868    |
| Axis lengths    | 1.02199    | 0.96006    |

**Table S4** List of hurricanes that passed by 100 km or closer from the Magdalen Islands, with recorded wind of the hurricane at that time and known impacts.

| #  | Date       | Hurricane | Wind speed (km/h) | Known impacts |
|----|------------|-----------|-------------------|---------------|
| 1  | 2019-09-07 | Dorian    | 138               | Yes           |
| 2  | 2014-07-06 | Arthur    | 83                | No            |
| 3  | 2010-09-04 | Earl      | 101               | No            |
| 4  | 2001-10-15 | Karen     | 74                | No            |
| 5  | 1999-09-18 | Floyd     | 65                | No            |
| 6  | 1996-10-10 | Josephine | 83                | No            |
| 7  | 1996-07-14 | Bertha    | 93                | No            |
| 8  | 1991-08-20 | Bob       | 74                | No            |
| 9  | 1988-08-08 | Alberto   | 65                | No            |
| 10 | 1979-09-07 | David     | 93                | No            |
| 11 | 1975-07-28 | Blanche   | 111               | Yes           |
| 12 | 1962-07-04 | Not named | 65                | No            |
| 13 | 1959-07-12 | Cindy     | 65                | No            |
| 14 | 1950-08-21 | Able      | 74                | No            |
| 15 | 1944-09-15 | Not named | 83                | No            |
| 16 | 1940-09-17 | Not named | 111               | No            |
| 17 | 1937-09-26 | Not named | 111               | No            |
| 18 | 1936-09-25 | Not named | 102               | No            |
| 19 | 1934-09-10 | Not named | 46                | No            |
| 20 | 1934-06-21 | Not named | 74                | No            |
| 21 | 1933-10-30 | Not named | 93                | No            |
| 22 | 1933-09-18 | Not named | 111               | No            |
| 23 | 1927-08-25 | Not named | 157               | Yes           |
| 24 | 1924-08-27 | Not named | 111               | No            |
| 25 | 1918-09-07 | Not named | 74                | No            |
| 26 | 1917-08-11 | Not named | 83                | No            |
| 27 | 1916-07-22 | Not named | 56                | No            |
| 28 | 1901-10-01 | Not named | 56                | No            |
| 29 | 1900-09-13 | Not named | 120               | Yes           |
| 30 | 1899-11-02 | Not named | 74                | No            |
| 31 | 1898-10-06 | Not named | 46                | No            |
| 32 | 1896-10-15 | Not named | 65                | No            |

|    |            |           |     |     |
|----|------------|-----------|-----|-----|
| 33 | 1891-10-15 | Not named | 65  | No  |
| 34 | 1889-10-08 | Not named | 74  | No  |
| 35 | 1888-08-23 | Not named | 93  | No  |
| 36 | 1879-11-21 | Not named | 120 | Yes |
| 37 | 1879-08-20 | Not named | 111 | No  |
| 38 | 1877-11-30 | Not named | 74  | No  |
| 39 | 1875-10-16 | Not named | 74  | No  |
| 40 | 1871-10-13 | Not named | 111 | No  |
| 41 | 1860-08-27 | Not named | 65  | No  |
| 42 | 1851-10-14 | Not named | 56  | No  |

**Table S5** Days when winds exceeded 110 km/h on the Magdalen Islands and known impacts. Data from the Historical Weather dataset (Environment and Climate Change Canada, 2020).

| #  | Date          | Wind speed (km/h) | Known impacts          |
|----|---------------|-------------------|------------------------|
| 1  | 2019-09-08/07 | 117               | Yes (Hurricane Dorian) |
| 2  | 2008-12-22    | 117               | Yes                    |
| 3  | 2007-11-04    | 111               | No                     |
| 4  | 2002-11-18    | 111               | No                     |
| 5  | 2001-11-07    | 115               | Yes                    |
| 6  | 1994-11-07    | 132               | Yes                    |
| 7  | 1990-11-26    | 117               | No                     |
| 8  | 1990-11-11    | 113               | No                     |
| 9  | 1989-12-09    | 111               | No                     |
| 10 | 1989-12-03    | 122               | Yes                    |
| 11 | 1986-12-08    | 111               | No                     |
| 12 | 1985-12-18    | 130               | No                     |
| 13 | 1984-11-02    | 115               | No                     |